Photon Detectors for the Ring Imaging Cherenkov Counters of the LHCb Experiment

Richard W. R. Plackett

Imperial College, London

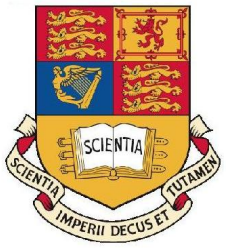

A thesis submitted for the degree of Doctor of Philosophy
in the University of London

July 2006

ABSTRACT

This thesis reports on the author's contribution to the development of the Ring Imaging Cherenkov(RICH) detectors in the LHCb experiment due to take data at the CERN Large Hadron Collider in 2007. The first chapter summarises the physics to be explored by the LHCb experiment; measurements of CP violating asymmetries and a study of rare B decay modes. A brief overview of other experiments studying B-physics is presented. The experiment itself is then described, focussing on the RICH system used for particle identification, with particular emphasis on the photon detectors.

The thesis then reports on the work done by the author on the design of the RICH1 Magnetic Shield, that allows the photon detectors to operate in the fringe field of the LHCb dipole magnet, while fulfilling the conflicting requirement to provide additional magnetic bending power to aid the LHCb charged particle trigger. The design of all of the many sections of the shield are described in depth and the results of finite element simulations performed by the author are reported. The results of measurements the author took of the field produced by the completed magnetic shield are then evaluated and compared with the simulation.

Next follows a study undertaken by the author on the electronic readout of the RICH Hybrid Photon Detectors (HPD). Two related mesurments were made, a novel series of timing tests on the HPD's analogue readout in an assembled tube and a series of experiments using a pulsed laser to simulate the charge deposition of a photoelectron. The final part of the thesis describes the analysis of data taken in a charged particle beam studying the Cherenkov photon yield seen with a teest RICH system and the prototype HPD electronics chain. This work links the laboratory timing studies with measurements performed in the testbeam, and compares the efficiency of the HPDs with predictions.

To all those who inspired me to enjoy science for its own sake. Especially my Father and Grandfathers. To their memory.

Acknowledgements

Dave Websdale, for all his support and advice throughout my PhD.
Claire, for putting up with me writing this.
Bill Cameron, for always pointing me in the right direction.
Steve Jolly, for explaining the mysteries of CERN and OPERA3D.
Trevor Savidge, for regularly managing to find just a few more centimetres.
Mitesh Patel, for his mighty effort sub-modelling the HPD plane.
Tom Blake, for being the one in the box when the magnet tripped.
Ken Wyllie, for teaching me about the LHCBPIX1.
Thierry Gys, for his valuable time spent helping me with the HPD.
Alex Howard, for thinking of distorting the HPD with a magnet.
Gianluca Aglieri-Rinella, for all his help with the HPD measurements.
Ulrik Egede, Gabriel Vidal and Richard Hallam, for their work on the photon yield.
Marcello Losasso, for his work on the RICH1 shield, and scaring us to death once.
Ann van Lysebetten, for her continuing contribution to the field measurements.
Frederic Teubert et al., for the automatic field measurements.
James Lever and Steve Jolly, for offering to proofread when they didn't have to.
James Storey and Steve Wotton, for the MAPMT testbeam.
James, Lydia, Maiko, Mike, Phil and Tim, for making the first year memorable and fun.
Alex, James, James, Rob and Simon for making *that* summer school more fun that it would otherwise have been.
Andy and Chris, for always being ready for tea.
'The Hairies', for drinking most Thursdays.
The members of Dead Karma and Gravity Prevails, for putting up with a regularly absent drummer.

Contents

List of Figures

List of Tables

Preface

This thesis presents work carried out on the development of single photon sensitive detectors and their magnetic shielding for the Ring Imaging Cherenkov counters of the LHCb experiment currently under construction at interaction point eight of the Large Hadron Collider project at CERN. The aims of the LHCb experiment are discussed, and an overview of the detector is presented. The focus then shifts to the design of the RICH detectors and their photo-tubes. The author's work on the magnetic shielding, vital to the photon detectors' operation, a study of the performance of the read-out electronics and recent tests of the photon detectors in charged particle beams are described.

Chapter 1

Physics Motivation

In 1973 Kobayashi and Maskawa[1] predicted a third generation of quarks. They required this generation to allow a complex quark mixing matrix to describe the violation of the matter-antimatter symmetry (CP violation), that had been observed in the neutral Kaon system[2] in 1964. The prescience of this prediction is notable as it was suggested before the discovery of the charm quark and any indication of a third generation.

The discovery in 1977 at Fermilab experiment 288[3] of the Υ(1S), a b anti-b meson, together with the discovery, three years previously, of the J/ψ [4][5], a charm anti-charm meson, was pivotal in establishing the quark content of the Standard Model of particle physics.

Today the B hadron family has been extended to include five resonances of the Υ and a spectrum of charged and neutral B mesons and baryons. Notable amongst the early B sector experiments is CLEO[6], an experiment on the CESR ring at Cornell. CLEO's first achievement was the discovery of the Υ(4S)[7] in 1980. Since then it has made a string of precision measurements covering the B sector, measuring the masses and lifetimes of the B^0 and $B^{\pm}$ mesons and the rate of B^0_d -$\overline{B}^0_d$ mixing[8].

Further progress in the B sector was made at higher energy colliders that allowed the production of heavier flavours at facilities such as LEP[9] and the Tevatron[10][11]. Experiments at these machines improved our knowledge of the masses, lifetimes and mixing rates of particles containing the b quark.

The large mass of the b quark and the associated enhanced coupling to the Higgs field, its relatively long lifetime and its use as a probe of CP violation have made the b-hadrons some of the most studied at current experiments. The B-Factories, *BABAR* [12] and BELLE [13], running at the $\Upsilon(4S)$ made the first observations of CP violation in the B system and have measured CP violating asymmetries in several B meson decay modes, allowing detailed measurements of the parameters of the quark mixing (CKM) matrix.

1.1 Symmetries and the Standard Model

The Standard Model of particle physics[14] is a mathematical description of the interactions between the quarks and leptons currently known to exist and three of the fundamental forces, weak, electromagnetic and strong. It includes (at least) 28 parameters. These are the values of the masses of particles, their mixing angles and phases and their coupling strengths to the gauge bosons that describe the forces. Its predictive accuracy has been one of the great successes of modern physics. One area where (until the results from the B-factories) the values of the parameters were unconstrained by measurements was the CP violating phases of the mixing matrix. CP violation is a necessary ingredient in the generation of the observed matter/antimatter imbalance in the universe[15]. The level so far observed in the strange and b-quark sector is insufficient to explain the imbalance of matter in the universe. It is likely that additional processes have been at work in the early universe. It is speculated that the recent observation of non-zero neutrino masses, that allow lepton mixing and possibly CP violation, could be the source.

CP violation is the rare contravening of what was once thought to be a universal symmetry within particle physics. Symmetry is the invariance of a physical system to a transformation, or series of transformations. Translations in time and space are examples of continuous symmetries, related to conservation of energy and momentum, whilst the parity transformation 'P' (reversing the spatial coordinates) is a discrete symmetry. Charge Conjugation is the replacement of all particles with their antiparticles, and is denoted by the C operator. CP symmetry is the application of the C operator, followed by the P operator, reversing the particle charges and the coordinate system. CP is conserved in the vast majority of situations, it is not

violated by electromagnetic interactions and has not been observed to be violated by the strong force. It is only in the weak interactions of quarks that CP violation has been observed.

1.2 The CKM Matrix

The decay of kaons by the weak interaction in processes such as $K^0(\overline{s}d) \rightarrow \pi^-$ $(\overline{u}d)$ $l^+\nu_l$ indicates that coupling between generations occurs, and that there is no equivalent to lepton number conservation in the quark sector. The terms in the Lagrangian for a flavour-changing weak interaction including the first and second quark generations can be written as:

$$\frac{g_W}{\sqrt{2}} W_\mu [\bar{\psi}_u \gamma^\mu \frac{1}{2}(1-\gamma^5)\psi_d + \bar{\psi}_c \gamma^\mu \frac{1}{2}(1-\gamma^5)\psi_s] \tag{1.1}$$

where g_W is the weak coupling strength, W_μ is the gauge field representing the charged W boson, ψ and $\bar{\psi}$ are the wavefunctions of the quarks and $(1-\gamma^5)$ is the left handed projection operator. This can be alternatively formulated as:

$$\frac{g_W}{\sqrt{2}} W_\mu \begin{pmatrix} \bar{\psi}_u & \bar{\psi}_c \end{pmatrix} \begin{pmatrix} 1 & 0 \\ 0 & 1 \end{pmatrix} \gamma^\mu \frac{1}{2}(1-\gamma^5) \begin{pmatrix} \psi_d \\ \psi_s \end{pmatrix} \tag{1.2}$$

These interactions do not include mixing between the generations. To allow this the central unit matrix must be altered to provide the cross generational coupling by adding off-diagonal terms. These have been experimentally determined to be:

$$\begin{pmatrix} 0.975 & 0.222 \\ -0.222 & 0.975 \end{pmatrix} \tag{1.3}$$

This is the Cabbibo rotation matrix[16][17].

$$V_c = \begin{pmatrix} V_{ud} & V_{us} \\ V_{cd} & V_{cs} \end{pmatrix} = \begin{pmatrix} \cos\theta_c & \sin\theta_c \\ -\sin\theta_c & \cos\theta_c \end{pmatrix} \tag{1.4}$$

The Cabbibo matrix is a unitary transformation between the mass eigenstates and the eigenstates of the weak interaction.

$$\begin{pmatrix} d_m \\ s_m \end{pmatrix} = V_c \begin{pmatrix} d_w \\ s_w \end{pmatrix} \tag{1.5}$$

So what would, in one generation of quarks, have been $u_m \mathrm{W}^- \rightarrow d_m$ becomes $u_m \mathrm{W}^-$ $\rightarrow$ (d_m cosθ_c + s_m cosθ_c), and so on. As $\theta_c \approx 13^\circ$ we see that u $\mathrm{W}^- \rightarrow d$ is the Cabbibo favoured interaction and u $\mathrm{W}^- \rightarrow s$ is Cabbibo suppressed. This explains why the decay rate $K^- \rightarrow \mu\ \bar{\nu}_\mu$ is less than that for $\pi^- \rightarrow \mu\ \bar{\nu}_\mu$.

CP violation is a consequence of a phase in the quark mixing matrix. However adding a complex phase to the Cabbibo matrix has no effect, as it can be removed by redefining the quark fields with a compensating phase that does not appear in the final Lagrangian.

In order to obtain a phase that cannot be absorbed into the quark wave functions it is necessary to introduce the third generation. The full three generation mixing matrix is the Cabbibo Kobayashi Maskawa (CKM) matrix:

$$V_{CKM} = \begin{pmatrix} V_{ud} & V_{us} & V_{ub} \\ V_{cd} & V_{cs} & V_{cb} \\ V_{td} & V_{ts} & V_{tb} \end{pmatrix} \approx \begin{pmatrix} 0.975 & 0.223 & 0.003 \\ 0.222 & 0.974 & 0.040 \\ 0.009 & 0.039 & 0.999 \end{pmatrix} \tag{1.6}$$

where the numerical values have been measured[18] and are not predicted by the Standard Model. In terms of mixing angles $\theta_{12}, \theta_{23}, \theta_{13}$ and phase δ_{13} where s_{12} denotes $\sin\theta_{12}$ etc, the CKM matrix is

$$V_{CKM} = \begin{pmatrix} c_{12}c_{13} & s_{12}c_{13} & s_{13}e^{-i\delta_{13}} \\ -s_{12}c_{23} - c_{12}s_{23}s_{13}e^{-i\delta_{13}} & c_{12}c_{23} - s_{12}s_{23}s_{13}e^{-i\delta_{13}} & s_{23}c_{13} \\ s_{12}s_{23} - c_{12}c_{23}c_{13}e^{-i\delta_{13}} & -c_{12}s_{23} - s_{12}c_{23}s_{13}e^{-i\delta_{13}} & c_{23}c_{13} \end{pmatrix} \quad (1.7)$$

A useful parameterisation was developed by Wolfenstein[19]:

$$V_{CKM} = \begin{pmatrix} 1 - \frac{1}{2}\lambda^2 & \lambda & A\lambda^3(\rho - i\eta) \\ -\lambda & 1 - \frac{1}{2}\lambda^2 & A\lambda^2 \\ A\lambda^3(1 - \rho - i\eta) & -A\lambda^2 & 1 \end{pmatrix} + \mathcal{O}(\lambda^4) \quad (1.8)$$

In this parameterisation we define $s_{12} = \lambda$ and then expand V_{CKM} up to $\mathcal{O}(\lambda^3)$. With $s_{23} = A\lambda^2$ and $s_{13}e^{-i\delta_{13}} = A\lambda^3(\rho - i\eta)$.

The presence of complex components implies that CP violation will occur in b hadron decays that involve couplings of $b \to u$ and $t \to d$ quarks. The sensitivity of the measurements made by LHCb will be such that it becomes necessary to extend the precision of the above parameterisation beyond λ^3. When we do this we find that there are new imaginary contributions in the $c \to d$ and $t \to s$ transitions:

$$\begin{aligned} \mathcal{I}m[V_{cd}] &= -A^2\lambda^5\eta \\ \mathcal{I}m[V_{ts}] &= -A\lambda^4\eta \end{aligned} \quad (1.9)$$

1.3 CP Violation and the Unitarity Triangles

The CKM matrix provides the transformation between the mass and weak interaction eigenstates, and so is constrained by the condition that the matrix is unitary:

$$V_{CKM} \begin{pmatrix} d_w \\ s_w \\ b_w \end{pmatrix} = \begin{pmatrix} d_m \\ s_m \\ b_m \end{pmatrix} \quad (1.10)$$

This provides us with nine unitarity conditions, six of which are orthoganality conditions:

$$\begin{aligned}
&1) \quad V_{ud}V_{us}^{\star} + V_{cd}V_{cs}^{\star} + V_{td}V_{ts}^{\star} = 0 \\
&2) \quad V_{ud}V_{ub}^{\star} + V_{cd}V_{cb}^{\star} + V_{td}V_{tb}^{\star} = 0 \\
&3) \quad V_{us}V_{ub}^{\star} + V_{cs}V_{cb}^{\star} + V_{ts}V_{tb}^{\star} = 0 \\
&4) \quad V_{ub}^{\star}V_{cb} + V_{us}^{\star}V_{cs} + V_{ud}^{\star}V_{cd} = 0 \\
&5) \quad V_{ub}^{\star}V_{tb} + V_{us}^{\star}V_{ts} + V_{ud}^{\star}V_{td} = 0 \\
&6) \quad V_{cb}^{\star}V_{tb} + V_{cs}^{\star}V_{ts} + V_{cd}^{\star}V_{td} = 0
\end{aligned} \tag{1.11}$$

Six of the values of the CKM matrix can be measured directly and using the unitarity constraints the ranges of the others can be narrowed. The uncertainty divided by the CKM value is shown below for each element.

$$\sigma_{CKM}/V_{CKM} = \begin{pmatrix} 0.0012 & 0.027 & 0.432 \\ 0.027 & 0.0014 & 0.12 \\ 0.979 & 0.15 & 0.0002 \end{pmatrix} \tag{1.12}$$

These numbers were taken from the PDG[18] in 2005. From this we see that (at the time) significant levels of uncertainty remained in V_{ub}, V_{td}, V_{ts} and V_{cb}.

The conditions in 1.11 relate to six triangles that can be plotted on the Argand diagram. Of the triangles produced, only those from 2) and 5) have sides of similar order length and so have accessible angles. Three of the more uncertain parts of the matrix are also present in these triangles making them a useful tool to study the relationships between the matrix elements. The two triangles are normalised by dividing by the $V_{cd}V_{cb}^{\star}$ term, producing the following equations:

$$\begin{aligned}
\frac{V_{ud}V_{ub}^{\star}}{V_{cd}V_{cb}^{\star}} + 1 + \frac{V_{td}V_{tb}^{\star}}{V_{cd}V_{cb}^{\star}} = 0 \\
\frac{V_{ub}^{\star}V_{tb}}{V_{cd}V_{cb}^{\star}} + \frac{V_{us}^{\star}V_{ts}}{V_{cd}V_{cb}^{\star}} + \frac{V_{ud}^{\star}V_{td}}{V_{cd}V_{cb}^{\star}} = 0
\end{aligned} \tag{1.13}$$

The triangles these produce are shown below:

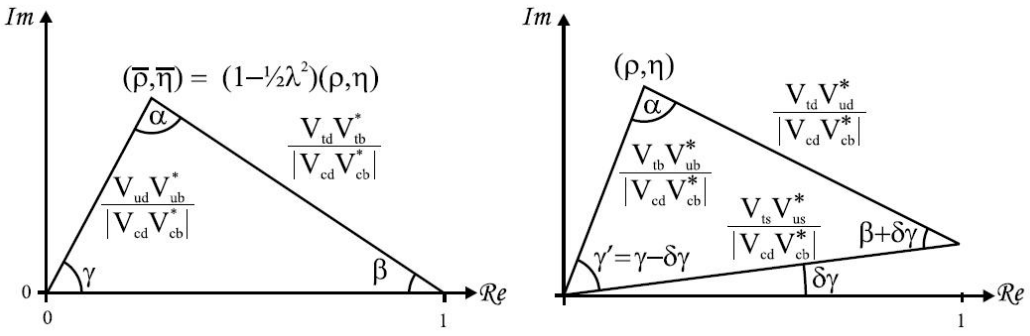

CP violation has been observed in three different regimes; mixing, decay and interference [20]. CP violation in mixing, also called indirect CP violation, is in essence an asymmetry in the rate of $B^0 \to \overline{B}^0$ and $\overline{B}^0 \to B^0$. It is caused by a complex phase being present in the mixing amplitudes. It has been well studied in the K sector, but is expected to be vanishingly small in the B sector. CP violation in decay, also called direct CP violation, is the difference between the rate of a decay, and the rate of its CP conjugate. This has also been studied in the K sector, although the measurements are extremely difficult and have only recently confirmed a non-zero observation[21][22]. The final method is CP violation in the interference between decays with and without mixing. This is a route by which both a neutral particle and its antiparticle can decay to the same final state, allowing the phase difference to result in a measurable CP violating effect. CP violation in mixing (indirect CPV) was observed at *BABAR* and BELLE in 2001 in the channel $B^0 \to J/\psi\ K_s$ [23][24], whilst direct CP violation in the B sector was observed at *BABAR* in July 2004 in the channel $B^0 \to K^+\ \pi^-$ [25].

1.4 The B Mixing Rates

B^0-$\overline{B}^0$ mixing, like K^0-$\overline{K^0}$ mixing is the oscillation of a neutral meson into its antiparticle, without any external interaction. This is a consequence of a lack of the flavour conservation in weak decays described by the CKM matrix. The method was originally proposed by Gell-Mann and Pais[8] in 1955 and was first observed in the K sector in 1956. In both the B^0 and K^0 cases the interaction takes place though a 'box' Feynman diagram of the type shown below for the B^0 system. Since the contribution increases with the mass of the particle in the loop, it is the t quark

that dominates, hence the the CKM elements that are indicated in the vertices.

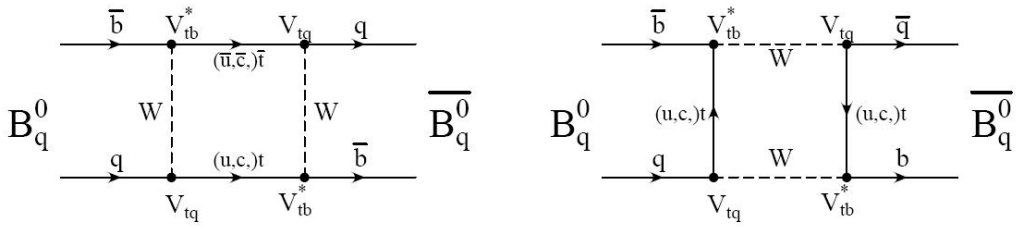

As with other mixing schemes, mixing in the B sector is governed by the mass difference between the two mass eigenstates, also referred to as mass splitting, giving the parameters Δm_d and Δm_s for B_d and B_s respectively. These are important parameters in CKM physics since they determine one of the sides of the unitarity triangles, and thus feed into the CKM constraints of the Standard Model of CP violation. B^0 mixing also provides access to the CKM terms V_{td} and V_{ts} through B_d and B_s mixing respectively.

1.5 B-Physics at LHCb

The LHCb experiment at the CERN LHC is designed to be a dedicated B-physics detector. The LHC luminosity, the high collision energy and the detector layout offer advantages over previous and current detectors at CLEO, LEP, the Tevatron and the B-factories. In addition the dedicated design allows a better B-physics performance than the LHC general purpose detectors ATLAS & CMS.

1.5.1 High Luminosity

The nominal LHCb luminosity is $2\times10^{32}\text{cm}^{-2}\text{s}^{-1}$. This provides a maximum number of bunch crossings with a single p-p collision and a yield of 10^{12} b-hadrons in one year. LHCb will have access to a larger sample of B decays than any previous experiment.

In this regard it is only outperformed by ATLAS and CMS that run at the full

LHC luminosity of 10^{34} cm^{-2}s^{-1}. However without hadron identification, it is not possible for them to obtain the necessary background suppression, except in B decay channels involving leptons[26].

As well as making measurements with very high statistics, this luminosity gives LHCb the opportunity to examine events of extreme rarity, with branching fractions of less than 10^{-7}. These rare decays often give an insight into physics beyond the Standard Model. This is especially so in cases where loops are involved in the underlying quark interactions and the presence of new physics can compete with the (very small higher order) Standard Model flavour-changing neutral currents.

1.5.2 Access to the B_s Sector

Whilst LHCb is certainly not the first particle detector to have access to B_s decays, it is the first to combine this with an arsenal of tools dedicated to making B-physics measurements. Important measurements that can be accessed through B_s decays include the B_s mixing parameter Δm_s, that constrains the length of one side of the unitarity triangle, and independent measurements of the CP angle γ. These will both constrain the Standard Model and probe for new physics by comparison with γ measurements obtained through B_d decays. Recent Δm_s measurements[27][28] from the Tevatron experiments, D0 and CDF, have demonstrated that this parameter is within reach of the LHCb proper time resolution.

This access to the B_s sector distinguishes LHCb from the current generation of dedicated B-experiments. *BABAR* and Belle have explored the physics of the B_d and B_u systems resulting in high precision measurements of the CKM parameters accessible. Although it is possible to increase the e^+e^- collision energy to produce B_s mesons, it is only at the expense of a lower luminosity, or at a less asymmetric beam energy, resulting in a loss of precision in the proper lifetime of the decaying b-hadrons.

1.5.3 Detector Design Considerations

The unique features of LHCb, important for B-physics measurements, are its ability to find and resolve the production and decay vertices of B particles and to identify hadrons in the decay products. The vertex detector allows a precise determination of the proper lifetime, and access to the oscillation period of both B_d and B_s mixing. LHCb can thus use decays, such as $B_d \to \pi^+\pi^-$ [29] and $B_s \to D_s\ K$ [30], unavailable at general purpose detectors due to the large backgrounds that can only be suppressed by hadron identification. Similarly the CP asymmetry in the decay $B_s \to J/\psi\ \phi$[31], combined with the precision vertexing allows the determination of the higher order CP angle $\delta\gamma$.

Chapter 2

The LHCb Detector

LHCb is designed to take maximum advantage of the high rate of $b\bar{b}$ pair production at the LHC, which will be the most copious source of b quarks ever constructed. A large number of B mesons and baryons will be produced, giving access to many channels with low branching fractions, and phenomena such as B_d and B_s mixing. Studies using the PYTHIA event simulation have shown that the majority of $b\bar{b}$ pairs will be produced in forward-backward cones, as shown in Figure 2.1. This allows a detector of limited polar angle acceptance. Furthermore since both b-hadrons are emitted in the same (forwards or backwards) cone, an asymmetric design, reminiscent of a fixed-target experiment has been adopted: a forward arm spectrometer with an acceptance between 10 and 300mrad. The LHC beam transport optics have been adjusted to offset the LHCb interaction point by 11.5m from the centre of the former LEP-DELPHI cavern. This offset corresponds to three interaction separation units with the LHC bunch-crossing frequency of 40MHz, and results in the optimum use of available space in the cavern.

To make significant measurements LHCb is required to identify the products of b-hadron decays. To do this it uses a dipole magnet and tracking system to provide a momentum measurement for charged particles; a vertexing system to measure the 'proper lifetime' (decay length) of b-hadrons; a Ring Imaging Cherenkov system to determine the velocity of charged particles and separate light mesons and thus identify pions, kaons and protons; a calorimeter system to separate electrons, photons and hadrons and provide a transverse energy measurement for the trigger system and a muon detector system to identify muons and make a transverse momentum

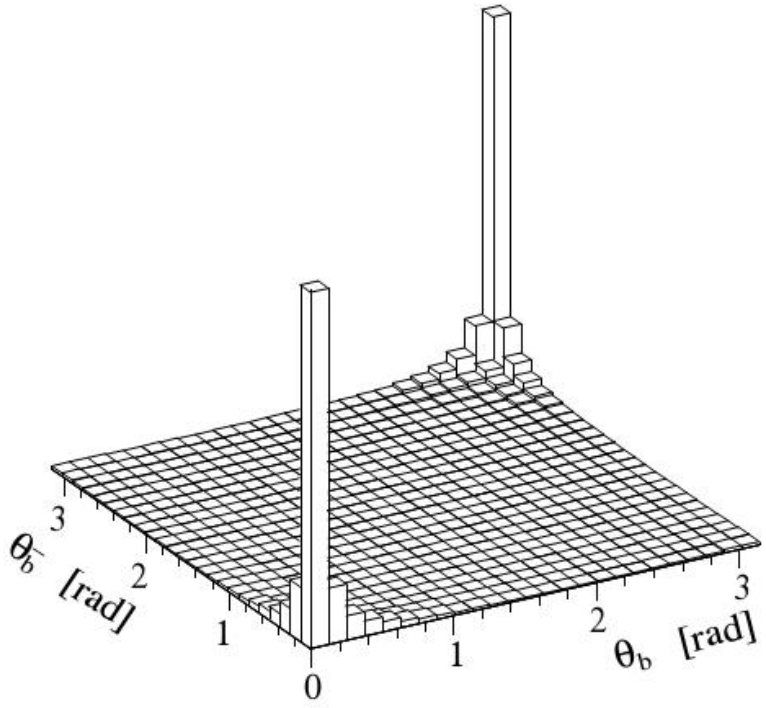

Figure 2.1: The polar angles of b-hadron pair production in LHC collisions.

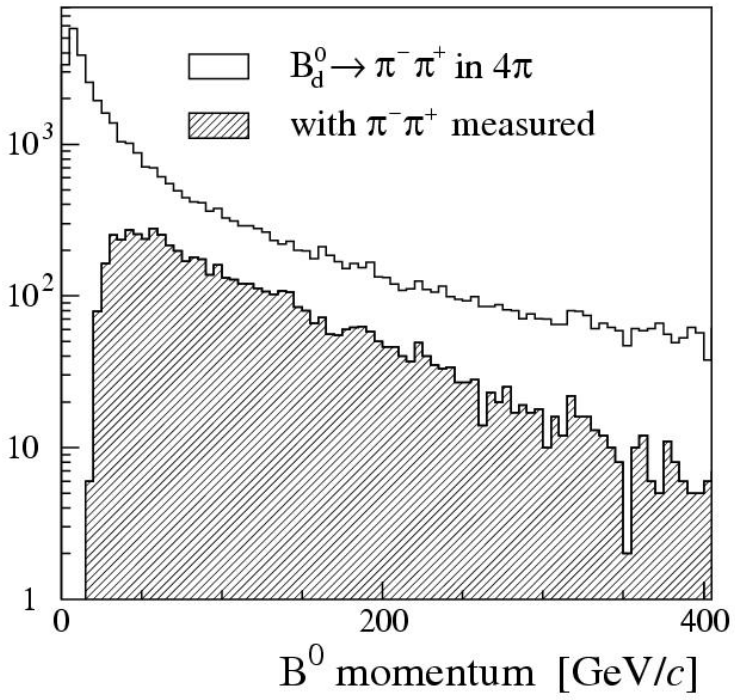

Figure 2.2: The momentum distribution of $B^0_d \to \pi^+\pi^-$ into a 4π solid angle for measured and unmeasured pions.

measurement, again for the trigger. Figure 2.2 shows the momentum distribution of B^0 mesons, where the shaded area corresponds to those detected and measured in the LHCb detector. The loss is due to low momentum pions, swept out of the detector by the magnet and high momentum pions that remain below the 10mrad acceptance.

Due to the very high rate of LHC interactions, a trigger system is required to select interesting events and reduce the data rate to a level that can be recorded. This is achieved by a combination of high transverse momentum measurements and the reconstruction of primary and secondary decay vertices.

The LHCb coordinate system is designed to be right handed, with the x-axis horizontal, y vertical and z along the beamline, with the origin at the interaction point. A brief description of the LHCb sub-detectors is presented in this chapter. Technical details can be found in the Technical Design Reports (TDR)[33] to [44] and subsequent updates as appropriate[45], [46].

The detector design was re-optimised[45] in 2002 to reduce the level of particle interactions with the material of the tracking stations within the dipole magnet. This would otherwise have resulted in an unacceptable loss of efficiency in reconstructing events with high track multiplicity. This led to a series of changes to the design of LHCb, collectively referred to as the 'lite' redesign. It includes changes to the tracking system, vertexing system, upstream magnetic shielding and the Ring Imaging Cherenkov system. This reoptimised design is shown in Figure 2.3.

2.1 The Beampipe

The LHCb beampipe separates the LHC primary vacuum and circulating beams from the detectors of LHCb with the exception of the vertexing system which is housed within a secondary vacuum region. To minimise the probability of particles scattering in the material of the beampipe, it is designed to have a very long radiation length, especially in the upstream region. To maintain the LHC primary vacuum the beampipe must be periodically baked out at 250°C. This drives off any substances that may expel gas later and reduce the quality of the vacuum. As the beampipe traverses the entire experiment it affects all the LHCb sub-detectors.

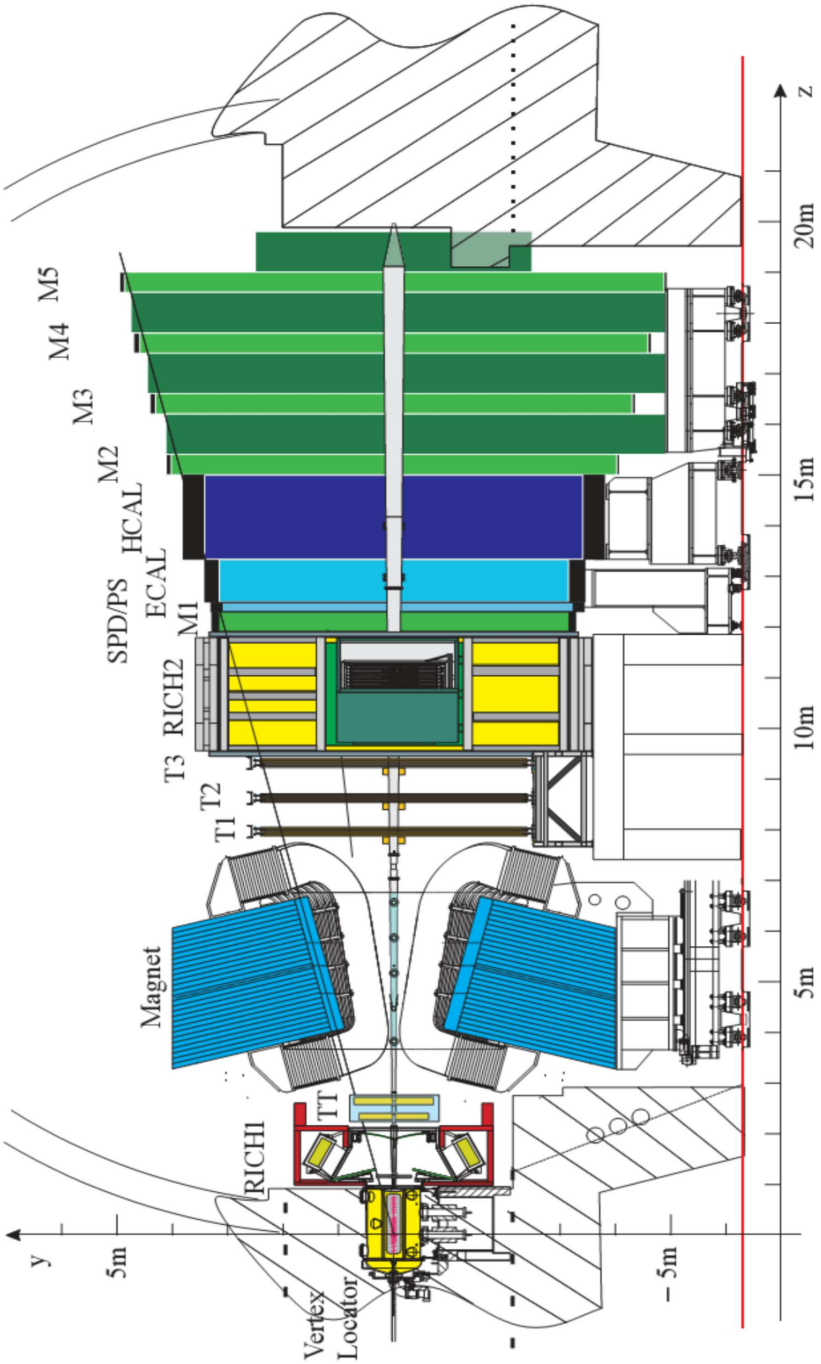

Figure 2.3: The layout of the sub-detectors in the non bending plane of LHCb[45]. The tracking stations are labelled TT, T1, T2 & T3 and the muon stations are labelled M1 to M5.

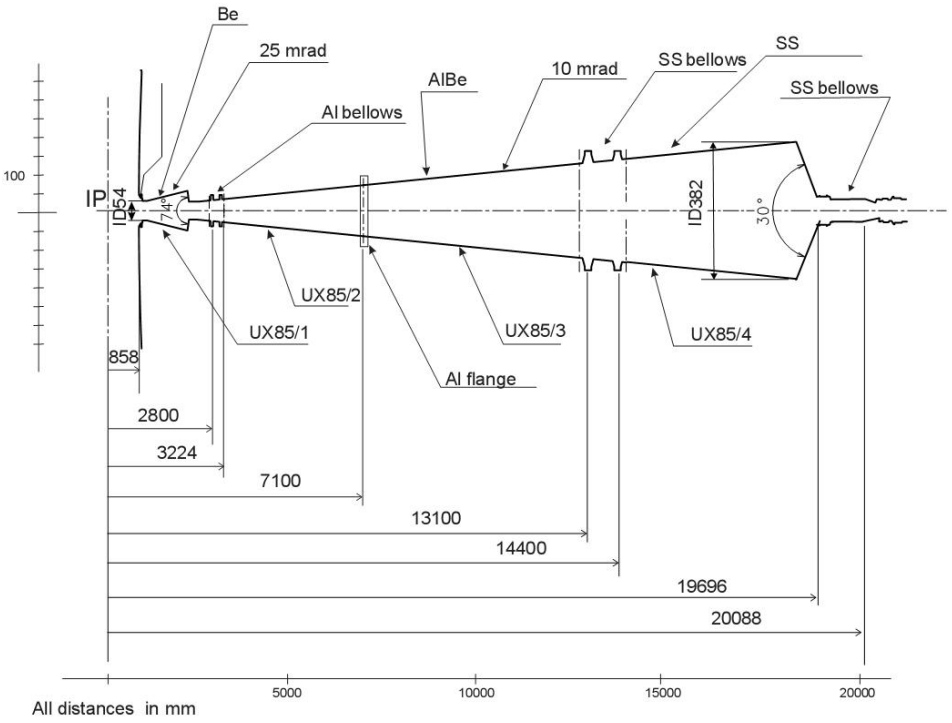

Figure 2.4: The design of the LHCb beampipe.

The beampipe consists of an exit window on the vertexing system and two concentric cones shown in Figure 2.4, the first with a 25mrad angle and the second with a 10mrad angle. The exit window is 2mm thick, covers an acceptance of 390mrad and is machined out of an aluminium alloy. This is welded to a 1840mm long beryllium section that forms the 25mrad cone and start of the 10mrad cone. A flange at the end of this section connects it to the next beryllium[1] section via aluminum bellows to allow some compliance and minimise stresses on the aluminum window. This section, made in two pieces and connected by a flange extends to 13m from the interaction point and is then joined to a stainless steel cone via another bellows. Several prototype sections of the beampipe have been manufactured and bake-out procedures are in place for each of the sections.

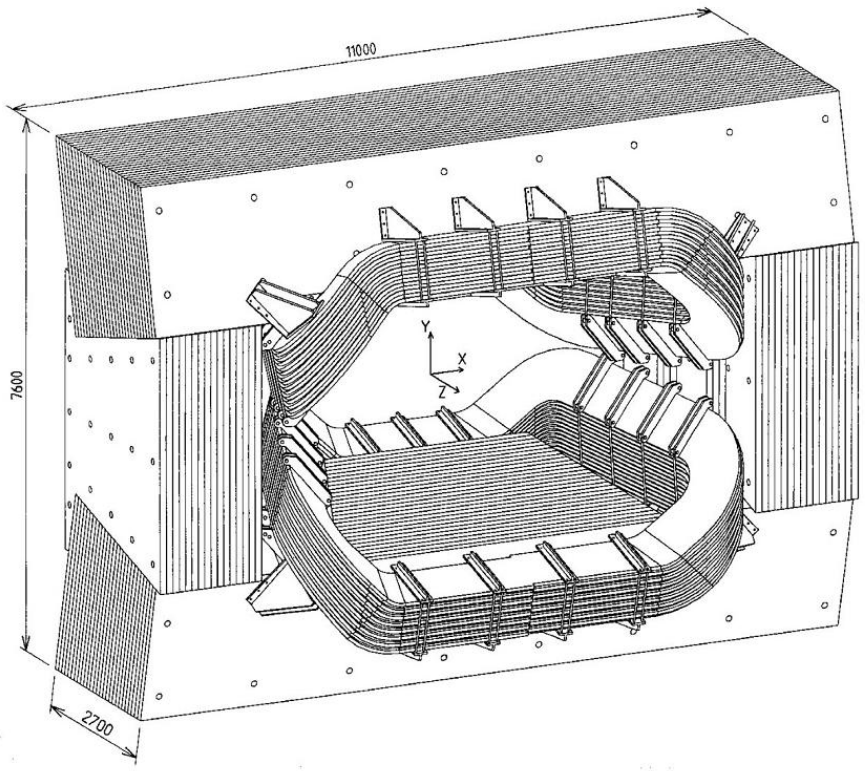

Figure 2.5: View of the LHCb dipole magnet from the downstream side. Dimensions are in millimetres.

2.2 The Dipole Magnet

The LHCb dipole magnet[42] is designed to bend the path of charged particles passing through the experiment to allow a momentum measurement to be performed. It is situated between the TT and T1 tracking stations, providing an integrated field of 4Tm along 10m of the beamline, with a peak intensity of 1.1T. It is a warm iron (non-superconducting) magnet, that consumes approximately 5MW of power.

The opening of the magnet, surrounded by the coils and the return yoke, follows the LHCb acceptance. The water-cooled coils, made from 15 layers of 15 turns of 50mm square aluminium, each carry 5.8kA. There is a channel running through the centre of each coil that carries cooling water. A diagram of the magnet is shown in Figure 2.5.

Since the LHC proton beams traverse the magnet they are subject to bending. Correcting dipoles are inserted into the LHC lattice to compensate for the distortion of the beam optics.

2.3 The VELO

The VErtex LOcator (VELO)[34] is the tracking system immediately surrounding the LHCb interaction point. Its main function is to determine the positions of the primary and secondary decay vertices of b-hadrons. This high resolution tracking is designed to allow precise measurements of b-hadron proper lifetime and provide a high efficiency trigger on displaced decay vertices. It also provides the principal tracking information upstream of the magnet.

The VELO is made up of semi-circular silicon strip tracking planes. These have azimuthal and quasi-radial strips that measure r and ϕ respectively, implanted on one side of a pair of back to back silicon wafers. There are 21 planes arranged along the beamline close to the interaction point, with their positions chosen to optimise the resolution of the impact parameter of tracks relative to the primary vertex, and to decrease the likelihood of multiple Coulomb scattering in the silicon. The

[1]This is labelled as AlBe in Figure 2.4 but has since been changed to beryllium.

thickness of the silicon planes is 220 μm, chosen to provide an acceptable signal to noise ratio in the measurement of the charge deposited by traversing particles. The sensor strips have a pitch of between 35 and 100 μm, varying with radius on the azimuthal planes. The planes themselves have an active area bounded by the 8mm and 40mm radii. The design was limited to a maximum of 200,000 analogue channels by the space required to route the data lines through the walls of the vacuum vessel.

Two additional planes, upstream of the interaction point, provide a pile-up veto for the Level-0 trigger. This allows an estimate of the number of vertices in an event to be made, and any multiple interactions rejected. The veto stations have only radial sensitivity to reduce the probability of scattering.

To maximise their effectiveness the VELO planes operate as close as possible to the LHC circulating beams. This leads to the planes being operated in a secondary vacuum, separated from the LHC primary vacuum by a 300μm-thick aluminium foil, which is contained by the VELO housing. Protecting this vacuum is extremely important, as a failure would cause a loss of the LHC beam and probably damage to the LHCb detectors. As the diameter of the beam immediately after injection is much larger than it is in stable operation, the planes form two halves that can be retracted 30mm when necessary. The planes in opposing halves are offset by 15mm in z, to allow the sensitive regions of each half station to be bought into a position where full coverage is achieved. The planes and their read-out electronics are protected from the radio frequency signals generated by the circulating beams by the foil that encloses each half of the detector. The silicon detector planes, foils and housing are shown in Figure 2.6.

Tests carried out on the VELO components indicate that the detector will achieve a precision in x/y of $\sigma_{x,y} = 10\,\mu$m. This precision allows the VELO to make a proper time measurement with a precision of 45fs in a typical B-decay channel. The VELO silicon planes will operate in a very harsh radiation environment, with their innermost regions subject to the equivalent neutron flux of $1.3 \times 10^{14}\text{cm}^{-2}$ per year. Under these conditions it is expected that the sensors will have to be replaced every three years of operation at nominal luminosity.

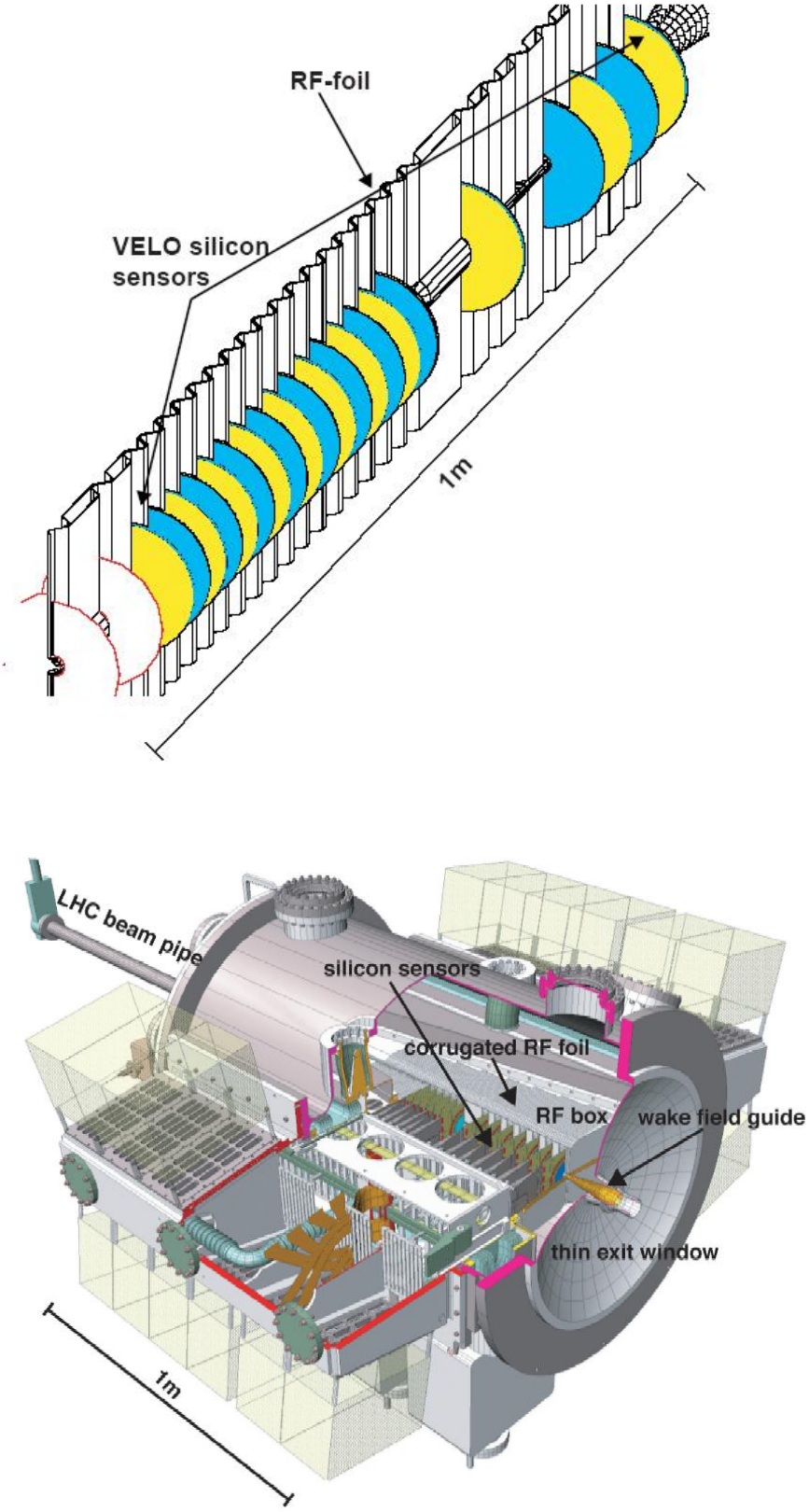

Figure 2.6: (top) The orientation of the VELO tracking planes. (bottom) The VELO vacuum vessel.

2.4 The RICH System

As described in Chapter 1, high-efficiency separation of pions and kaons is vital to the performance of LHCb, as the $b \to c \to s$ decay chain leads to a high proportion of B meson events producing a Kaon. These are separated from the pion background by the Ring Imaging Cherenkov RICH detectors[35], [45]. The Cherenkov light emitted by a charged particle in a transparent radiator medium is used to make an accurate determination of the particle's velocity.

To cover the required momentum range from 1GeV/c to beyond 100GeV/c the LHCb RICH system uses three radiators. Silica aerogel, used for the identification of low momentum particles, and C_4F_{10} gas are located in RICH1, immediately downstream of the VELO. A CF_4 gas radiator is located in RICH2 between the tracking stations and the calorimeters (Figure 2.3).

Spherical mirrors focus the cones of light produced in the radiators to form rings on photon-detector planes, made up of single-photon-sensitive Hybrid Photon Detectors. These phototubes use an electrostatic field to accelerate photoelectrons from a photocathode at the HPD entrance window onto a silicon pixel detector. Their performance is degraded by the presence of magnetic fields and so must be shielded from the LHCb dipole magnet, a requirement described in more detail in Chapter 4. The other design features of the RICH system are described in Chapter 3.

2.5 The Tracking System

In addition to the VELO, LHCb has four tracking stations placed perpendicular to the beamline: the Trigger Tracker(TT)[45], T1, T2 and T3. These stations form a system that records the trajectories of charged particles within the detector. Using this information the momenta of charged particles passing through the dipole magnet can be measured. The tracks reconstructed will be critical to interpreting the data from the other sub-detectors, including the location of rings in the RICH detectors, energy clusters in the calorimeters and tracks in the muon filters.

The TT is the furthest upstream station, located between RICH1 and the magnet.

Information from the TT and VELO is used in the Level-1 trigger (hence the name of "Trigger Tracker") to make an initial estimation of the transverse momentum of individual tracks, and thus enrich the selection of a heavy flavour interaction. T1, T2 and T3 are situated between the magnet and RICH2 providing tracking information for high-momentum charged particles that have passed through the magnet.

Owing to the higher density of particles close to the beampipe each downstream station is divided into an Inner Tracker (IT)[36] and an Outer Tracker (OT)[37]. The division between the two regions is set by requiring an occupancy of less then 10% in any readout channel. Thus the IT has finer granularity and uses silicon strip technology while the OT uses straw chamber technology.

The Inner Tracker stations and the TT are similar silicon microstrip devices, with a track pitch of 198μm. The TT consists of two planes of two $\pm 5^o$ stereo layers, separated by 30cm to provide a measurement with good angular resolution. Each Inner Tracker station has two pairs of stereo layers without the separation.

The Outer Tracker is constructed from 5mm diameter straw drift tubes packed into 5m-long by 34cm-wide modules. The tubes are arranged in a double layer within each module to give a better efficiency and spatial resolution. The 5mm diameter of the tubes is dictated by the requirement for a maximum drift time of 50ns, which can be tuned by adjusting the gas mix to different proportions of Argon, CO_2 and CF_4. The 50ns drift time (corresponding to two LHC bunch crossings) was set to reduce spillover effects and limit the channel occupancy.

Data from all the stations in the tracking system are available to the Level-1 trigger, although at the time of writing only information from the TT is planned to be used in the Level 1 algorithms. This is revisited in more detail in Chapter 4.

Data from the VELO will be combined with the tracking information during the offline analysis to reconstruct the, approximately, 75 charged tracks in an average event. Of these tracks 40% are products of the primary pp interaction, the others being caused by secondary interactions and photon conversion within the detector material. Tracks with a momentum lower than 3GeV/c will be bent out of the acceptance by the magnet and will only be present in the VELO and the TT. Figure 2.7 shows a simulated event in the tracker, with some tracks passing through all the detectors, some seen only in the VELO and TT and some seen only in T1-T3.

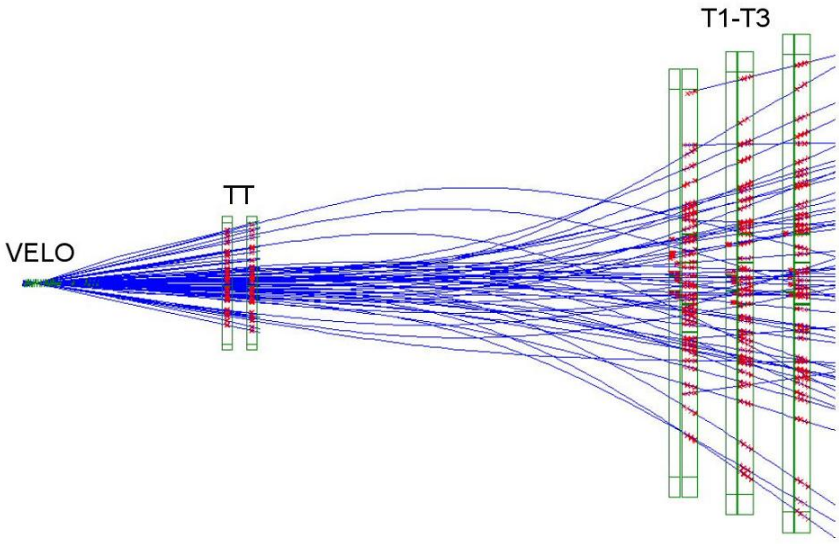

Figure 2.7: A simulated event in the tracking system[36].

Tracks detected in the VELO and the TT are used to make an initial transverse momentum measurement that informs the Level-1 trigger. Tracks between the TT and T1-T3 are reconstructed offline to give an accurate momentum measurement.

The precision of the tracking systems is limited by multiple scattering, resulting in an uncertainty of $\delta p/p = 0.003$. This translates into an uncertainty on the mass of a fully reconstructed B meson in a typical $B \rightarrow \pi^+\pi^-$ event of approximately 10MeV/c^2. The IT and TT microstrip systems provide a spatial resolution of $60\,\mu$m and the OT straw tube detectors provide a resolution of $100\,\mu$m. The maximum occupancy in the detectors has been estimated to be below the required 10% level, with the OT at 9.1% the IT at 2.3% and the TT at 4%[47][48].

2.6 The Calorimeter System

The LHCb calorimeters[38] are positioned downstream from RICH2, before the main muon stations. Their purpose is to measure the energy of all charged and neutral interaction products except muons and neutrinos. This measurement is used in the Level-0 trigger to select interactions with high transverse energy, resulting from the decay of heavy b-hadrons. There are four components to the calorimeter system.

Going from up to downstream these are a Scintillating Pad Detector (SPD) followed by a Pre-Shower detector (PS), an electromagnetic calorimeter (ECAL), and a hadron calorimeter (HCAL).

The SPD and PS provide electron identification to the Level-0 trigger. The SPD consists of a plane of 15mm thick scintillator tiles, and provides separation between charged and neutral particles, allowing the discrimination of electrons from photons. Immediately downstream is the PS, consisting of a lead plate 2.5 radiation lengths thick (12mm), immediately followed by another layer of scintillator tiles. The PS differentiates electrons and hadrons by their different interaction lengths; electrons deposit far more energy in the thin lead plate than the predominantly pion background.

The ECAL and HCAL are both sampling calorimeters constructed from interleaved layers of high density material and scintillator tiles. Charged particle showers caused by the dense regions are 'sampled' by the layers of scintillator. Recording the progression and penetration of these showers allows the energy of the original particle to be calculated. The light in the scintillator tiles is read out using a wavelength-shifting fibre, connected to a multi or single-anode photomultiplier tube. The ECAL scintillator tiles are 2mm thick separated by 4mm lead sheets aligned perpendicularly to the beamline. This is designed to sample optimally the well-collimated electromagnetic showers produced by photons and electrons. The HCAL tiles are aligned edge-on to the beamline, optimised for the more divergent hadronic showers. The tiles are 200mm deep and 4mm thick, separated by 16mm of iron in x and 200mm of iron in z. Figure 2.8 shows the ECAL and HCAL tile arrangement and the connection of the wavelength shifting fibre to the scintillators.

The calorimeter tiles are arranged so that the boundaries in the four stations are aligned and converge on the interaction point. This "projective geometry" makes clustering and combining measurements in the trigger far simpler. The tile pitch is increased as the particle flux increases; closer to the beampipe the ECAL tiles are 40mm square, whilst at the edges of the acceptance they grow to 120mm by 120mm.

A predicted ECAL energy resolution of $\frac{\sigma_E}{E} = \frac{(9.4 \pm 0.2)\%}{\sqrt{E(GeV)}}$ and a predicted HCAL resolution of $\frac{\sigma_E}{E} = \frac{(79.2 \pm 2.9)\%}{\sqrt{E(GeV)}}$ have been verified using measurements in charged

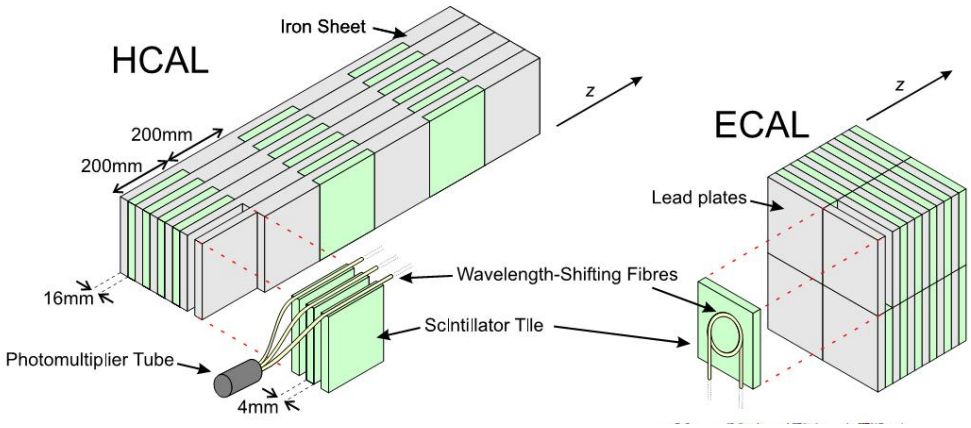

Figure 2.8: The ECAL and HCAL scintillator tile arrangements.

particle beams and satisfy the requirements presented in the TDR. This enables the calorimeters to have a mass resolution on a π^0 equal to 10MeV/c^2.

2.7 The Muon Detector Stations

The muon system[39], [40], [41] provides vital information to the Level-0 trigger, as well as having a critical role in detecting the final states of several important b-hadron decays. It provides up to 30% of the Level-0 trigger rate primarily by detecting high transverse momentum muons that indicate the presence of a semi-leptonic decay of a high mass (heavy flavour) particle.

The system consists of five stations, planes sensitive to charged tracks, M1 to M5, each separated into four concentric regions of increasing granularity towards the centre. The stations follow a projective geometry similar to that of the calorimeters, with the edges of the chambers and regions pointing to the interaction point. M1 is situated between RICH2 and the calorimeter system, with M2 to M5 behind the calorimeter system and separated from it by a series of 800mm-thick iron hadron filters. Of the stations, M1, M2 and M3 are used for track finding (and hence the calculation of the muons' momenta), and M4 and M5 are used to positively identify the particle as a muon. To reach M5 a charged particle needs to have penetrated 30 interaction lengths of iron. M1 and M2 are separated by the depth of the calorimeter systems, to provide a long enough lever arm to make an accurate

transverse momentum measurement.

The principal instrumentation in the muon system consists of MultiWire Proportional Chambers (MWPC), each a gas-filled 5mm gap with central wires and high voltage cathode pads. A muon traversing the gap produces ∼50 electrons in the gas, which drift towards, then avalanche at the wires under the influence of a ∼3kV potential. The signal produced in the wires is then amplified and read out. Four chambers are placed one behind the other and connected as two double gaps to produce a station with an efficiency in excess of 99%. MWPCs were chosen as the primary instrumentation due to their high sensitivity and good radiation tolerance.

The inner region (approximately ±40cm around the beampipe) of the upstream M1 station is subjected to a very high particle intensity and is instrumented with a triple Gas Electron Multiplier (GEM) detector [41]. This detector consists of a primary ionisation gap and three gas electron multiplier foils. These cause a cascade of electrons in the gas, and cathode strips detect an induced current from the electron cloud drifting from the last stage.

The muon system is anticipated to allow the Level-0 muon trigger to operate with an efficiency of 55.2% ± 0.9% for $b \to \mu$ X events. It permits the offline reconstruction of muons with a momentum over 5GeV/c with an efficiency of greater than 90% with a probability of less than 1.5% that a pion can be misidentified as a muon.

2.8 The Trigger System

In common with the majority of other modern particle physics experiments, the rate at which data are produced at LHCb will be far larger than the capacity available to record and store it. To allow the experiment to discard events that are less likely to contain decays of interest, a trigger system selects which events are to be recorded. The LHC bunch crossings will occur at a rate of 40MHz. For LHCb the beams will be defocused to optimise the occurrence of single collisions. This produces a mean interaction rate of 12MHz, (of which 9MHz comes from single interactions and 3MHz is from multiple interactions) which in turn leads to a mean $b\bar{b}$ production rate of 100kHz. Of these events only about 30% have decay products that remain within the LHCb acceptance. The branching fraction of B interactions of interest is

typically less than 10^{-3} which leads to a rate of the order of tens of events per second for a given decay channel. This means the trigger [43], [44] has the responsibility of reducing the rate from 40MHz to 200Hz. To do this efficiently, with the minimum necessary buffering, the task has been separated into three levels of decision: Level-0, Level-1 and the Higher Level Trigger (HLT). The corresponding input and output rates are shown in Table 2.1 for each level.

	Level-0	Level-1	HLT
Input rate	40MHz	1MHz	40kHz
Output rate	1MHz	40kHz	200Hz
Sub-detectors Used	VELO, Muon Calorimeters	All but RICH T1-T3	All but RICH

Table 2.1: The input and output rates of the three levels of the trigger system and the sub-detectors used in the initial algorithms.

The Level-0 trigger is implemented in custom, on-detector, electronics and is designed to run at the full 40MHz LHC interaction rate to avoid losing any events that occur in consecutive bunch crossings. Each sub-detector readout channel buffers 4μs (160 bunch crossings) of data to give the trigger time to make a decision, and to propagate it throughout all sub-detector readout electronics.

The Level-0 uses the pile up veto from the VELO, transverse energy information from the calorimeter system and transverse momentum information from the Muon system to reach a decision. The VELO pile-up stations are used to reconstruct quickly tracks that allow single-interaction events to be selected. Fast reconstruction algorithms are used to determine rough transverse energy and momentum measurements that are the signature of a heavy flavour decay.

The Level-1 trigger is run on a processor farm in the counting room. Custom electronics in the counting room—the TELL1 and UK1 boards—read the data from the Level-0 units across the detector, apply zero suppression and a common formatting and pass it via a high speed network switch (the event builder) to the farm over multiple gigabit ethernet links. In addition to the Level-0 information, the initial implementation for the Level-1 trigger will use information from the TT and the VELO. The Level-1 algorithm has to take the 1MHz rate from the Level-0 trigger and reduce it to 40kHz. The system is designed to be upgradable to include information from the T1-T3 tracking stations and the M2-M5 muon stations. In the

present scheme more detailed transverse momentum measurements are made on the low momentum VELO to TT tracks (swept out of the acceptance by the magnet), and on tracks in the muon system and calorimeter that are matched with tracks in the VELO and TT. The final selection is made based on tracks with a large transverse momentum, large impact parameter from the primary vertex and thus a high probability of having originated from a heavy flavour decay.

In November 2005, due to the appearance of switching technology with a capacity greater than a terabit per second (in this case the device being considered is the Terrascale E1200 by Force 10 Networks), it has become possible to send full precision data to the processor farm at the Level-0 acceptance rate of 1MHz [46]. This improvement eliminates the need for a separate Level-1 trigger and the associated buffering and subdivision of the processor farm.

The HLT will accept data at either the Level-1 40kHz or Level-0 1MHz rates depending on the decision[2] taken about the necessity of a Level-1 trigger. The HLT has access to full precision data from all the sub-detectors, although as the computationally-intensive RICH information has not yet been processed the initial algorithms do not use its information. The algorithms begin by reconstructing the primary vertex from the VELO information, and then link tracks to the T1-T3 tracking stations. The transverse momentum measurements are refined using the higher precision that is available, and interesting physics channels are selected. The events are stored at a rate of approximately 200Hz.

[2]In fact it has now been decided to combine the functionality of the Level-1 trigger with the HLT into the processor farm, which will accept the 1MHz input corresponding to the Level-0 acceptance rate.

Chapter 3

The RICH System

The primary task of the Ring Imaging Cherenkov (RICH) system is Particle Identification (PID). This is the determination of the particle species associated with a track from an interaction. Specifically the RICH system is designed to identify pions, kaons and protons with momenta from $\sim$1 GeV/c up to and beyond 100 GeV/c.

3.1 Motivation for Hadron Identification

Hadron identification is vital to separate decay modes, important for the measurement of CP asymmetries, from background processes with identical topologies. Examples of these decays are:

- B^0_d & $\overline{B}^0_d \to \pi^+ \pi^-$ [29]. This decay allows a measurement of CP asymmetry, related to the CKM angle α. It has several topologically similar backgrounds: $B^0_d \to K^+ \pi^-$, $B^0_s \to K^- \pi^+$, etc. The two-body invariant mass distribution from a PYTHIA simulation of similar decays is shown in Figure 3.1. It is clear that without the ability to distinguish π and K the $B^0_d \to \pi^+ \pi^-$ channel is swamped by its backgrounds, many of which are themselves CP violating, and the measurement becomes impossible.
- $B_s \to D^+_s K^-$ or $D^-_s K^+$ [49] provides a measurement of the CKM angle γ. The separation from $B_s \to D_s \pi$ is critical to remove the dilution from this

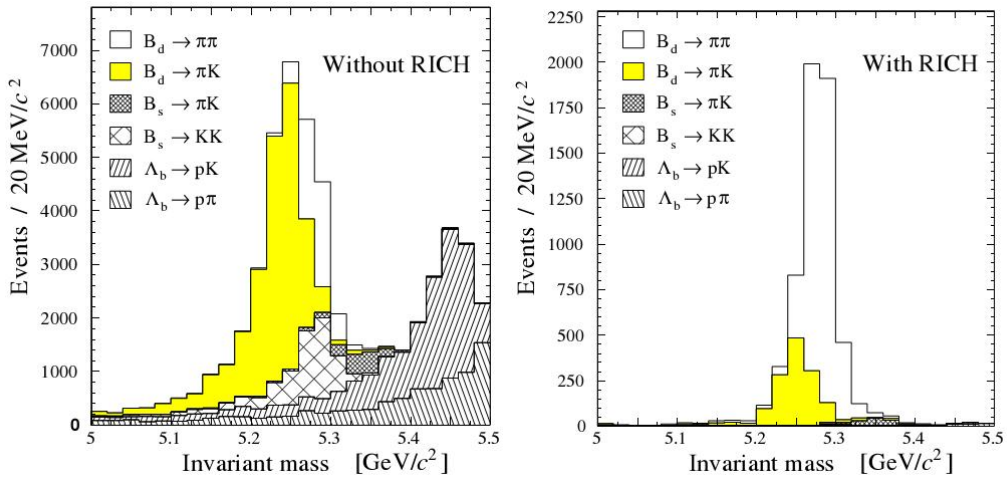

Figure 3.1: $B_d \to \pi^+\pi^-$ and background event separation, without (left) and with (right) the PID provided by the RICH detectors.

(fifteen times) more abundant decay channel. Again a PYTHIA simulation demonstrates the difficulty of separation without the π/K power of the RICH detectors. This is illustrated in Figure 3.2.

- $B^0 \to D^0\ K^{*0} \to \pi^-\ K^+\ K^+\ \pi^-$ and $B^0 \to \overline{D}^0\ K^{*0} \to \pi^-\ K^+\ K^+\ \pi^-$ [50] is a rare decay that provides an independent way of measuring the CP angle γ. In this case it is vital to identify which daughter particles were produced by the decay of the B^0 mesons, and again without the RICH this would be impossible.

- Flavour Tagging[51] is a method of determining whether a B meson contained a b or $\bar{b}$ quark when it decayed, allowing effects associated with neutral B mixing to be measured. The favoured b-c-s decay chain causes a b present in the meson to decay to an s that can be seen as a K^-. So determining the flavour of the s (or $\bar{s}$) quark in the K makes it possible to determine the flavour of the original B meson. However, this requires the product kaon to be distinguished from any charged pions produced.

The ability of LHCb to separate π and K species is one of the significant advantages it has over ATLAS and CMS in exploring the physics of the b-hadron sector.

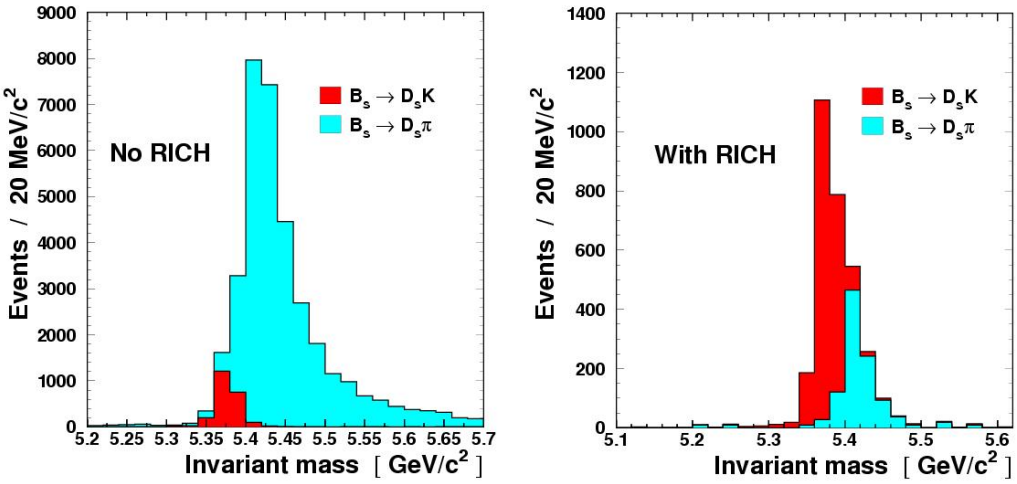

Figure 3.2: The separation between $B_s \to D_s\ K$ and the larger background $B_s \to D_s\ \pi$, without (left) and with (right) the PID provided by the RICH detectors.

3.2 Cherenkov Radiation

Cherenkov radiation is light emitted by particles travelling faster than the speed of light in the medium through which they are passing[52]. Historically its intensity has been used as an indicator of the activity of radioactive materials in nuclear facilities, where it is responsible for the distinctive blue glow in the water surrounding a nuclear reactor core. It is caused by a charged particle passing close to an atom in a radiator medium and polarizing it. As the atom relaxes it emits a photon. If the particle is travelling subluminally the photons are emitted in a de-coherent manner and destructive interference prevents them being radiated. If the particle is travelling superluminally the photons form a constructive wave front at a specific angle to the path of the particle, θ_c. This effect is shown in Figure 3.3, and results in a cone of light being emitted around the particle. The angle at which the light is emitted is calculated from the geometry of Figure 3.3 as

$$\cos\theta_c = \frac{1}{n\beta} \tag{3.1}$$

where θ_c is the angle of the light to the trajectory of the particle, n is the refractive index of the material and β is the particle velocity, expressed as a fraction of c. The photons are emitted uniformly in energy across the region of the electromagnetic

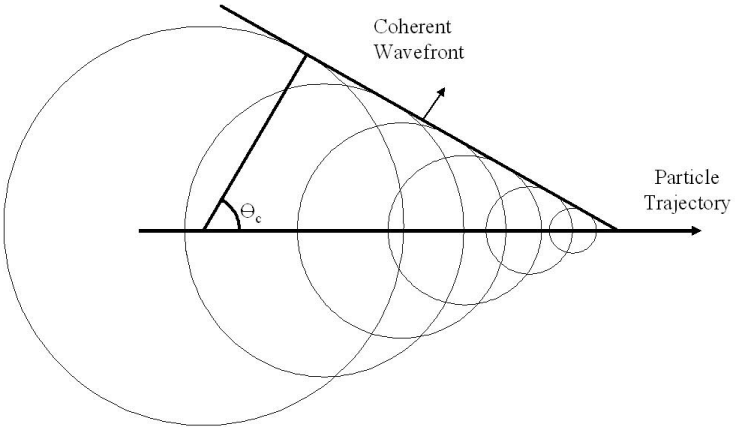

Figure 3.3: A Huygens construction showing how the light emitted by a particle travelling faster than the speed of light in the medium in which it is travelling results in a coherent front at a specific angle θ_c to the particle's trajectory.

spectrum where the radiator material is transparent and $n > 1$. Equation 3.1 makes evident a threshold particle velocity $\beta_{min} = 1/n$. The photon intensity is governed by the Frank-Tamm[53] relation.

$$\frac{dN}{dE} = \left(\frac{\alpha}{\hbar c}\right) Z^2 L \sin^2 \theta_c \tag{3.2}$$

Where dN is the number of photons generated by the particle, dE is the energy range $E \rightarrow E + \delta E$, Z is the particle's charge, L is the distance it travelled through the medium and α is the fine structure constant. Cherenkov radiation is a weak light source. For a singly charged particle, travelling at $\beta \approx 1$ 3.2 gives

$$\frac{dN}{dE} = 370 \left(1 - \frac{1}{n^2}\right) \text{cm}^{-1}\text{eV}^{-1} \tag{3.3}$$

By focussing this cone of photons to a ring with a spherical mirror, it is possible to determine θ_c and hence the velocity β of a particle by measuring the radius of the ring. It is this principle that drives the design of RICH detectors.

3.3 LHCb RICH Detectors

Diagrams of the RICH1 and RICH2 optical arrangements are shown in Figure 3.4. The two-mirror design is motivated by a requirement to keep the photon detectors

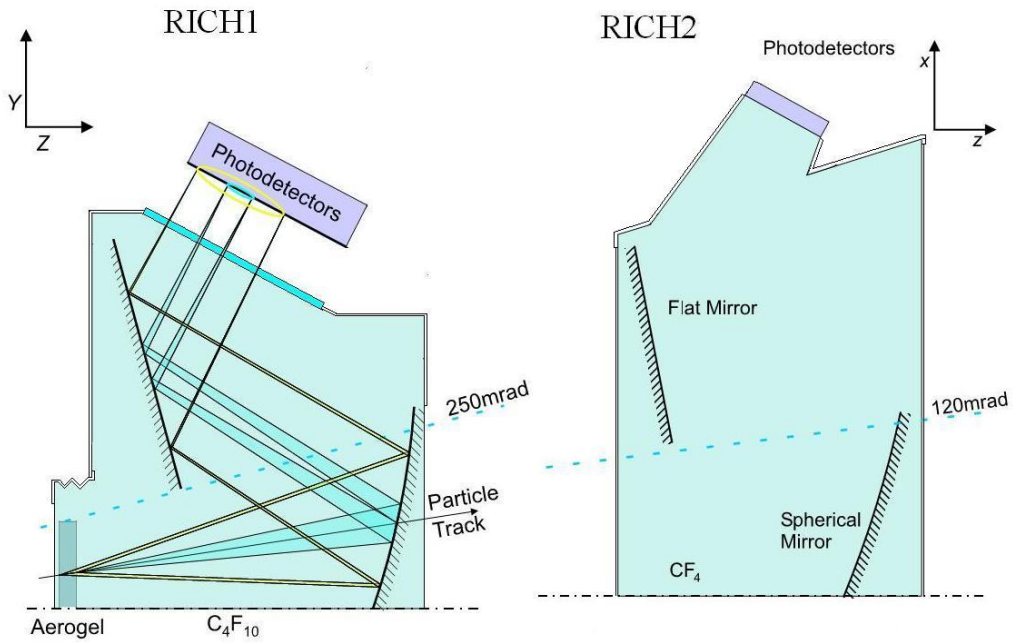

Figure 3.4: (Left) The upper half of the RICH1 optics in cross section, showing the flat and spherical mirrors, the aerogel and C_4F_{10} radiators, the quartz windows, the photon detector plane and the trajectory of Cherenkov light for a typical particle. (Right) The right half of the RICH2 optics in cross section, showing its smaller angular acceptance, radiator and mirror positioning.

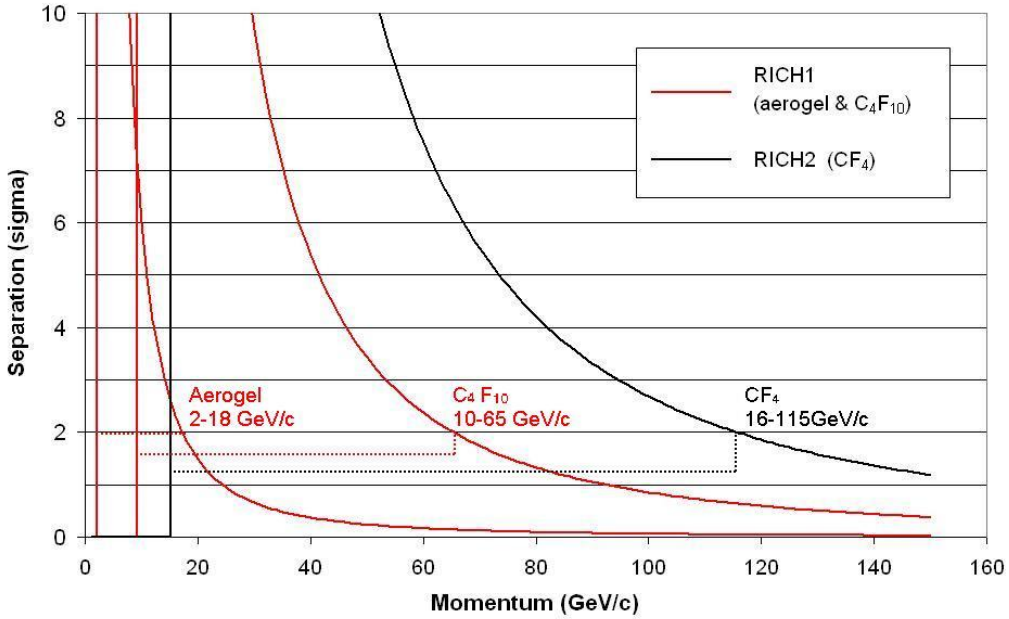

Figure 3.5: The π/K separation power of the three radiators, expressed in terms of the significance (sigma) of the Cherenkov angle difference as a function of particle momentum. The momentum coverage for a 2σ significance is indicated.

out of the LHCb acceptance and to minimize the overall z-dimension of the detector. Their design and performance are described in this section.

3.3.1 Radiators and Momentum Coverage

To separate hadrons over the wide momentum range that will be required by LHCb (1-150GeV/c)[33], three RICH radiators materials of specific refractive index are required. Figure 3.5 shows a calculation of the π/K separation performance of the silica aerogel, C_4F_{10} and CF_4 radiators chosen. The Cherenkov threshold and saturation limits can be seen for all three radiators. Figure 3.5 was produced by calculations based on equation 3.1 and values of uncertainty in angular measurement, refractive index and photon production given below in Section 3.3.2. The details of this calculation can be found in Appendix A.

The two radiators (aerogel and C_4F_{10}) designed to separate lower momentum par-

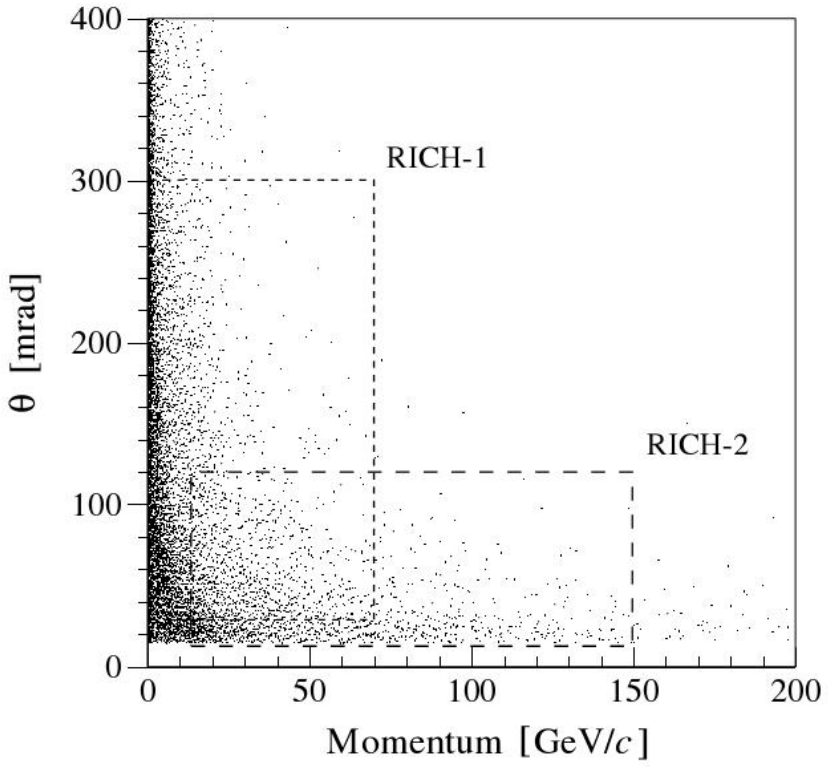

Figure 3.6: Scatter plot of polar angle vs momentum for all the tracks produced in a typical LHCb event. The acceptance of RICH1 and RICH2 are indicated, demonstrating the importance of the wide RICH1 acceptance and that the narrower angular acceptance of RICH2 is adequate.

ticles are housed in the RICH1 sub-detector. This detector is located upstream of the dipole magnet and is used to identify the lower momentum particles over the full angular acceptance. This includes those that would be swept out of the spectrometer acceptance by the magnet. Cherenkov rings from both radiators are focussed on the same photodetector plane by a common optical system. The CF_4 radiator will be located in RICH2, which has a smaller angular acceptance and is downstream of the magnet, as it is only needed to identify the higher-momentum tracks. The distribution of particle momenta across the LHCb acceptance and their division between the two RICH systems is shown in Figure 3.6.

In addition to possessing a suitable refractive index the radiators have to scatter the Cherenkov light as little as possible, requiring a high level of transparency. The two gas radiators comply easily, however the aerogel has to be in a thin section to prevent the relatively high Raleigh scattering in this medium from reducing the effectiveness of the ring pattern recognition software (see Section 3.4). There is also concern over aerogel ageing, as the variety being used is hygroscopic, and becomes opaque unless it is kept in a dry environment.

Recent developments in aerogel production[54], specifically aimed at developing a material for use in RICH detectors, have led to the production of tiles with exceptional clarity and good radiation tolerance. Tests in a charged particle beam carried out at CERN by the LHCb group[55] have confirmed the material will perform well as part of the LHCb RICH system.

3.3.2 Precision of Cherenkov Angle Measurement

There are four main contributions to the uncertainty of the Cherenkov angle measured by the RICH detectors.

- **Emission Point Error:** To locate the photodetector planes outside the acceptance of the experiment, the spherical focussing mirrors have to be tilted. This leads to the reconstruction of the Cherenkov angle being dependent on the position where the Cherenkov photon was emitted along the particle's track. As it is not possible to determine this position, the midpoint of the track through the radiator is selected for the calculation, leading to an uncer-

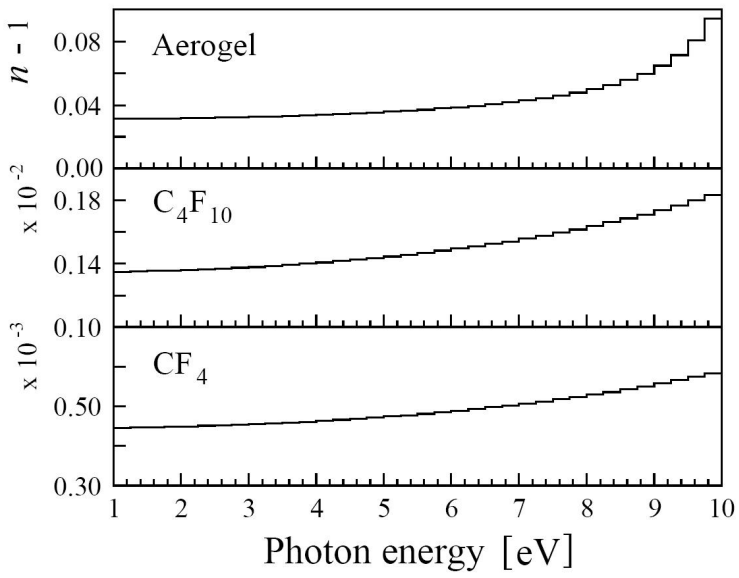

Figure 3.7: The variation in refractive index against photon energy for each of the three RICH radiators. This is the cause of the chromatic dispersion uncertainty.

tainty. The contribution from this uncertainty is dependent on the length of the radiator and cannot be reduced without causing an unacceptably high loss of Cherenkov photons.

- **Pixel Size:** The effect of the granularity (pixel size) of the photon detector on the resolution of the measurement of the Cherenkov angle is a limiting factor on the optics of the system. This is set by the photon detector technology being used. The differing optical paths from the three radiators mean that a pixel size set by a common photo-detector design will subtend a varying angle and contribute differently to the uncertainty for each RICH radiator system.

- **Chromatic Dispersion:** The dependence of the radiators' refractive index on the energy of the photon (shown in Figure 3.7) results in an uncertainty on the Cherenkov angle. This is due to the photons being generated with a distribution of unknown energies, causing the refractive index that determines θ_c to be uncertain.

- **Track Error:** The tracking systems have a finite resolution, leading to an uncertainty in the trajectory of the particle within the RICH radiator volumes. This leads to an uncertainty in the reconstruction of the track and the Cherenkov angle that links it to a ring on a photodetector plane.

Radiator		Aerogel	C_4F_{10}	CF_4
Location		RICH1	RICH1	RICH2
Refractive Index		1.03	1.0014	1.0005
Length	(mm)	40	850	1900
$p_{thresh}(\pi)$	(GeV)	0.6	2.6	4.4
$p_{thresh}(K)$	(GeV)	2.0	9.3	15.6
$\sigma_{emission}$	(mrad)	0.29	0.69	0.31
σ_{pixel}	(mrad)	0.62	0.62	0.18
$\sigma_{chromatic}$	(mrad)	1.61	0.81	0.42
σ_{track}	(mrad)	0.52	0.40	0.20
σ_θ	(mrad)	1.9	1.3	0.7
N_γ		6.8	30.3	23.2

Table 3.1: The parameters for the three radiators and the values of the four major sources of uncertainty for each.[45]

The first three contributions above yield uncertainties on the Cherenkov angle from a single photon. They are independent for all photons produced by a given particle. The contributions thus scale as $\frac{1}{\sqrt{N}}$ where N is the number of photons produced. The track error is however common to all photons and is not reduced by a large N, so needs to be small in comparison to the other three contributions.

A summary of the values associated with these major sources of error is given in Table 3.1. The N_γ value given is for the final photon detector choice and is the number of photons expected to be detected, rather then the number emitted by the radiator. The pattern recognition and angle reconstruction algorithm are described in the following section.

3.4 Pattern Recognition and RICH PID Performance

In the RICH system, particle identity is determined by matching tracks (produced by the VELO and TT) to rings on the photodetector planes and determining the most probable candidate particle for each track/ring. This method is combined with information from the calorimeters and the muon systems to further enhance the PID efficiency of LHCb.

The RICH pattern recognition[56] software uses a global maximum likelihood method to fit the association of all measured photon hits with all measured charged particle tracks. The association is made in the θ_c, ϕ_c space of the Cherenkov angles, calculated for each hit-track association. The advantage of this global method is that the main background originates from Cherenkov rings associated with neighbouring tracks and this is correctly accounted for in the likelihood function.

To identify the particle that produced a track a likelihood is calculated, based on the Cherenkov angle of the hits. If this is carried out for the six available particle hypotheses (pion, kaon, muon, electron, proton and beyond threshold), for all the tracks in an event, the computation time is excessive. Instead, as the majority of particles passing through the RICH system are pions, a fit is made assuming all the particles are pions and then, track by track, the various hypotheses are tested, maximising the likelihood on a track by track basis. The photodetector planes of a typical event with the fitted rings and hits marked are shown in Figure 3.8.

The performance of the RICH PID is measured by efficiency, defined as the fraction of particles of a given type that are identified correctly. Figure 3.9 shows the Kaon efficiency and the pion misidentification rate over the momentum range. If the occupancy of the photoplanes rises above $\sim$1% then the efficiency of the pattern recognition is reduced.

3.5 Photon Detectors

The Cherenkov rings are projected onto planes of photon detectors, made up of an array of pixelated photo-tubes. These instrument a total area of about $3m^2$ with pixels of order $2x2mm^2$ and with an active to total area ratio of approximately 70%. There are strict requirements on the performance of these sensors. These include:

- Single photon sensitivity: The small number of photons emitted by each particle travelling through the various radiators means that a sensitivity to individual photon hits is an absolute requirement.
- Very high signal to noise ratio: The performance of the ring-finding algorithms is degraded by random noise in the system, so minimizing this is important.

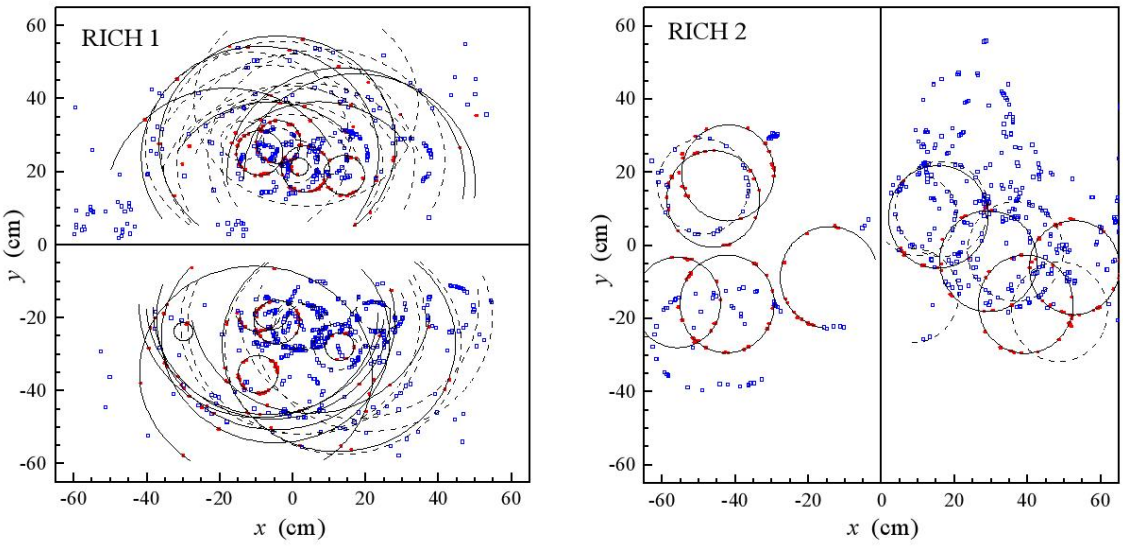

Figure 3.8: The hits and fitted rings for a typical event in RICH1 and RICH2. The small (large) ring radii in RICH1 originate from the C_4F_{10} (aerogel) radiator. The solid rings indicate tracks passing through the whole detector and the dotted rings indicate other tracks.

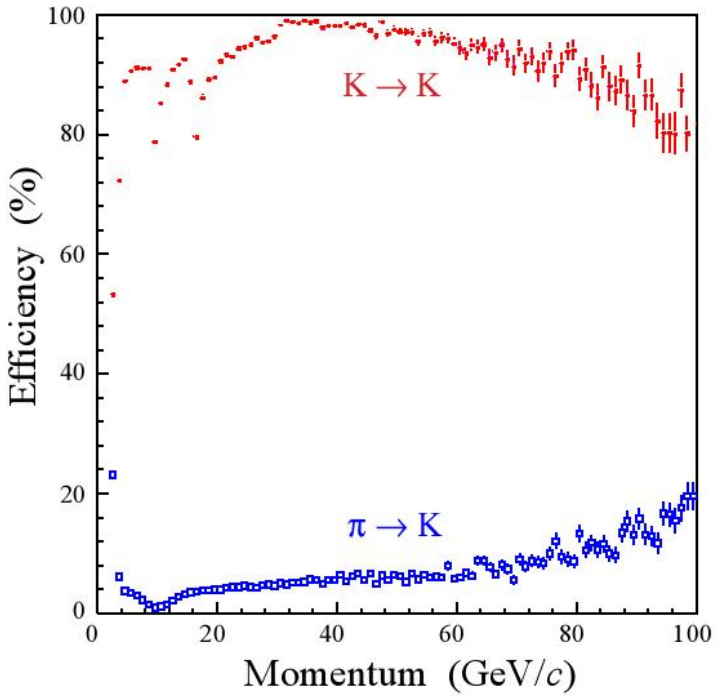

Figure 3.9: The kaon identification efficiency and pion misidentification rate over the 0-100GeV/c momentum range. The dips in the K efficiency occur at the K threshold in the different radiators[35].

- A high quantum efficiency: Again, the small number of Cherenkov photons means that any improvement in the quantum efficiency of the detectors improves the ability of the RICH system to make a good measurement of the Cherenkov angle of a given particle.

- Radiation tolerance: Whilst the photo-tubes are housed some way from the beamline, they will still experience a radiation dose of approximately 3kRad per year. It is important that the system can withstand this and continue to operate within specifications for the ten year proposed lifetime of the experiment.

- 40MHz readout rate: To match the LHC bunch crossing rate the photon detectors have to be read out every 25ns.

- Broad spectral range: Cherenkov light is emitted across a broad spectrum. The tubes have to be sensitive to as wide a band as possible (within the limits of the other optical components) to maximise the number of photons collected for each ring, to aid the pattern recognition and to enhance the accuracy of the measurement.

- Insensitivity to magnetic fields: The photo-tubes have to operate in the fringe fields of the LHCb dipole magnet. Whilst shielding will be installed, it can only attenuate, not eliminate, the field the tube experiences. This issue is examined in more detail in Chapter 4.

After the "lite" redesign, two photon detector technologies remained under consideration for use in the RICH detectors. The Hammamatsu Multi Anode Photo Multiplier Tube (MAPMT)[57] and the CERN-designed Pixel Hybrid Photon Detector (HPD)[58]. There is no critical difference in the performance of the two detectors in terms of photon yield, Cherenkov angle precision and particle identification performance. However, there are slight variations in these indicators between the two technologies and more significant differences in cost, magnetic performance and availability[59].

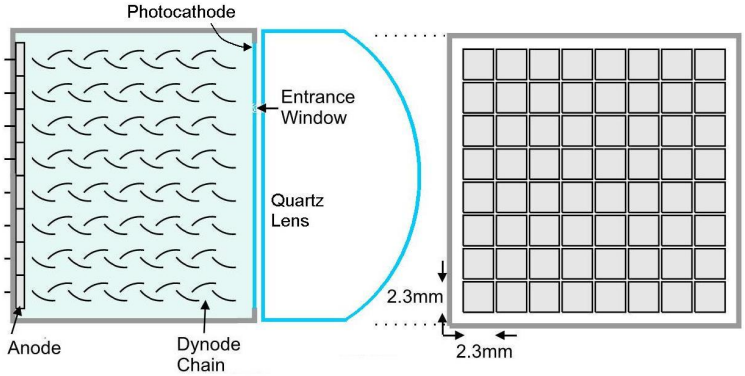

Figure 3.10: (*left) A conceptual diagram of a reduced MAPMT dynode chain.* (right) The corresponding pixel arrangement mapped onto the front of the tube.

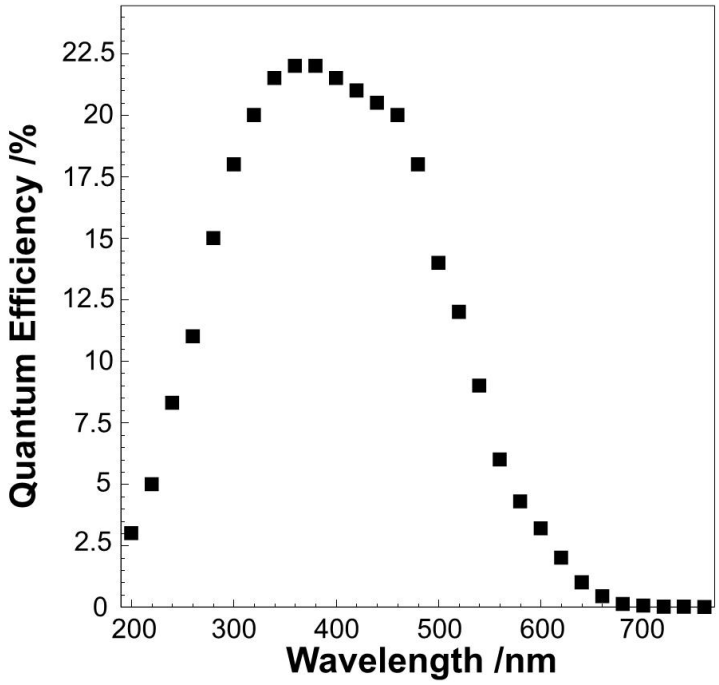

Figure 3.11: The quantum efficiency of the MAPMT photocathode window as a function of the wavelength of the incident photon[57].

3.5.1 The Hammamatsu Multi-Anode PhotoMultiplier Tube

The Hammamatsu R7600-03-M64 64 channel MAPMT operates in a similar manner to a standard single-anode photomultiplier. A photon falling on the UV-glass entrance window hits the bialkali photo cathode deposited on the inside. The photoelectron produced is accelerated onto the first dynode of one of the 64 independent dynode chains. This causes a cascade down the dynode chain in the same way as a standard photomultiplier, leading to a measurable signal on the anode. The principle is illustrated in Figure 3.10.

The adoption of the MAPMT would have required a readout system to be designed. It was decided to use the University of Heidelberg 'Beetle' chip[60], developed for the silicon detectors of the VELO, TT and IT front end readout systems. As the signals produced by the 12 dynode MAPMT are much larger than the 25,000 e^- expected by the pre-amplifier of the Beetle chip, a variant 8 dynode MAPMT was considered with a much smaller gain. Variations of the Beetle chip with lower pre-amplifier gain were also designed and tested.

The advantages of using the MAPMT were as follows. Firstly, as a commercial product, little development work was required. In fact, the development is limited to the adaption of the Beetle chip to the larger front end signals. The MAPMT also has a better tolerance to magnetic fields than the HPD. The unshielded MAPMT is able to withstand fields up to 20G longitudinally before its efficiency drops below 90% [61]. In addition there is no field level at which it suddenly stops operating; its performance degrades slowly in increasing fields as more electrons miss the dynodes in the cascade. The fractional area coverage of the initial stage dynodes of the close-packed array of MAPMTs is only 37%. By using hemispherical quartz lenses, and sacrificing a further 8% of photons to the two additional quartz-air interfaces that are introduced, it is possible to increase this to 78%. This figure drops to 72% when magnetic shielding is added increasing the spacing between tubes, but is still higher than the 67% achieved with the hexagonal close-packed cylindrical HPDs.

The MAPMT has several disadvantages compared to the HPD. The quantum efficiency of its photo cathode (shown in Figure 3.11) with an energy-integrated value of 0.6eV is at least 20% lower than the associated value for the HPD photo cathode. The cost of instrumenting the photo-plane with MAPMTs is 1 million CHF

higher than for HPDs, before including the development and production of the additional MAPMT electronics. Tests in a charged particle beam carried out in 2003[62] with nine close-packed MAPMTs discovered significant problems with the prototype readout electronics. These included channel-to-channel cross talk, undershoot and spillover effects, resulting from the coupling of the Beetle chip to the pin-out of the MAPMT.

The MAPMT/Beetle system could be read out either in analogue or digital modes. The infrastructure to support reading the Beetle in analogue mode was deemed to be prohibitively expensive. The two options were to either provide radiation tolerant analogue digital converters close to the RICH or run the analogue signals 100m to the counting room. The digital mode of the Beetle chip incorporates a 3-bit threshold, however this requires that the gain of the system is carefully controlled. In addition the digital mode leads to an unavoidable loss of efficiency, due to the threshold cut on the wide single photoelectron pulse shape of the MAPMT anode signal. In the beam tests carried out on this device it was not possible to obtain an efficiency better than 80% on single photoelectron signals and to achieve this figure the gain and high voltage required careful tuning[62].

3.5.2 The Pixel Hybrid Photon Detector

The pixel HPD[58] was developed by Thierry Gys et.al. at CERN in collaboration with DEP[1]. Figure 3.12 shows a completed tube and the principles of its operation. The front of the tube is enclosed in a spherical quartz window 83mm in diameter and 7mm thick. The window has an S20 multialkali photocathode coating deposited onto its inner surface. The photocathode is held at -20kV and photoelectrons are accelerated in the electrostatic field. Two further electrodes at -19.7kV and -15.8kV cross-focus the photoelectrons onto a pixelated silicon sensor with a demagnification factor from cathode to sensor of approximately 5.4. The sensor is directly bonded to the tube's internal readout electronics. This readout chip converts the charge deposited in the silicon sensor into a 40MHz binary signal, synchronised to the LHC bunch crossings. This allowed the HPD to be read directly by the external electronics chain. Details of this encapsulated readout chip are presented in Section 5.1.

[1]Delft Electronic Products, Netherlands

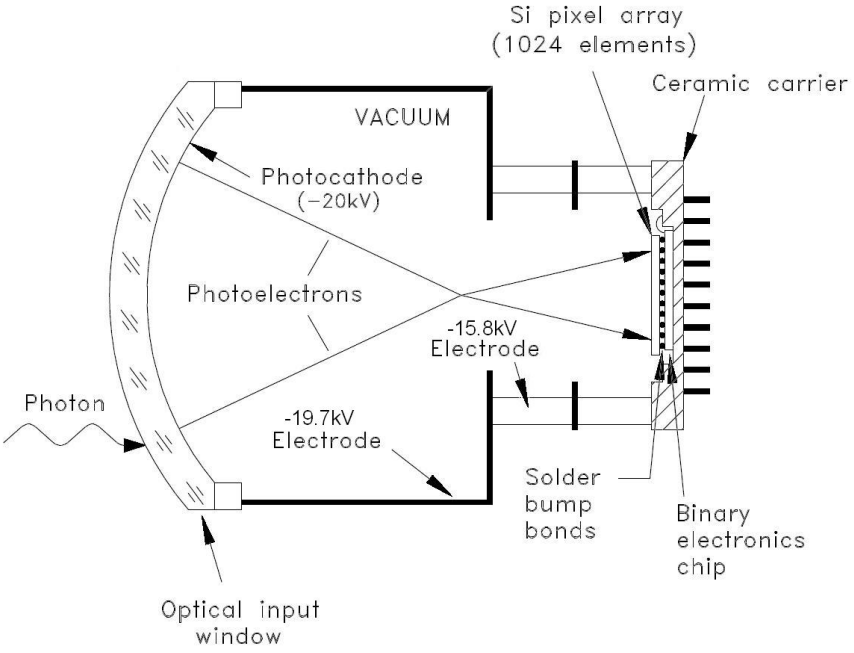

Figure 3.12: (Top) A schematic diagram showing the components of the HPD and the path of a photon $\rightarrow e^- \rightarrow$ sensor. (Bottom) A photograph of a completed HPD.

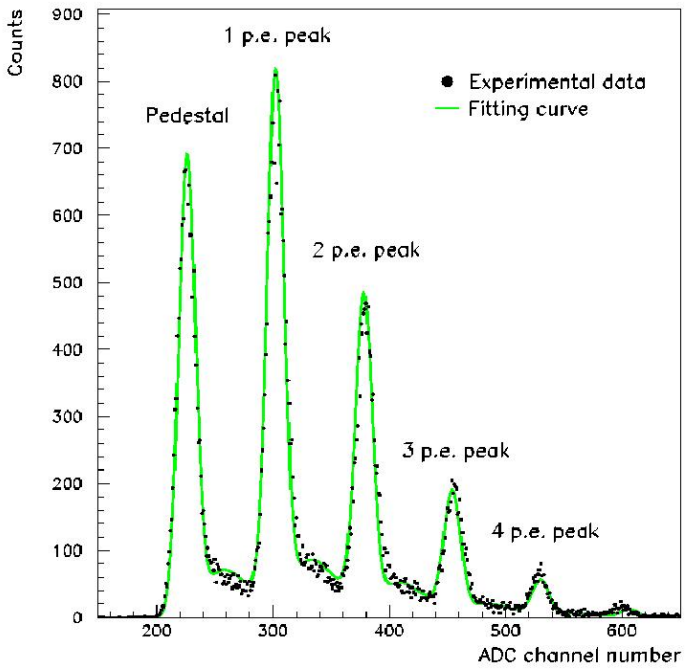

Figure 3.13: The response of the HPD sensor assembly to multiple photoelectron hits. The clear distinction between the single photoelectron and the pedestal is shown[58]. This plot is for an early prototype of the HPD where the analogue response was available, in the final tubes the separation between the pedestal and the 1 p.e. peak has been increased further to give a signal to noise ratio of order 50.

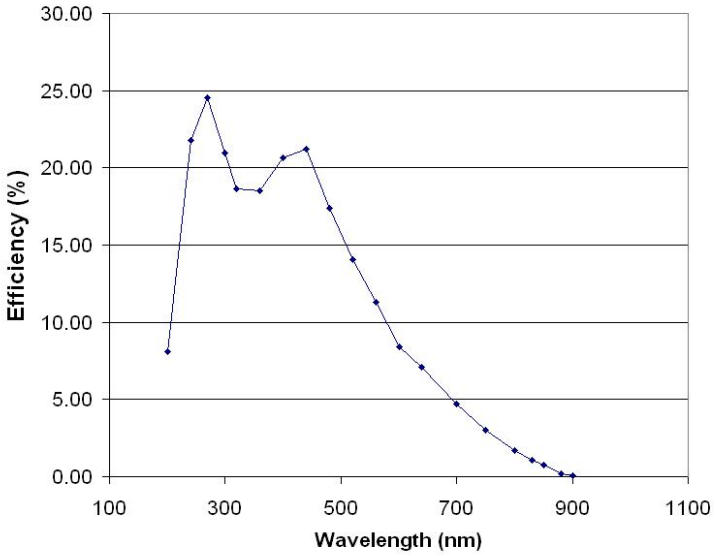

Figure 3.14: The typical quantum efficiency of the HPD's S20 photocathode as a function of the wavelength of the incident photon[35].

The useable photocathode covers a circular area of the HPD window 75mm in diameter, giving an active fraction of 0.82 of the HPD's frontal area. With the tubes arranged in a hexagonal close-packed structure, with 2mm tubular magnetic shielding around each HPD, the coverage of the photo-plane is reduced to 67%.

The HPD has several advantages compared to the MAPMT. Primarily it has an extremely good signal to noise ratio, due to the unique way in which it uses a silicon sensor and electrostatic field to provide its amplification and detection. A photoelectron accelerated through 20kV in the HPD will deposit approximately $5000e^-$ in the silicon pixel detector, providing excellent photoelectron counting performance as shown in Figure 3.13. This amplification, coupled with the proximity of the read out electronics, means that the signal to noise ratio of the HPD is of order 50. The photocathode has a very high quantum efficiency (shown in Figure 3.14), with an energy integrated value of 0.77eV. The LHCbPIX1[63] read-out chip has been demonstrated to withstand a radiation dose of 30MRad. This is three orders of magnitude larger than the expected integrated 30kRad in the final HPD location. The on-board digitisation and binary readout provided by the LHCbPIX1 chip significantly reduce the required data transfer and processing that would otherwise have to be carried out by the Level-0 board.

The drawbacks of the HPD as the RICH photon detector are its sensitivity to magnetic fields and the more severe requirement to electrically insulate the tubes (20kV for the HPD vs 1kV for the MAPMT) when they are arranged in a close-packed array. The sensitivity of the HPD to magnetic fields is discussed in more depth in the next chapter; but briefly it requires significant shielding to allow it to operate in the fringe field of the LHCb dipole magnet. In addition the -20kV potential on the photocathode means it is critical that the tubes are isolated from each other. This allows individual tubes in the array to be returned to ground if they fail, without having to disable the entire photo plane. This is achieved by coating the inside of the magnetic shielding tubes with a layer of kapton[64]. The insulation scheme also isolates the HPDs from their tubular magnetic shields, reducing the probability of micro-discharges causing noise hits, and any larger scale discharges causing damage to the tubes. At the time of writing, a recent system test of a close packed array of HPDs had been completed successfully at the Frascati National Laboratory beam test facility. Preliminary results[65] from this indicate that the level of this noise is well within the limits of 1% occupancy, beyond which the performance of the particle ID pattern recognition program will decrease.

The HPD development and manufacture has involved several companies external to CERN. The HPD is assembled at DEP from a quartz window, on which the photo cathode is deposited, a ceramic envelope and an anode assembly packaged in a Pin Grid Array (PGA) carrier. To ensure the high quality vacuum necessary in the tube, the components have to be baked out at 300^{o}C before the quartz window is sealed to prevent out gassing in the future. The anode assembly is produced at VTT[2] where the pixel sensor is attached to the readout chip by a "bump bonding" process. This entails an array of solder bumps (hemispheres of approximately 12μm radius) being deposited using a photo-lithographic photo resist mask that is then etched away. The two chips with the solder bumps are aligned and heated until the bumps melt together to form an array of joints. Once the anode assembly has been manufactured it is wire-bonded and packaged to a gold plated carrier with a PGA similar to a 'Pentium' class microprocessor. This carrier is then sealed into the base of the phototube before it is baked out prior to the window being sealed.

[2]VTT Technical Research Centre of Finland

3.5.3 Choice of Photon Detector

Throughout the majority of the development of the RICH systems the MAPMT was held as a backup option that, in the event of the HPD development failing to produce a phototube, could be manufactured in time to meet the installation schedule. This changed in 2002 when significant problems were encountered in the development of the bump bonding procedure required to attach the HPD's sensor to the read-out chip. The number of pixels that were insensitive or noisy after the tube had been fully assembled was unacceptably high, a problem caused by the bump bonds melting during the tube's vacuum bake-out cycle. Although this problem was later solved by the introduction of a new high lead content solder, important milestones in the development schedule had been missed. The decision was taken in 2003 to switch to the MAPMT as the first choice detector, whilst development of the HPD was continued. This led to significant work being carried out to produce a front end readout system for the MAPMT. The readout problems encountered by the MAPMT systems, its lower signal to noise ratio, the higher cost coupled with the solution of many of the production problems of the HPD project, led to the decision being taken to return to the HPD as the RICH photon detector. The current (June 2006) status is that 50% of the required HPDs have been delivered and tests indicate a very high yield of tubes with good quantum efficiency and greater than 99% of pixels operational.

3.5.4 RICH Readout Electronics Chain

The HPD readout electronics on the detector, the Level-0 adapter board, is required to create signals to provide the HPD clock and trigger event readout (at a maximum of 1MHz) and to multiplex the data read from the HPDs onto an optical link. The Level-1 readout boards in the counting room are required to accept these data, apply further zero suppression and pass them onto the HLT processor farm over gigabit ethernet links.

The RICH readout electronics chain is shown in Figure 3.15 and supported on a ladder frame[66] that carries the HPD tubes in a column (16 HPDs in RICH2 and 14 HPDs in RICH1). The HPD is connected to a Zero Insertion Force (ZIF) socket on a board in the HPD support mechanics and connected to the Level-0 board by

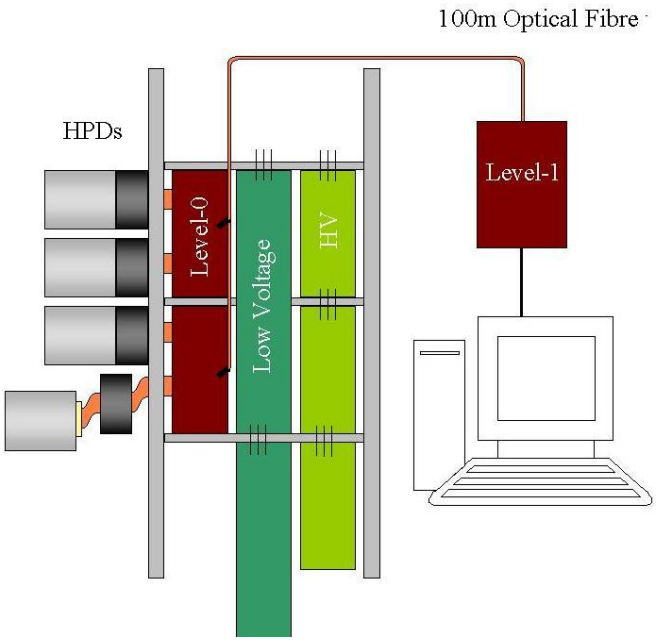

Figure 3.15: A diagram showing the components of the HPD readout electronics chain mounted on the column, the flexible coupling, the Level-0, Low Voltage, High Voltage(HV) and Level-1 boards that connect the HPD to the online computing farm in the counting room.

flat, flexible, kapton printed circuit cables. The Level-0 board[67] multiplexes the signals onto 1.6Gbs^{-1} optical fibres and sends them to the Level-1 board in the counting room. The RICH Level-1 board[68] takes the optical link and feeds the data into the computing farm over multiple gigabit ethernet links. The power for the readout chip and Level-0 boards is supplied by the Low Voltage (LV) boards. The power for the photocathode potential and the focussing electrodes in the HPD is provided by the High Voltage board (HV).

3.6 RICH1 Mechanics

The design of the magnetic shielding for the RICH1[69] detector is described in Chapter 4. The shielding is constrained by the requirements of the overall RICH1 mechanical and optical layout. It is therefore pertinent that these are described here in some detail.

The location of RICH1, upstream of the dipole magnet, allows for a larger angular acceptance than that of RICH2. This means its dimensions are not on the same scale as its larger sibling. However, the proximity of the cavern walls to the sub-detector, and the limited space along the beamline, significantly reduces the amount of space available, presenting many design challenges. The RICH1 spherical mirrors are tilted about a horizontal split, with the flat mirrors and HPD mountings above and below the beampipe. The layout of the sub-detector is shown in Figure 3.16. The mirrors, flat and spherical, are mounted on frames; these are in turn mounted within the C_4F_{10} gas enclosure. This is clamped to the lower magnetic shield. On the top and bottom of the gas enclosure are quartz windows to allow the photons to pass from the C_4F_{10} environment into the dry N_2 environment enclosing the HPDs. A small photosensitive area is shadowed by the necessity to manufacture the windows in two pieces and have a joining strip. The quartz windows are coated with an antireflective coating to reduce losses at the quartz-gas interface.

The upstream face of the gas enclosure has a circular aperture to allow a cylindrical, flexible bellows to connect the gas enclosure to the exit window on the VELO. This arrangement avoids the requirement of placing an entrance window within the LHCb acceptance, thus reducing the material budget of RICH1. The aerogel tiles, mounted in a carbon-fibre box with a thin glass downstream window to prevent

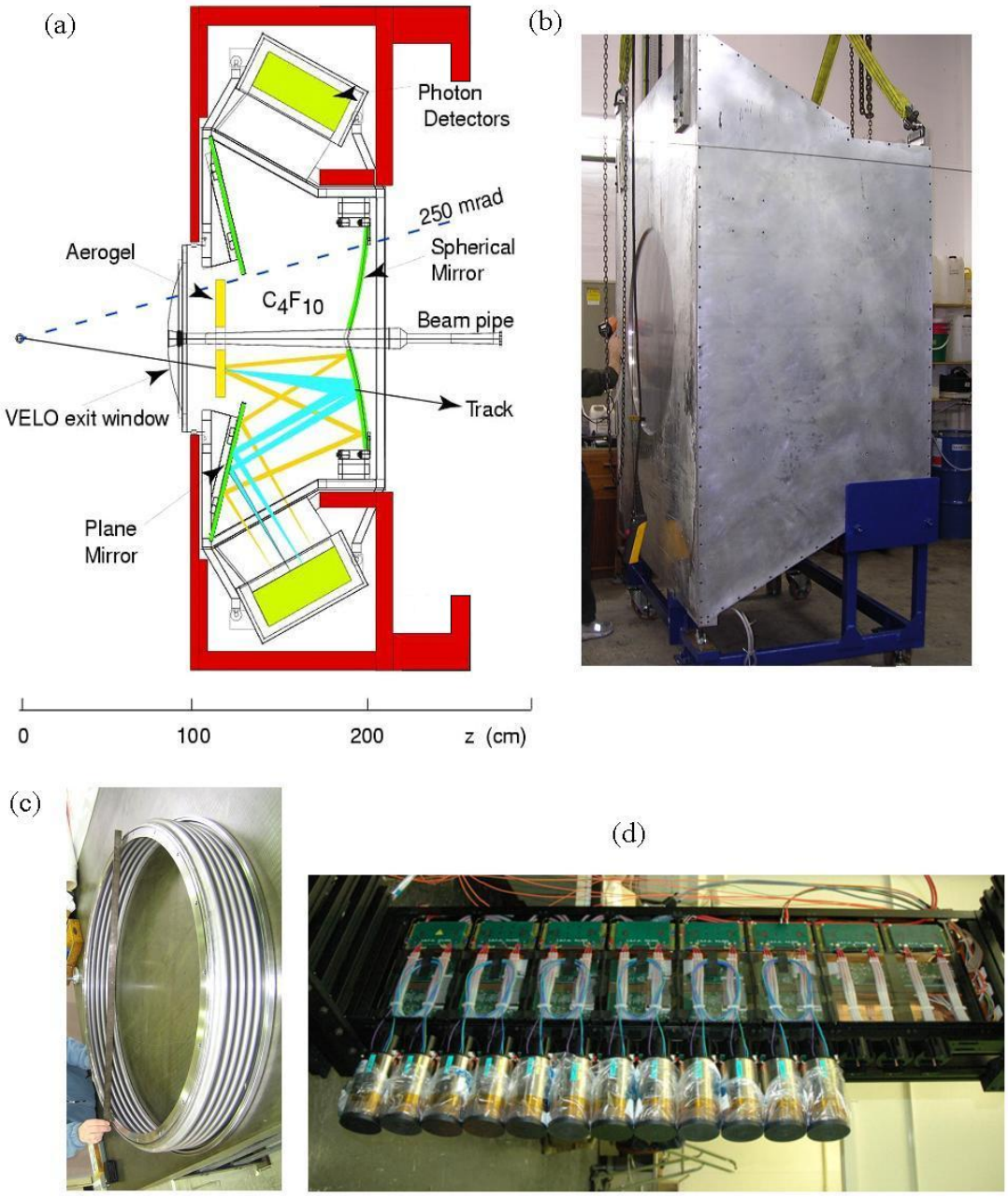

Figure 3.16: (a)A cross section of the design of RICH1, showing the optical path, mirrors, mirror supports, the beampipe, the VELO exit window, gas enclosure, HPD enclosures, radiators and magnetic shielding. (b) A photograph of the completed gas enclosure with the side plates on and a cover over the VELO window aperture. (c) The flexible bellows that will seal RICH1 to the VELO. (d) A partially populated RICH2 column of HPDs and electronics.

them coming into contact with water vapour, will be mounted within this circular aperture. The downstream face of the gas enclosure will comprise a low-radiation-length exit window sealed around the beampipe. It is a composite design, comprising two carbon fibre skins covering a core of polymethacrylimide(PMI) foam. This is sealed to the beampipe by a rubber diaphragm, designed to isolate mechanically the delicate beryllium beampipe from any movement of the exit window due to vibrations or a pressure difference across the window.

The sides of the gas enclosure are removable to allow the optical components to be installed. The gas enclosure itself is made from machined aluminium alloy plates welded together. It is clamped to the lower magnetic shield by a three point mounting system that accommodates differential thermal expansion and allows it to be accurately positioned and then locked in place.

The HPDs and their electronics will be mounted on seven columns of fourteen HPDs, in turn mounted in boxes that are held on rails above and below the gas enclosure. The top box is mounted from the upper magnetic shield; the positioning rail is mounted on the upstream wall of the shield to reduce the probability of movement. The lower box is mounted on the base of the lower shield using a similar rail system. Rails have been used as it is foreseen that it will be necessary to remove the HPD boxes reasonably frequently for access to replace tubes or repair electronics. The boxes will be connected to the frames of the quartz windows by a retractable flexible seal that will enclose the HPD N_2 atmosphere.

The RICH1 spherical mirrors are in the path of charged particles and high energy photons resulting from the proton-proton collisions. They are therefore required to contribute a small fraction of a radiation length (specified at $<2\%$), whilst spanning an area of 1.6m by 1.2m. In addition, the mirrors must have an excellent reflectivity across the band visible to the HPDs, be tolerant of the C_4F_{10} environment and be structurally stiff to avoid any deformation. The original technology proposed to meet these requirements was an eight section beryllium substrate design, that could be made as thin as 3mm. However supply problems have led to the adoption of a carbon composite solution provided by CMA[3]. The RICH1 plane mirrors are outside the LHCb acceptance and their material budget is not critical. They are therefore made from a glass substrate (borosilicate) with a deposited aluminium coating. These

[3]Composite Mirror Applications, Inc. USA

Component	X_0	λ_1
Aerogel	0.033	0.007
C_4F_{10}	0.026	0.016
Spherical Mirror	0.011	0.005
Exit Window	0.006	0.003
Total	0.076	0.031

Table 3.2: The material budget for RICH1, expressed as a fraction of a radiation (nuclear interaction) length $X_0(\lambda_1)$.[45]

plane mirrors allow the HPDs and associated electronics to be located outside the RICH1 acceptance, and in a region where iron magnetic shielding can be assembled to attenuate the field of the dipole magnet. The upper and lower plane mirror panels 1500mm by 775mm will each consist of eight segments. The individual mirrors will be aligned and then locked prior to installation. A laser alignment monitoring system will be used to verify the alignment and stability of the mirror segments. A laser transmitted down an optical fibre is split into a reference and objective beam. The reference beam is pointed directly at a CCD and the objective reflected from the mirror segments. Any changes in the relative position of the two spots on the CCD indicates a rotation in the mirrors.

As the design described above indicates, the material budget for items within the LHCb acceptance is extremely limiting. All of the components have been selected to have the minimum chance of causing scattering. This is due to the RICH1 location far upstream of the main LHCb sub-detectors and any scattering of charged particles or photon conversions will make the event more difficult to reconstruct. Additional tracks in the tracking stations, additional rings in RICH2 and degraded ECAL performance are all likely consequences of exceeding the RICH1 material budget. The radiation lengths for the components RICH1 in the acceptance are shown in Table 3.2.

The 25mrad section of beampipe passing through RICH1 is constructed from beryllium to minimise the chance of particles scattering and photons converting from it. It connects to the VELO exit window upstream and is sealed to the RICH1 exit window by a flexible diaphragm at its downstream end. Periodically the beampipe has to be baked out to maintain the quality of the LHC primary vacuum; to do this a heating jacket must be fitted around it, requiring the removal of the optical components in RICH1.

3.7 RICH2 Mechanics

The RICH2[70] CF_4 radiator volume covers a reduced acceptance angle of ±120mrad in x and ±100 mrad in y, optimised for high momentum tracks. It is shown in Figure 3.17. Its superstructure, made from welded aluminium box section girders weighing in excess of 6000kg, supports and locates the following components whilst remaining outside the 300mrad LHCb acceptance.

- **Spherical Mirrors:** The two RICH2 spherical mirrors each comprise arrays of 21 hexagonal and seven half-hexagonal segments. The mirrors cover an area of approximately 3m by 2.4m. The mirrors are made from aluminium deposited on a 6mm thick glass substrate and have a roughness of better than 3nm. Including the effect of gaps between the segments to allow for adjustment, the reflectivity of the surface reaches 96.2% and is above 90% between 230-600nm.

- **Flat Mirrors:** The flat mirror arrays each comprise 20 rectangular 410mm by 380mm segments. These plane mirrors are designed to extend the photon path and the HPD plane beyond the 300mrad LHCb acceptance.

- **HPD Assemblies:** Each of the RICH2 HPD planes and their associated electronics are mounted on 9 vertical columns of 16 HPDs. These follow the close-packed arrangement discussed earlier, with each tube being surrounded by its own individual 0.76mm-thick mumetal shield. The columns will be mounted on rails to allow easy withdrawal and access to maintain the tubes and their electronics.

- **Quartz Windows to HPD Enclosure:** The HPD quartz windows will each comprise three pieces of 6mm thick quartz, sealed together with a stainless steel 'I' beam with the joint at 30° to minimise photon loss. They have an antireflective coating to minimise reflection loss.

- **HPD Magnetic Shields:** To further shield the HPDs from the effects of the magnet's fringe field—over 150G in this location—they are enclosed in iron housings. These shielding structures are constructed from 60mm thick iron plates and attenuate the field the HPDs see by more then a factor of 15. These shields are bolted to the RICH2 superstructure. Having these large iron boxes in such a high field region means the superstructure has to endure

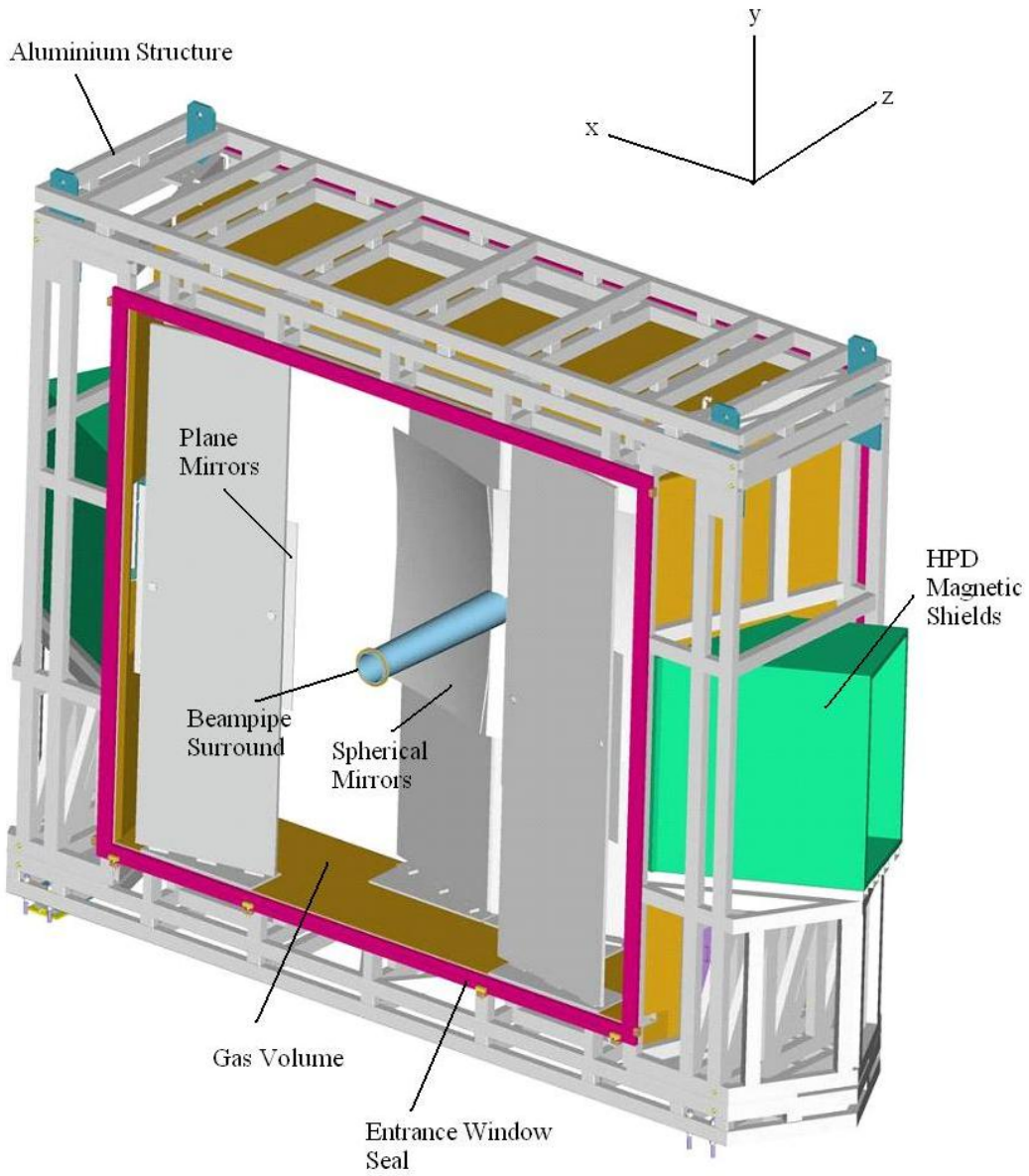

Figure 3.17: The design of the RICH2 mechanics. The superstructure is approximately 9m across (in x) and 7m high (in y).

Component	X_0	λ_1
Entrance Window	0.010	0.004
Exit Window	0.025	0.005
Spherical Mirrors	0.047	0.014
Panels	0.04	0.0095
Supports	0.005	0.002
Flat Mirrors	0.047	0.014
Panels	0.038	0.009
Supports	0.004	0.0015
Totals		
0 to 125 mrad	0.127	0.0345
125 to 300 mrad	0.124	0.0335

Table 3.3: The material budget for RICH2, expressed as a fraction of a radiation length X_0. The totals given are for horizontal angular divisions.

a magnetic force of over 5000N and yet is required to deflect less then 0.1mm to retain its optical stability.

- **Gas Enclosure Entrance and Exit Windows:** The entrance window is made from 1mm carbon fibre skins covering a 20mm PMI foam core. The exit window is made from 1mm aluminium skins and a 30mm foam core. They have to withstand a 400Pa overpressure of gas and will deflect slightly under it. Their lightweight design minimises the chance of photon conversion upstream of the calorimeters.

The radiation and interaction lengths for the components of RICH2 within the LHCb acceptance are shown in Table 3.3.

Chapter 4

RICH1 Magnetic Shield

The magnetic fringe field upstream of the dipole magnet affects two systems critical to the overall performance of the LHCb experiment. Too high a magnetic field in the HPDs (Hybrid Photon Detectors) in RICH1 degrades the performance of the RICH detector. Too little magnetic bending power upstream of the Trigger Tracker (TT) has an adverse impact on the ability of the experiment to trigger on an event of interest[71]. The RICH1 shield provides the means by which the magnetic field can be modified such that these two conflicting requirements can be satisfied. The RICH1 shield box is a 16 tonne iron structure that surrounds RICH1 and channels the magnetic field away from the HPDs, concentrating it in the region of the beamline, to provide bending power upstream of the TT. The design and optimisation of this structure's magnetic characteristics and the measurements of the completed shield are the principal topics of this chapter.

The late introduction of the RICH1 magnetic shield was prompted by the 'lite' redesign[45] of the LHCb detector. This was the decision by the LHCb collaboration to remove material from within the spectrometer's acceptance, after technological constraints led to an increase in the amount of material contributed by each sub-detector. This would have increased the quantity of scattering to a point where several important physics channels, specifically those requiring a large number of charged tracks to be reconstructed, would have suffered an unacceptably high loss in reconstruction efficiency. In the new design a number of tracking stations inside the magnet were removed. The remaining tracking station, the TT, now required more magnetic bending power than was available to maintain the trigger rate. To

provide this bending power the magnetic shielding plate that protected RICH1 and the VELO was removed. This in turn required a shielding solution to protect the HPDs in RICH1 that did not attenuate the field upstream of the TT.

The RICH pixel HPDs are sensitive to an external magnetic field because of its effect on their electron optics. This causes the image on the pixel chip to be distorted by even a modest field, and limits operation to fields of less then 10G. Experiments[72] with HPDs in Helmholtz coils have demonstrated the maximum levels of transverse and longitudinal magnetic field in which the HPDs can operate. In fields up to 10G the image on the pixel chip is distorted, but it can be recovered if the magnetic field is accurately mapped, however over 10G the image is distorted to such an extent that the photoelectrons start to miss the pixel chip, causing a loss of data.

The LHCb dipole magnet and RICH1 shield system were simulated using Vector Fields' Opera3d/Tosca Finite Element Analysis (FEA) package[74]. By calculating the 3-dimensional magnetic field maps for various shield configurations, the effects of design changes could be readily determined and an optimal design approached. This method was repeated for each of the shield components in turn, optimising the RICH1 shield, while taking into account the strict mechanical constraints imposed by the limited space between the VELO and the dipole magnet.

4.1 Shielding Requirements

This section will specify the performance requirements of the RICH1 shield, and describe how they relate to the FEA design.

4.1.1 Shielding the Photon Detectors

Measurements[72] of HPDs in a Helmholtz coil have demonstrated that the performance of an unshielded tube rapidly degrades beyond an acceptable level at a field strength of around 10G. Results are shown in Figure 4.1. Initially this meant that the design target of the magnetic shielding was to reduce the field in the HPD region to less than 10G. This proved to be extremely difficult to achieve, and so the decision was taken to allow the HPDs to operate within mumetal tubes with 2mm

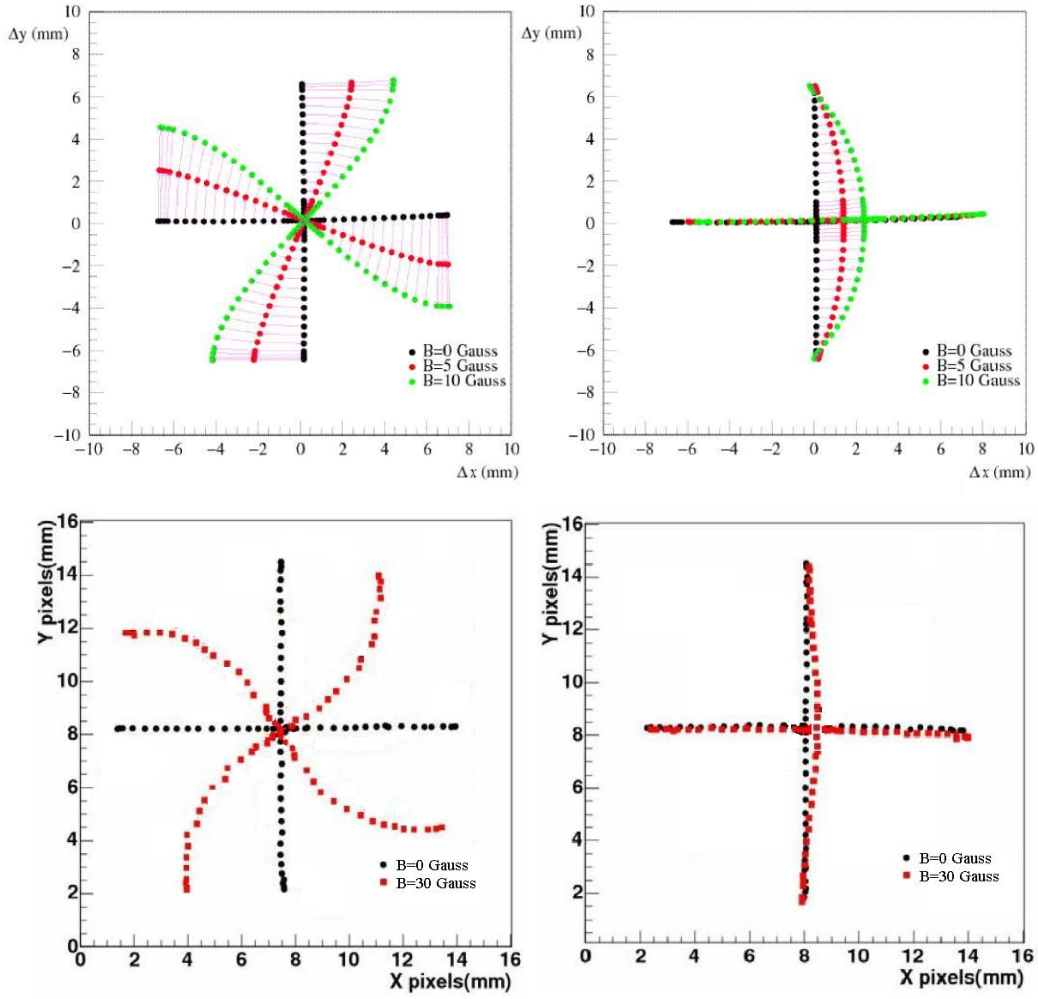

Figure 4.1: Comparison of image distortions with unshielded (top) and shielded (bottom) HPDs. The upper figures are for axial field (left) and transverse field (right) up to 10G. The lower figures show the results for a shielded tube in a **B** field of 30G, axial (left) and transverse (right).

thick walls.

Figure 4.1 (lower) shows that when enclosed within a local mumetal shield an HPD can operate in fields of up to 30G before the image of the photocathode spills over the boundary of the pixel sensor, resulting in an irrecoverable loss of data. However even with this shielding the significant distortions in mapping from the photo cathode to anode must still be corrected. This led to the specification for the maximum field on the HPD plane being relaxed from 10G to 25G, a level at which the HPDs could operate with software image correction and magnetic field monitoring.

FEA simulations, later confirmed by measurements, predicted that the maximum field in the HPD region without the presence of any iron shielding would reach approximately 600G. This means that the combination of global and individual shielding is required to provide a field attenuation of a factor of 60.

4.1.2 Providing the Trigger Field

In addition to shielding the HPDs, the RICH1 shield has to increase the amount of bending power available between the interaction point (z=0) and the TT (located at z=250cm) to improve the momentum precision of the tracker. The bending field requested by the trigger group [71] is defined as an integral along a line (chosen for its convenience) from the interaction point to the position of the TT with a value of at least 150kGcm, shown in Figure 4.2. Due to the symmetry of the situation and the proposed shape of the shielding box, the integral is a line of minimum field (in x), consisting entirely of the $\mathbf{B}_y$ component. FEA simulations without any shielding predict a value of 121kGcm. This means that the RICH1 shield is expected to actually increase the field in the trigger region with respect to the no shield case, rather than just avoid reducing it.

4.2 The OPERA3d FEA Package

Finite element Analysis (FEA) is a method to solve numerically partial-differential and integral equations with boundary conditions too complex for an analytic analysis. In this case Maxwell's equations are applied to a complex geometry containing

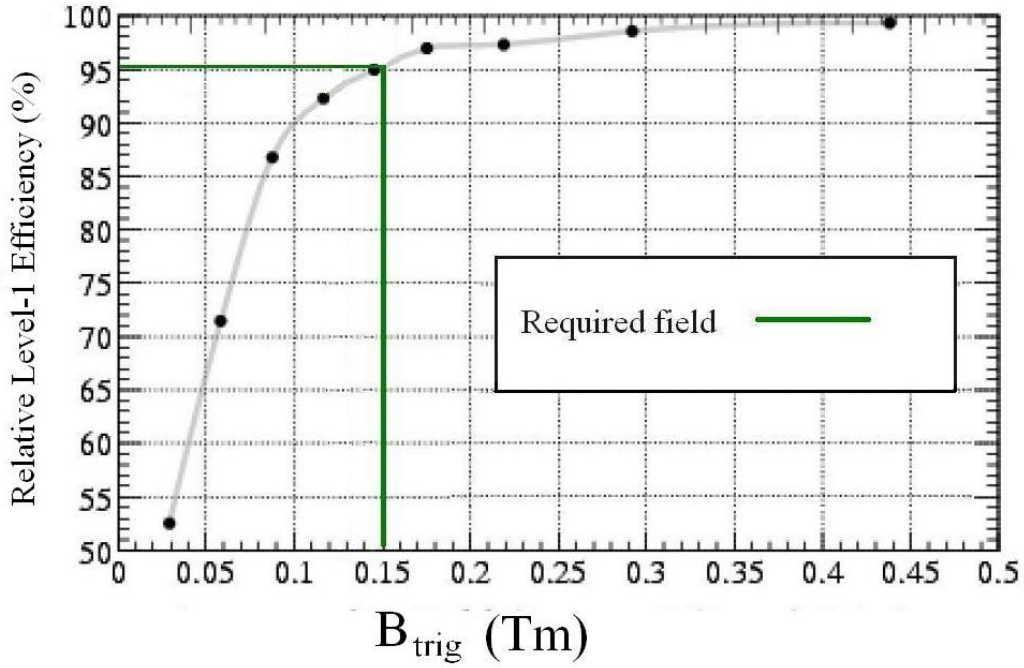

Figure 4.2: The relative efficiency of the Level-1 trigger for varying values of integral field $\mathbf{B}_{trig}$ [71].

many different magnetic volumes including non-linear magnetic material. This program is described more fully in the Reference Manual[74] and Frequently Asked Questions[75] documents.

The OPERA TOSCA sub-package is used to solve the magnetostatic equations. It takes a prepared geometry file that describes the locations of the element boundaries, the elements' magnetic properties, current volume and density and the model's boundary conditions. This is prepared in the OPERA preprocessor package and passed to the TOSCA calculator that returns a database of values to be interpreted by the post processor.

The finite element method requires the numerical solution for a variable to be found on a finite number of spatial coordinates. These are the corners of a 'mesh' of four or six sided volume elements that are compatible with the geometry of the model. Whilst the mesh is generated semi-automatically, it is up to the modeller to ensure that there is a high density of elements in the regions where a precise solution is required, or the granularity of the model requires a corresponding granularity of

elements. As the model cannot extend to infinity, boundary conditions have to be specified and can enforce a set field at a boundary or field lines perpendicular to the boundary to simulate a reflected geometry.

The differential form of Maxwell's equations are:

$$\begin{gathered} \nabla.\mathbf{D} = \rho \qquad\qquad \nabla.\mathbf{B} = 0 \\ \nabla \times \mathbf{E} = -\frac{\partial \mathbf{B}}{\partial t} \quad \nabla \times \mathbf{H} = \mathbf{J} + \frac{\partial \mathbf{D}}{\partial t} \end{gathered} \tag{4.1}$$

where $\mathbf{D}$ is the electric displacement field, $\mathbf{B}$ is the magnetic flux density, $\mathbf{H}$ is the magnetic field, $\mathbf{E}$ is the electric field, $\mathbf{J}$ is the current vector and ρ is the current density.

The magnetic property of a material is characterised by a curve of $\mathbf{B}$ vs $\mathbf{H}$. The permeability is defined through:

$$\mathbf{B} = \mu \mathbf{H} \tag{4.2}$$

where, for non-linear magnetic material, μ is a function of $\mathbf{B}$. $\mathbf{B}$-$\mathbf{H}$ curves for the relevant materials in this study are shown in Figure 4.3 and relate the field found inside an initially unmagnetized material to the applied field strength, $\mathbf{H}$.

Using this definition of μ, the magnetostatic conditions and assuming a negligible amount of residual magnetization, the relevant Maxwell's equations can be simplified to:

$$\begin{gathered} \nabla.(\mu \mathbf{H}) = 0 \\ \nabla \times \mathbf{H} = \mathbf{J}_s \end{gathered} \tag{4.3}$$

where $\mathbf{J}_s$ is the source current density provided by the magnetic coils.

The OPERA system provides two methods for solving the situation, the 'total' scalar potential (TSP) and the 'reduced' scalar potential (RSP). In the TSP strategy $\mathbf{J}_s$ is set to 0, so the method can only be used in regions without a current density. In this case a solution to equation 4.3 can be written in terms of the scalar potential ϕ_T:

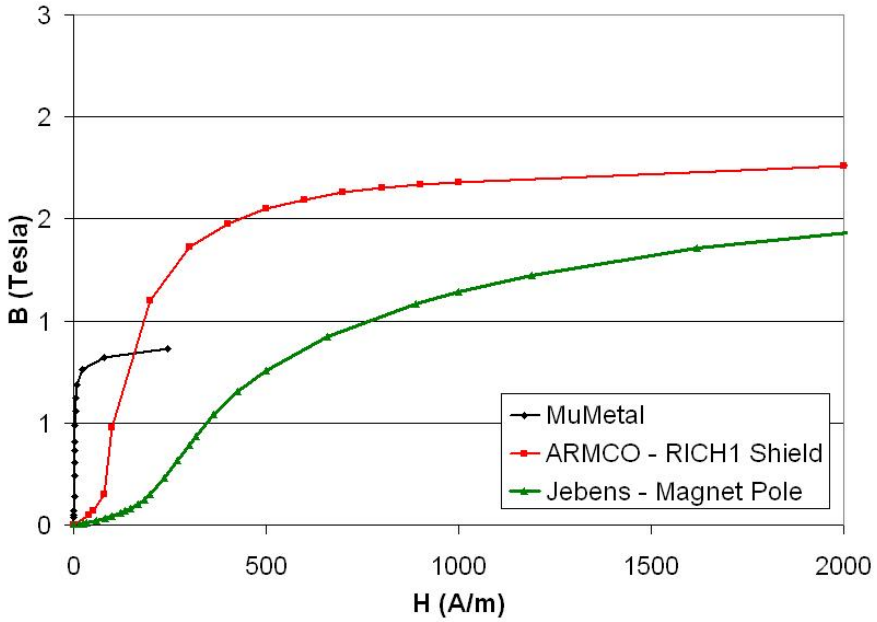

Figure 4.3: The magnetic properties of the Jebens iron used for the dipole magnet, the low carbon ARMCO used for the RICH1 shield and the mumetal for the local cylindrical shields.

$$\mathbf{H} = -\nabla\phi_T \tag{4.4}$$

$$\nabla.\mu\nabla\phi_T = 0 \tag{4.5}$$

If there are currents present in the system the RSP must be used. This adds an extra term to equation 4.4:

$$\mathbf{H} = \mathbf{H}_s - \nabla\phi_R \tag{4.6}$$

where ϕ_R is the reduced scalar potential and $\mathbf{H}_s$ results from the presence of $\mathbf{J}_s$ and can be calculated directly from the Biot-Savart law.

The RSP method should, in principle, provide a solution to all regions of the model. However in practice it can lead to large errors in regions that are shielded from the direct effects of the current, or in materials with a non-linear magnetic response. To avoid these problems a mixed method is used, where the type of solution required

is set in the pre-processor by the modeller for each individual element.

Figure 4.3 demonstrates that all the magnetic regions of the model have a very non-linear response. The field components in these non-linear volume elements are calculated iteratively using a Newton-Raphson method[76]. The level at which the solution is considered to be stable is set to either a maximum of 50 iterations, or a convergence tolerance of 0.475G.

4.3 Initial Shielding Investigations

This section describes the first steps of the evolution of the RICH1 shield carried out by my colleague S. Jolly. This work is described in more detail in his Thesis[77].

4.3.1 Individual Cylindrical Shields

Initially a series of FEA studies were performed[78] to determine whether it would be possible to only shield the HPDs individually in iron, or mumetal cylinders. A quarter symmetry tube was modelled in a background field corresponding to that expected from the magnet, as it was not possible to model features as small as those of the tube along with the full dipole magnet.

These studies showed that concentric iron and mumetal cylinders with a total of 6mm wall thickness, and extending up to 40mm beyond the photo cathode, reduced the field at the photo cathode to 10G. However this model is for only one HPD in a set field. It is possible an array of iron or mumetal shields would draw field in from the magnet, potentially causing the shields to saturate. In addition the 40mm overhang shades the photocathode from photons with a high angle of incidence; the 6mm-thick shielding results in a loss of sensitive area coverage, so that the number of photons lost becomes unacceptably high. For these reasons the cylindrical shields were not pursued.

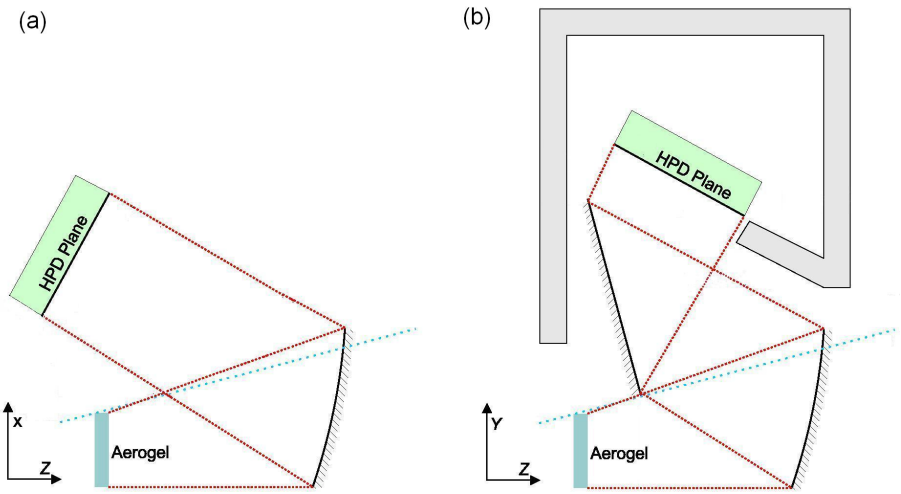

Figure 4.4: One half of the RICH1 detector, shown before the redesign (a) with HPDs to the left and right of the beam line, and after the redesign (b) where the HPDs are located above and below the beamline and surrounded by an iron shielding box. This vertical design also includes additional flat mirrors. [77].

4.3.2 Initial Shielding Boxes

To achieve a substantially greater shielding effect, an iron box that enclosed all the HPDs (similar to that of RICH2[79]) had to be developed[80][81]. However the RICH2 shield was designed for a field of at most 150G, whereas in RICH1 a field of 600G needs to be attenuated. It quickly became apparent that this would require secondary flat mirrors to allow the HPDs to be positioned further from the beamline. This change in the optical design, and the addition of a shielding box is shown in Figure 4.4. Initial FEA models showed that a horizontal shield box configuration pulled field away from the beamline, thus reducing the bending power within the spectrometer acceptance, where it is required for the tracking trigger. This was solved by rotating RICH1 to the vertical and using the shield itself to channel the field back to the trigger region. This design was then developed by the author, and the process is described in the following section.

4.4 The Vertical RICH1 Shielding Box

This section describes the design and optimisations of each component of the shield. Reference will be made to the LHCb axes. Specifically, these are; a horizontal x, a vertical y, and z running from the interaction point downstream along the beamline, forming a right handed set of coordinates with the origin at the interaction point.

From the requirements presented in Section 4.1, two criteria for the success of a shield model were determined. $\mathbf{B}_{max}$, the peak value on the HPD's photodetector plane, and $\mathbf{B}_{trig}$, the integral field along the beamline from the interaction point to the TT. The targets were set as $\mathbf{B}_{max}$ not exceeding 25G and $\mathbf{B}_{trig}$ being greater than 150kGcm. Thus the task of the shield is to reduce field in the HPD region by a factor of 25 and to increase the integral field by 20%.

As illustrated in Figure 4.5 the RICH1 magnetic shield is designed to attract field from the region near the magnet coils, and to direct it through the top plate (away from the HPDs), down the front plate to the beamline where it increases $\mathbf{B}_{trig}$.

The design was based on the principle of creating a route of least reluctance by putting as much iron as possible in the desired field path. In addition the HPDs were enclosed as much as possible to prevent stray field entering the area. Whilst this does not totally remove the field from the HPD region, it reduces it to a level where the mumetal shield can be effective. Two additional factors for the optimisation procedure are the overall weight of the structure, that needs to be reduced as far as possible, and the available space between the VELO and the TT detector.

4.4.1 Components of the RICH1 Shield

To provide a conceptual framework to allow geometry changes to be discussed conveniently, the description and analysis of the shield is broken into a series of sections or plates. These correspond to sides and parts of the shielding box. These plates are investigated individually using FEA, to remove any ambiguity in the cause of an observed effect.

The plates that were included in the final design are shown in Figure 4.6 and listed

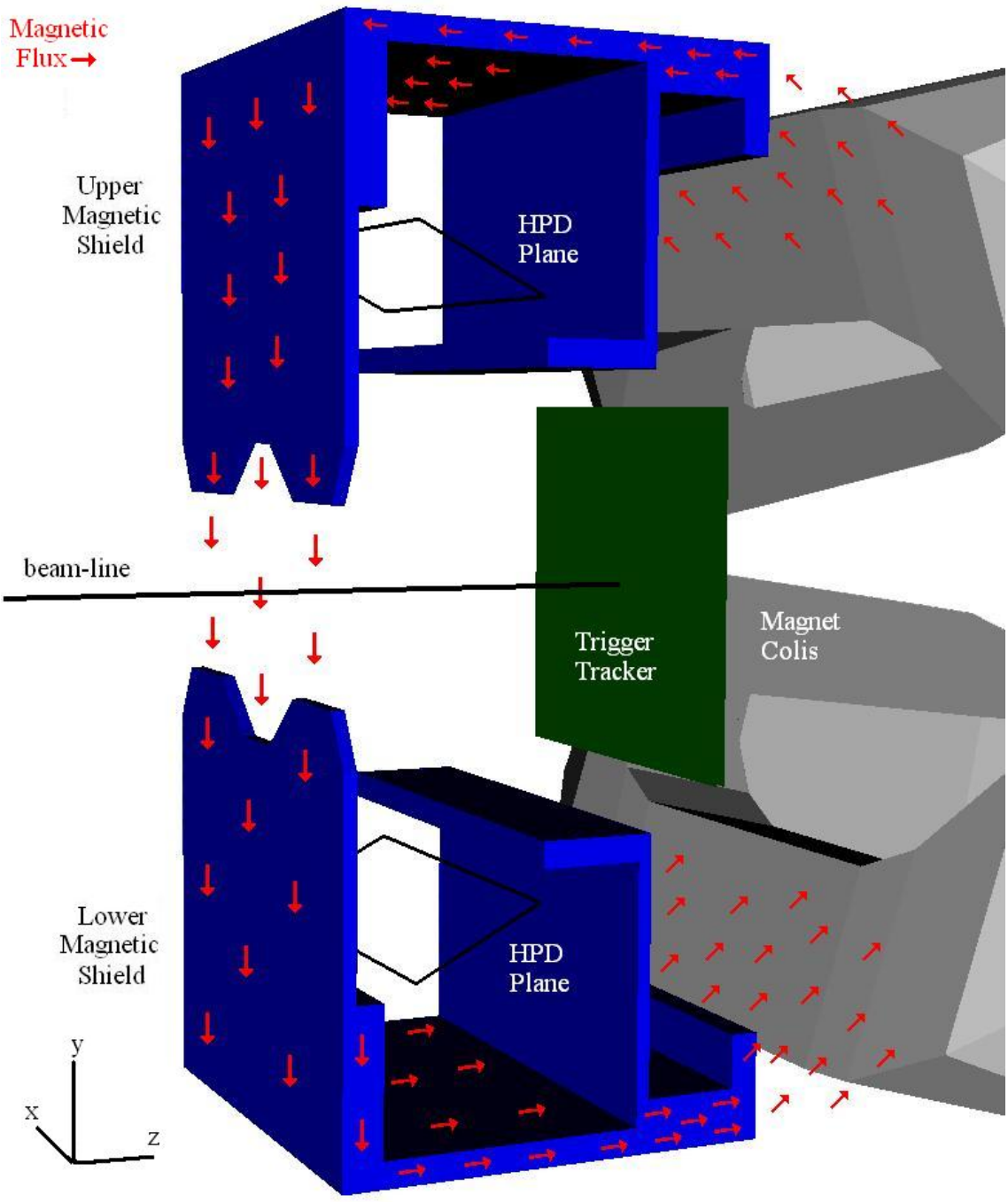

Figure 4.5: A diagram showing the intended field path that drove the design of the RICH1 magnetic shield.

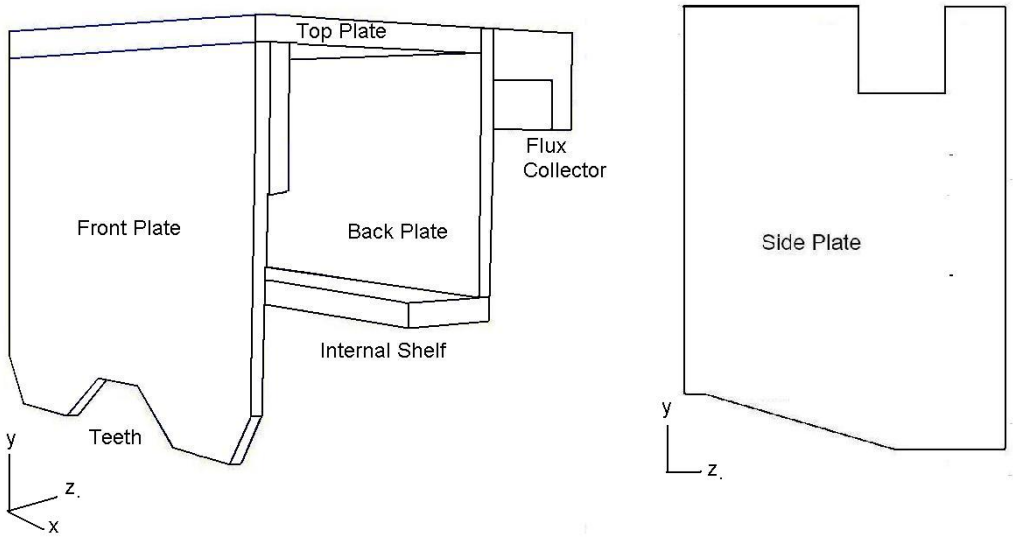

Figure 4.6: The components of the upper RICH1 shield.

below. The descriptions in following sections relate to the upper shield when discussing the 'top' or 'bottom' of a plate. These are mirrored in the lower half of the shield.

- The front, or upstream plate; incorporating the internal block and the 'teeth'.
- The side plates.
- The internal shelf.
- The back, or downstream plate.
- The magnetic block, or flux collector.

All components of the shield were modelled as ARMCO[1] iron, a very pure iron with good magnetic properties, i.e. a high saturation field and low coercivity.

4.4.2 The Upstream Plate

This plate forms the upstream wall of the shield box. It plays an important role as it directs the field into the optimal region for increasing $\mathbf{B}_{trig}$. It is in a mechanically

[1]A brand (and former name of) AK Steel, Ohio, USA

congested area, as it is adjacent to the VELO, the flat mirror supports and the seal between the VELO and the RICH1 gas enclosure.

FEA models indicated that this plate was critical to the values of both $\mathbf{B}_{trig}$ and $\mathbf{B}_{max}$. As it is extended (in y) closer to the beamline, bringing the two front plates together, $\mathbf{B}_{trig}$ increases and $\mathbf{B}_{max}$ decreases. This is shown in Figure 4.7 and is one of the few geometry changes that has a positive effect on both $\mathbf{B}_{trig}$ and $\mathbf{B}_{max}$. As a balance between the two parameters did not have to be taken into consideration, the plates were extended to the limits set by the mechanics.

In the ideal case the plates would extend to the LHCb acceptance, however this was not possible. The agreed installation procedure for the VELO exit window and the associated seal to the gas enclosure required these components to be inserted between the front plates. This called for enough clearance for the seal to pass through and be attached to the VELO. This set the limit in y for the extent of the front plate to $\pm$55cm.

As the VELO exit window and the seal are both circular, pieces were added to the front plate to allow it to fit around them. These teeth pieces, shown in Figure 4.6, have little impact on $\mathbf{B}_{trig}$ as they are off centre, but decrease $\mathbf{B}_{max}$ by approximately 10%. Their effect on the field can be seen clearly in Figure 4.8.

The other parameter of this plate that was investigated using FEA was its thickness (in z). Clearly having a thicker plate eases the magnetic path, and this is borne out by the FEA (shown in Figure 4.9). The shield was originally designed with a 10cm thick upstream plate, however this had to be reduced to 5cm to allow space for adjustable mounts for the flat mirrors. To compensate, the plate was increased to 15cm thick at its upper end where it joins the top plate. This and the surrounding mechanics are shown in Figure 4.10.

4.4.3 The Magnetic Flux Collector

More often referred to simply as the magnetic block, this piece of the shield is designed to draw flux from the magnet and increase $\mathbf{B}_{trig}$. In essence the flux collector is a large mass of iron attached to the downstream plate in close proximity to the coils of the magnet. The block was not present in the initial shield box

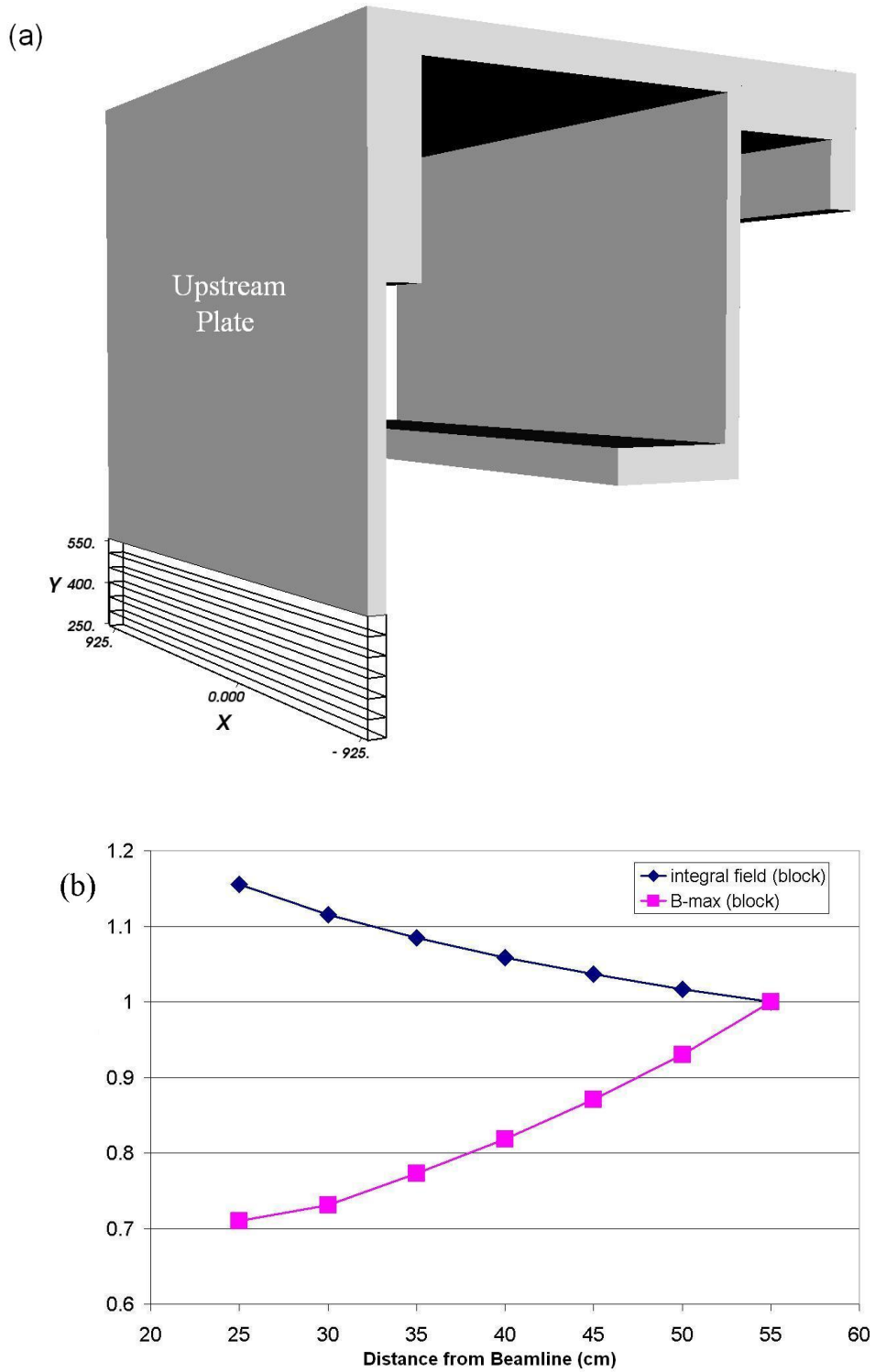

Figure 4.7: (a) The front or upstream plate is shown, indicating a series of geometry changes, increasing the extent to which the plate reaches towards the beamline at $y = 0$. The lower plot (b) shows how the integral field ($\mathbf{B}_{trig}$) is increased and the field at the HPD plane ($\mathbf{B}_{max}$) is decreased by reducing the gap between the upper and lower front plates. The scale is normalised to the values of $\mathbf{B}_{trig}$ and $\mathbf{B}_{max}$ at y = 55cm.

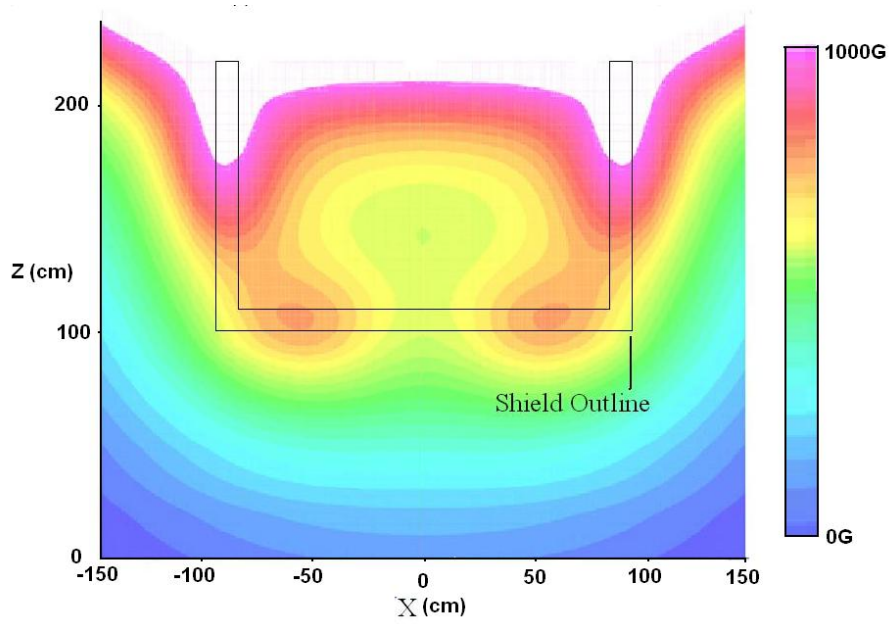

Figure 4.8: The field magnitude on the $y = 0$ plane, the circular regions of high field caused by the presence of the teeth are clearly visible.

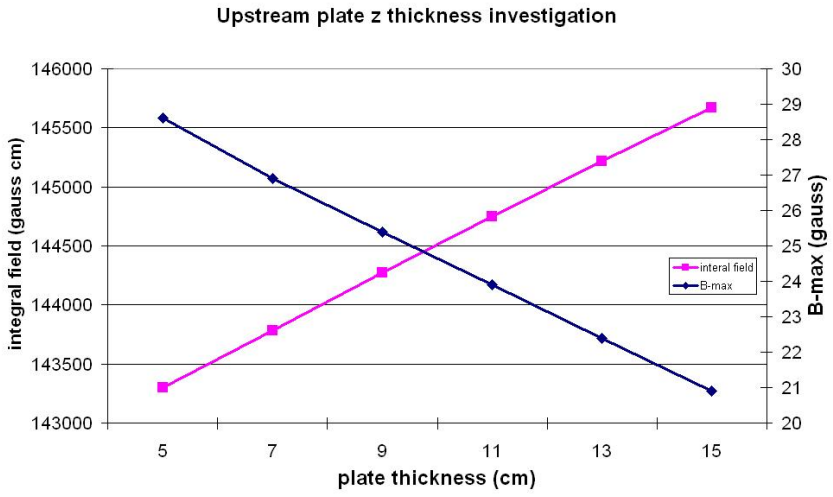

Figure 4.9: As the thickness of the upstream plate is increased (with y held at 55cm), the magnetic impedance is reduced, increasing the magnetic field at the beamline and reducing the field at the HPD plane.

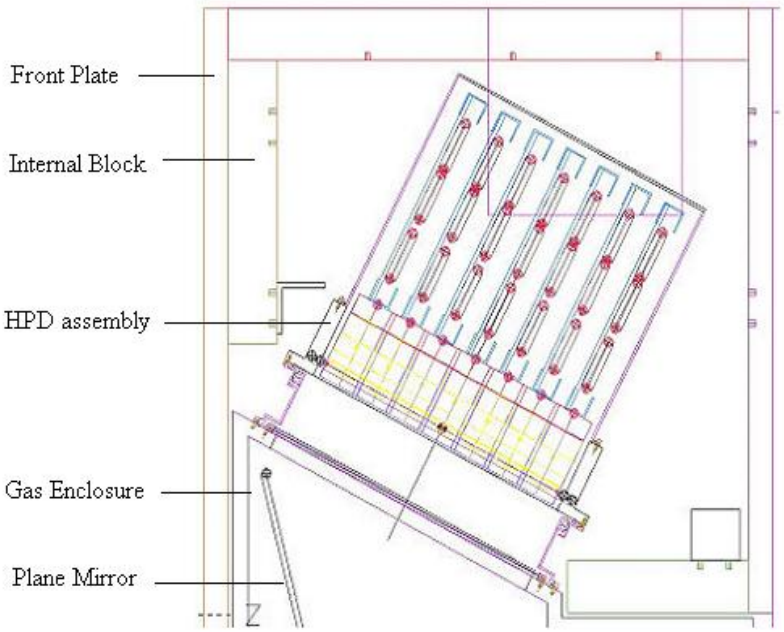

Figure 4.10: A schematic of the area around the plane mirror mountings showing the tight mechanical constraints in the area of the front plate. Note particularly the proximity of the plane mirrors, their attendant mounts and the gas enclosure.

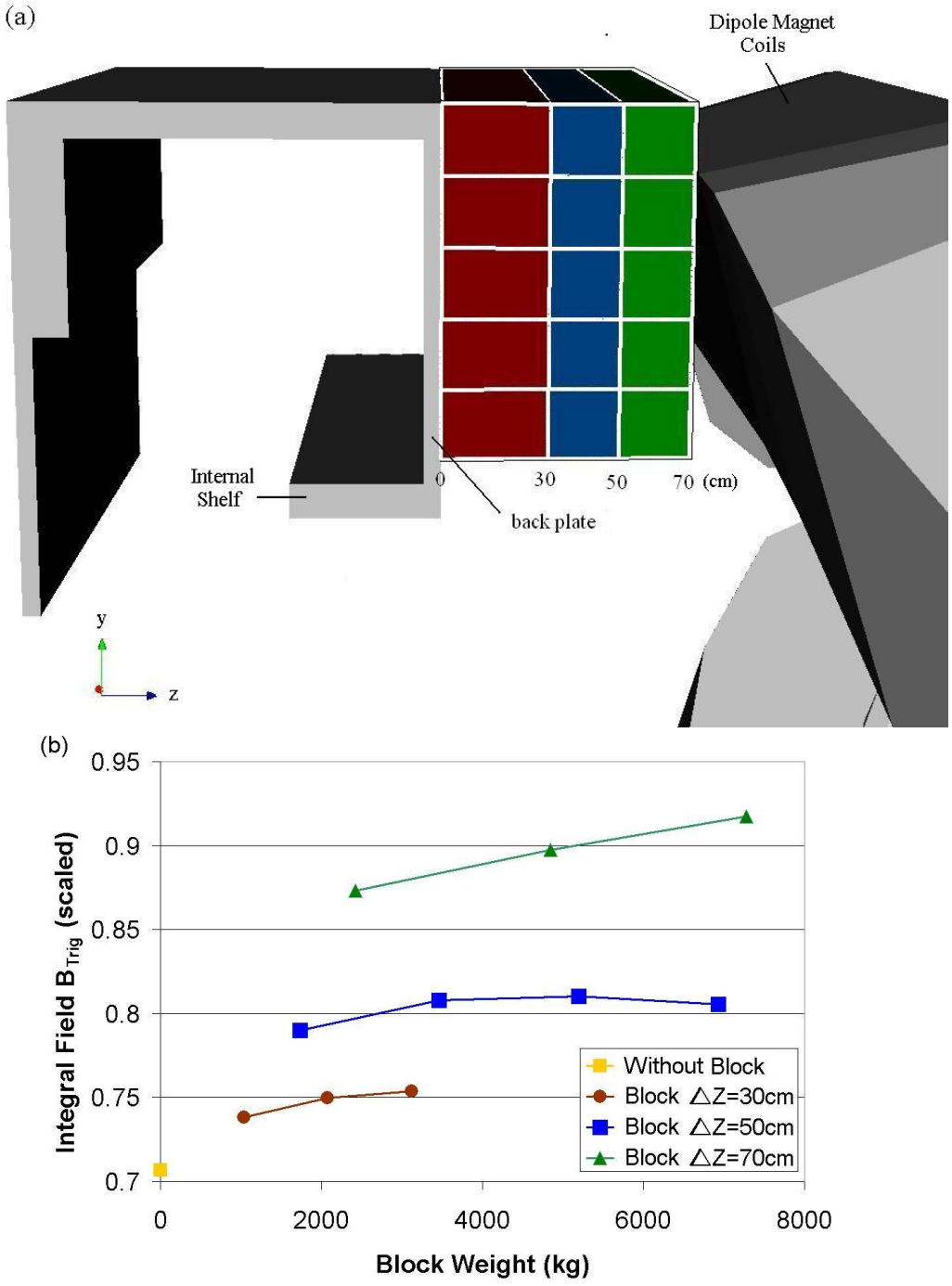

Figure 4.11: (a) A cross section of the proposed shielding, showing the various configurations of the magnetic block that were modeled in the series of calculations used to determine the effectiveness of the block. (b) The integral field $\mathbf{B}_{trig}$ plotted against the weight of the block and separated into series defined by the z-extent of the block, and hence its proximity to the coils of the dipole magnet. For each Δz (measured from the back plate) several values of Δy (measured from the top of the shield) were modelled and plotted according to the weight of the block. The colours in (a) corresond to the colours of the appropriate points in (b).

designs, however as changes to the upstream features reduced the expected values of $\mathbf{B}_{trig}$ it was deemed necessary. The presence of the block has an adverse effect on $\mathbf{B}_{max}$.

There are no strong mechanical constraints affecting the flux collector. It is limited by it weight, the position of the magnet and the position of the TT. These loose boundaries left a large area of parameter space to be scanned by FEA. Figure 4.11(a), shows the modular approach that was used, switching in turn the composition of different volumes between iron and air to allow the system to be scanned quickly.

The results of the FEA demonstrated that it was not the mass of the block that had the greatest impact on $\mathbf{B}_{trig}$, but instead its proximity to the magnet. This is shown in Figure 4.11(b). In addition the value of $\mathbf{B}_{max}$ was not primarily influenced by this proximity, as seen in Figure 4.12. This allowed $\mathbf{B}_{trig}$ to be increased without causing an unacceptable increase in $\mathbf{B}_{max}$ and consequent loss in the efficiency of the HPDs.

To minimise the weight of the block, it was reduced to a 20cm thick plate, the width of the shield, extending as close as possible to the magnet's coils. To minimise $\mathbf{B}_{max}$ it was positioned in line with the top plate, to allow the flux to be directed away with no chance of saturating the back plate. Positioning the block in this way also encouraged field to be pushed forward to the front plate, rather than down the back plate, where the shorter lever arm to the TT meant it would be less beneficial to the required transverse displacement of tracks at the TT chamber.

4.4.4 The Internal Shelf

The internal shelf is positioned as shown in Figure 4.13. It reduces the opening in the box around the HPDs to the gap necessary for the Cherenkov light. This piece is critical to the shielding of the HPDs and has almost no effect on the integral field. The shield's performance is highly dependent on the size of the z-dimension of the opening in front of the HPD plane, with the field in the HPD region increasing by 30% after a change of just 6cm, as can be seen in Figure 4.14.

Again this region is mechanically very congested. Initially the change from an angled shelf to a straight shelf as shown in Figure 4.13 was able to provide more

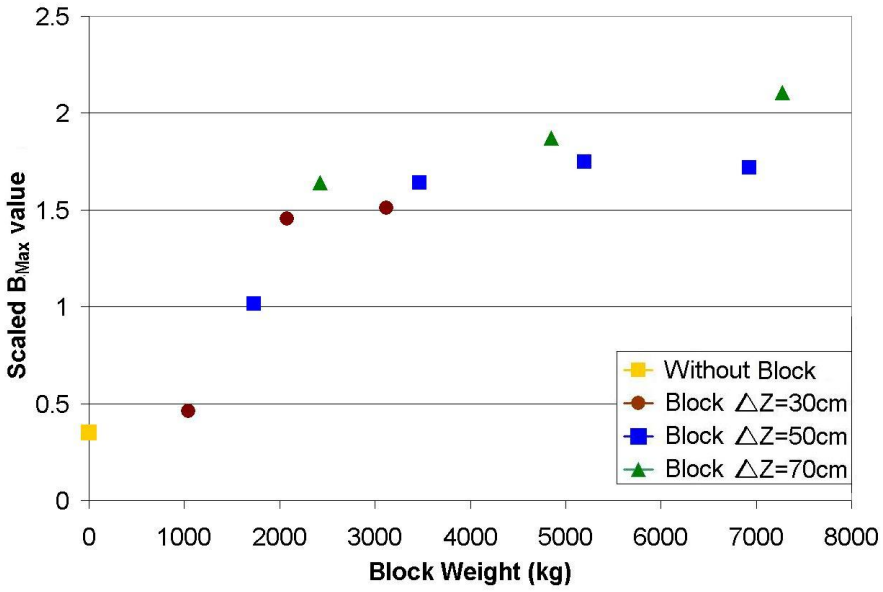

Figure 4.12: The maximum field on the HPD plane $\mathbf{B}_{max}$, again plotted against block weight with the same series as Figure 4.11. This shows that proximity to the magnet can be achieved without a dramatic increase in $\mathbf{B}_{max}$.

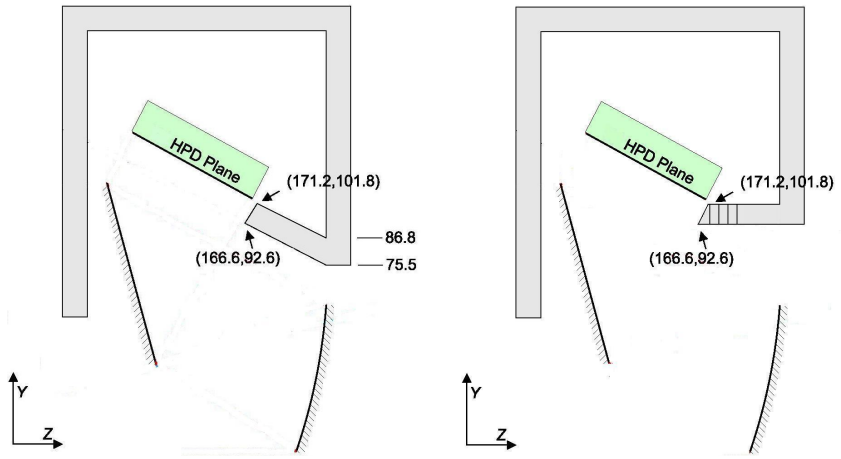

Figure 4.13: (Left) The original configuration of the internal shelf, angled to follow the edge of the proposed light cone between the mirrors (dimensions in cm). (Right) The new configuration of the internal shelf, with an angled edge to match the original positions and then several length reductions to allow space for the quartz window mountings and the nitrogen seal mechanics.

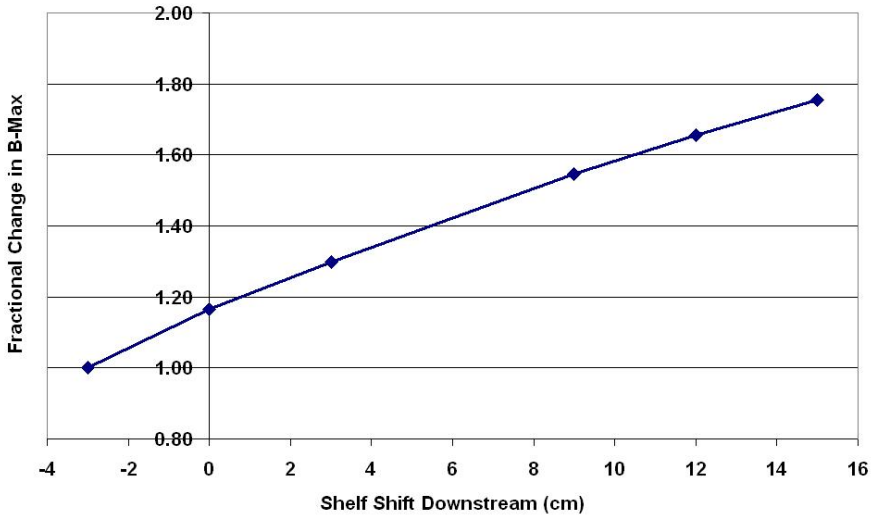

Figure 4.14: The fractional change in $\mathbf{B}_{max}$ as the internal shelf is shortened, as shown in Figure 4.13.

space for the spherical mirror mounts. However, it was decided that the aperture had to be increased at the expense of magnetic performance to allow room for the mechanics of the quartz windows, a light tight photon funnel and for a seal to the HPD enclosure. The profile of the end of the shelf was changed from angular to squared off, compromising the magnetic performance, to simplify manufacture with possibility of later shaping to fit more closely to the (at the time undefined) design of the other components.

4.4.5 The Side Plates

The side plates form the $\pm x$ sides of the shielding boxes. The FEA studies indicated that changing the geometry of these plates has less of an effect on the shield's performance than the parts discussed previously in this chapter. The two major parameters that were set using FEA were the y extent (its proximity to the beamline), and the thickness. The y extent of the plates allows the magnetic performance of the entire shield to be 'tuned', balancing $\mathbf{B}_{max}$ and $\mathbf{B}_{trig}$. By extending the plates towards the beamline the field was 'short circuited' away from the front plate, reducing $\mathbf{B}_{max}$ and $\mathbf{B}_{trig}$. Conversely retracting the plates away from the beamline increased both. This effect is shown in Figure 4.15. It was decided that the weight

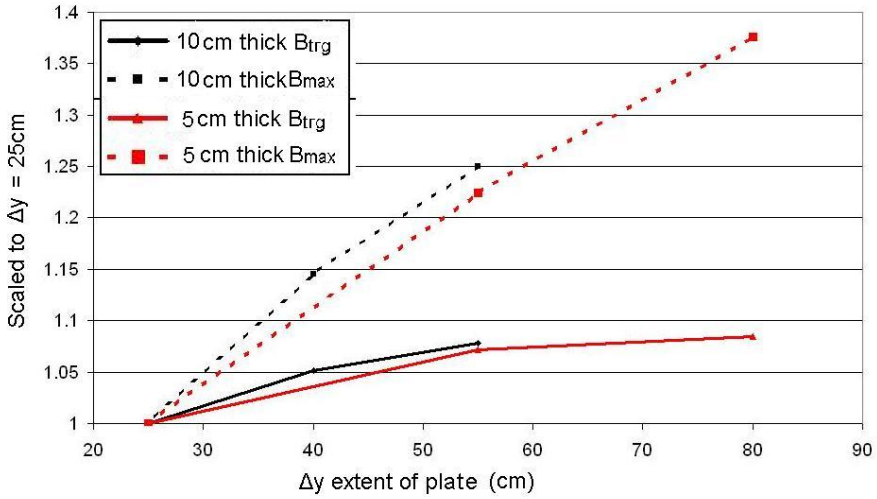

Figure 4.15: This plot shows the relative change in both the $\mathbf{B}_{max}$ and $\mathbf{B}_{trig}$ with different vertical (y) extents of the side plates. It also shows there is only a small increase in field values when the thickness of the plates is reduced from 10cm to 5cm.

saving offered by reducing the plates from 10cm to 5cm thick was justified, as the effect on the performance was negligible.

The side plates play an important role in the mechanics of the shield, and so have had more design iterations than the FEA study suggests. They are critical to the mechanical stability of the shield, important due to the HPD mountings, but also have to be removable to allow access to the HPDs and optics. In addition cables and coolant pipes must be routed to the HPD enclosures. Several variants of split and stepped shields were considered. Finally a solid shield with a 40cm by 40cm slot for cable routing was adopted. This meant the shields could be raised or lowered away from the services with minimal risk.

4.4.6 The Top and Back Plates

FEA studies allowed the top and back plates to be reduced to a minimum thickness in order to reduce their weight, whilst avoiding any possibility of saturation and consequent leakage of field into the HPD region. Thickneses of 10cm and 5cm respectively were deemed to be adequate for the top and back plates. No real benefits

to the magnetic performance were found by making these plates thicker, and doing so would have caused problems in the congested region of the HPD electronics.

4.4.7 Shield X-Dimensions

Investigations were carried out into the effect of the width of the shielding box on the magnetic performance. The general trend was to improve the performance as the shield box became narrower. Whilst this is another effect that can benefit both $\mathbf{B}_{trig}$ and $\mathbf{B}_{max}$, changing the width is obviously constrained by the space required for the optical components and their support/adjustment mechanics and the structure of the side plates.

4.4.8 Sub-Modeling Mumetal Cylinders

To simulate the very small features of the mumetal shields, with wall thickness of the order of 1mm, in the same FEA model as the dipole magnet with structures of the order of 10m is impossible. This is due to limitations on the number of mesh elements available to the FEA software. To model the effects of the mumetal cylinders on the RICH1 shield a sub-modeling technique had to be employed. This involved taking the boundary of a field map around the RICH1 shield, then remodeling the RICH1 shield with the mumetal tubes in place in a separate model, with much finer granularity, using the boundary conditions as an input. One limitation of this method is that it is invalid if the mumetal causes a change in the field crossing the boundary of the sub-model. The sub-modelling studies were carried out by Mitesh Patel and are described in more detail elsewhere[82].

When the tubes were modeled the field crossing the boundary between whole and sub models did not change when the tubes were added, indicating a reliable solution. The results of the model indicated that the mumetal shields worked better as an array than individually, providing better shielding to the central HPD tubes, where the unshielded field is highest. There was no indication that the mumetal was drawing field from the high-field regions in the top or upstream plates. Although the model does not predict this, there is still concern that the presence of the mumetal will cause a small part of the side plates to saturate. This would occur if there was more

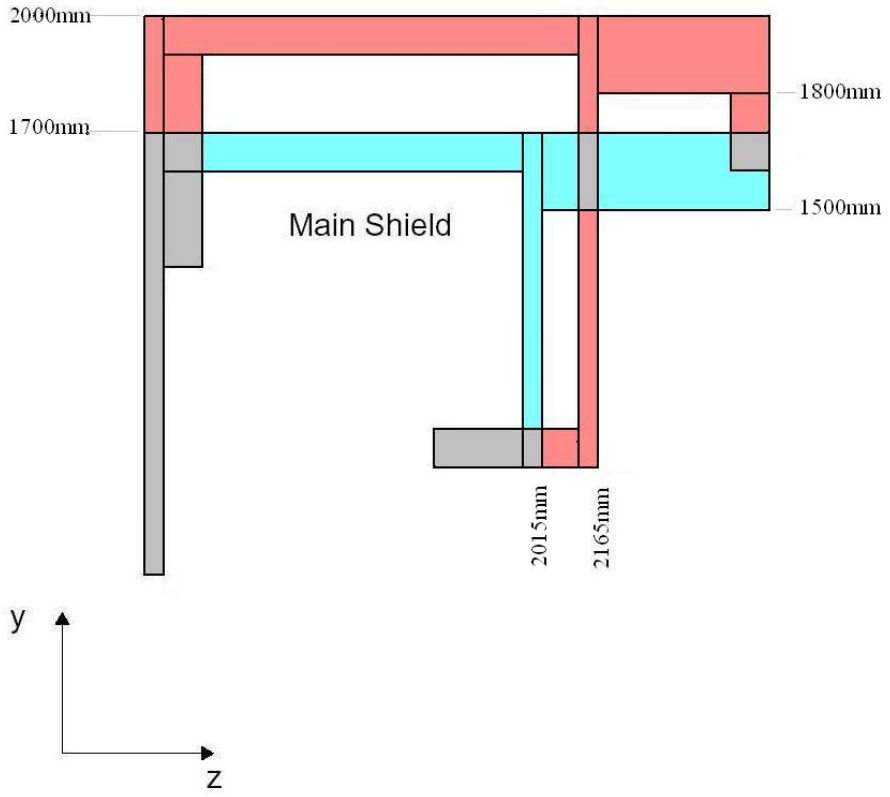

Figure 4.16: Changes made to the positions of the top and back plates to increase the space available to enclose the HPD readout electronics chain and the attendant mechanics. Blue, the optimised design; Red, the compromise finally adopted.

field than predicted by the model, and would lead to more field entering the HPD region. A solution to this is to have contingency pieces of ARMCO iron that can be bolted onto the side plates to thicken them and absorb the excess field if necessary.

4.4.9 Enclosing the Electronics

As the design of the electronics of the HPD readout system was finalised, it became apparent that the RICH1 shield would have to be enlarged if it were to accommodate the same electronics layout as would be used in RICH2. In the interests of maintaining identical photon detector systems, the RICH1 shield was increased as shown in Figure 4.16. This change resulted in a shift of balance between the integral field and

the HPD field, with $\mathbf{B}_{trig}$ being reduced by 5% and $\mathbf{B}_{max}$ reduced by approximately 2%. The change involved raising the top plate up by 30cm and moving the back plate downstream by 15cm. Moving the top plate also meant the magnetic block had to move, so an extension piece was added to maintain its function of attracting flux from the high field region close to the coils of the magnet.

Although moving the downstream plate further downstream had little effect, there were several consequences to moving the top plate up 30cm. Even with the extension block there was still a 5% reduction in $\mathbf{B}_{trig}$, and a significant increase in the amount of field in the back plate, bringing it closer to saturation.

4.4.10 Mechanical Performance

The final design of RICH1 requires that the upper HPD housing be mounted onto the upper half of the shielding, and only be connected to the gas enclosure by a flexible seal. This requires the upper shield to remain rigid under both its own weight and magnetic forces. Any detectable movement with respect to the gas enclosure would affect the spatial precision of the detector . This constraint required the side plates to be made of a single piece, and to be in place whilst the magnet is powered. ANSYS[83] simulations[84] (shown in Figure 4.17) of the shield predict that the maximum movement of the shield will be less than 200μm. The position of the HPD array is set by the rail system on the upstream plate, rather than the rail on the downstream plate, as the upstream plate is closer to the mounting point and is predicted to move less. The bottom shield supports the lower HPD box and the gas enclosure, but it is mounted on the floor and calculations indicate a much smaller displacement than the upper shield.

4.4.11 Accuracy and Initial Validation

Due to the necessary combination of the very large FEA elements simulating the magnet, the very small elements simulating RICH1 and the maximum number of computational nodes available within the FEA program, the resolution that can be achieved is limited. This is especially true in areas of high field gradient where a much higher density of elements is needed. This is compounded by the propagation

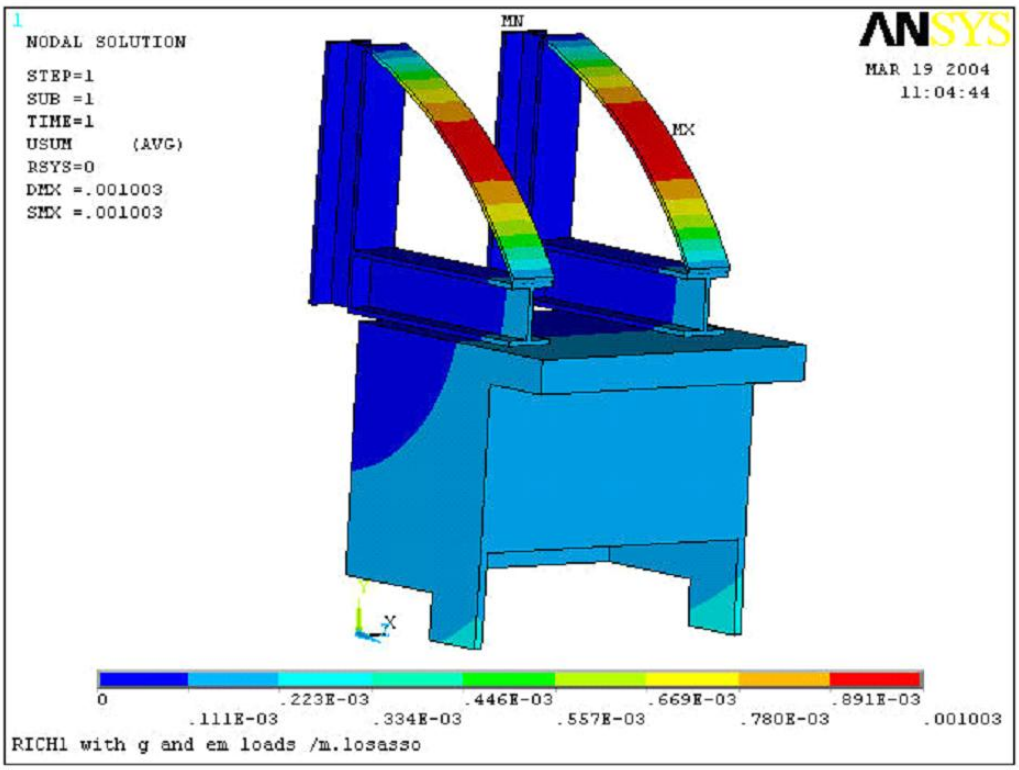

Figure 4.17: ANSYS mechanical results produced by M. Losasso indicating that the shield will be rigid enough under the loading exerted by gravity and the magnetic field. The colour coding indicates the spatial displacement from the 'unloaded' position, showing maximum values of approximately 200μm for the shield structure.

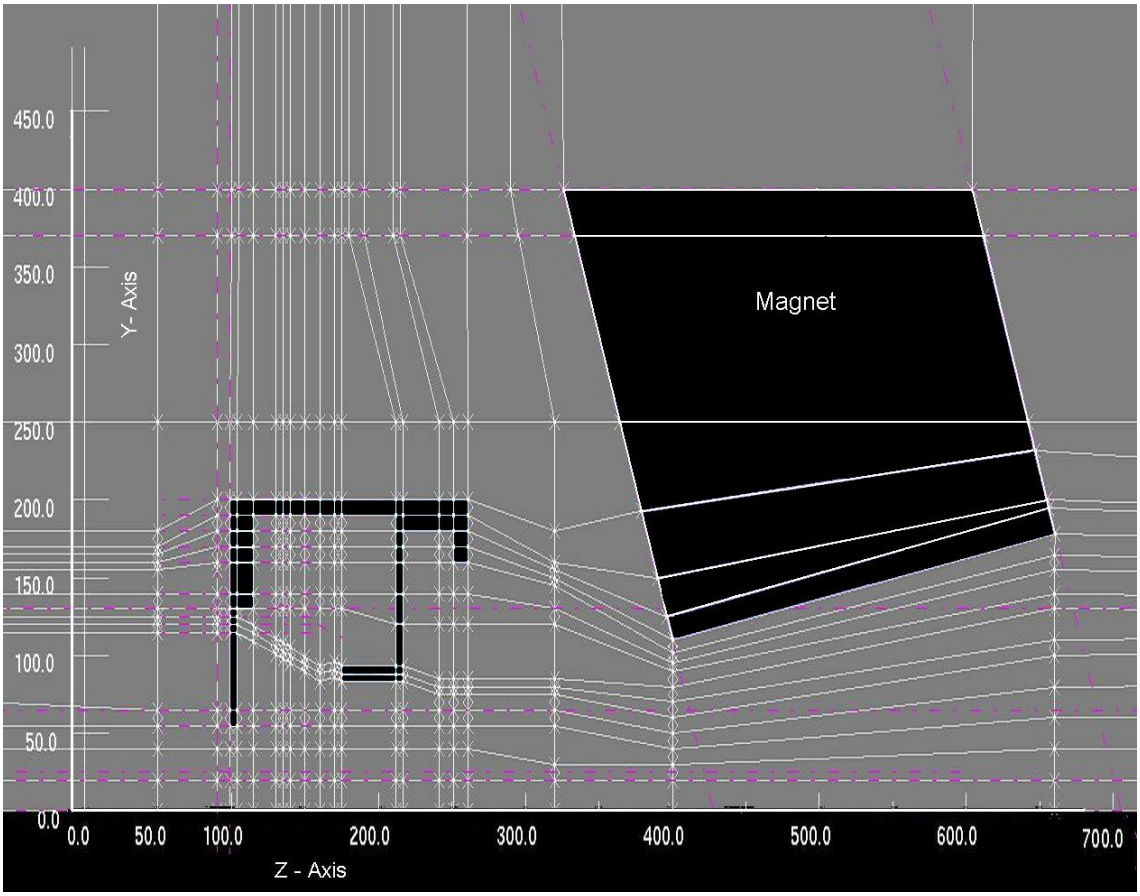

Figure 4.18: A screen-shot from the OPERA preprocessor showing the $x = 0$, y-z layer of the magnetic model and the element lines propagating out from the RICH1 shield region.

of nodes in 'layers' through the model, resulting in unnecessarily high node density in uninteresting areas. This can be seen in Figure 4.18 and is a consequence of the way the program deals with the FEA mesh. The hexahedral meshing propagates through the planes of the geometry without losing its granularity, resulting in neighbouring regions having a large number of redundant computational nodes and very elongated element shapes. This meant that the limited number of computational nodes available was being used to calculate uninteresting areas of the model whilst the region requiring greater accuracy was limited.

To address this poor granularity, the model used was changed from a half to a quarter symmetry, freeing 50% of the computational elements and providing an invaluable cross check. Changing the simulation from a half to quarter symmetry completely changed the meshing of the model, making the recovery of the same

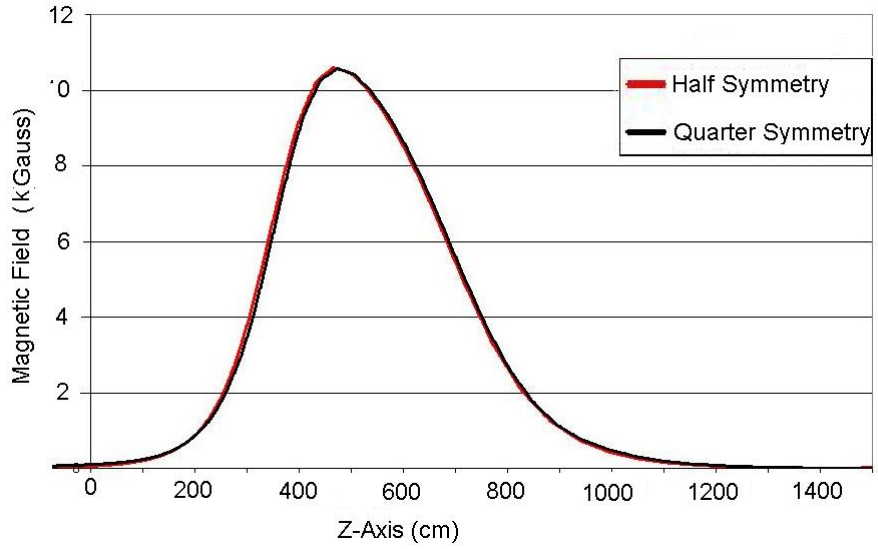

Figure 4.19: The field magnitude along the beamline predicted in half and quarter symmetry models, and indicating the compatibility of the two models.

results a valid check of the robustness of the simulation. Figure 4.19 shows the very good agreement between the models, and allowed the modelling process to proceed with a higher granularity system and the assurance that the computational results were stable under major changes to the shape of the mesh whilst the geometry of the iron was held constant.

In addition to the half and quarter symmetry models described above several other models were prepared by Marchello Lossaso (as part of the overall LHCb magnet design process) and Mitesh Patel (during the sub modelling work presented in Section 4.4.8). These simulations modelled nearly identical iron geometories with very different calculation meshes and produced results that differed by up to 20% in the most extreme of cases. However, the various models have consistently agreed on the trends in $\mathbf{B}_{trig}$ and $\mathbf{B}_{max}$ when the shield elements have been changed. This suggests that whilst the absolute values predicted may be uncertain at the level of 20%, nevertheless the shield itself will have reached the optimum performance within the mechanical limits set. The differences in the absolute numbers produced by the models are due to the difficulty of modelling the complicated shape of the RICH1 shield in a fringe field of a dipole magnet with the limited number of computational nodes available to the program.

4.5 A Summary of the RICH1 Shield Design

The final design of the RICH1 magnetic shield is shown in Figure 4.20. It details the shape and dimensions of the main enclosures, the side plates and the front plate. A full 3D model of the entire magnet-RICH1 system used for the FEA is shown in Figure 4.21.

The principal features of the shield components are listed below.

- *Front Plate and Internal Block* : The front plate is a 50mm thick plate on the upstream side of the shield box. Its proximity to the beamline is critical to improving the HPD shielding and the bending power; to further optimise this it has been shaped around the VELO seal by the addition of the 'teeth'. To increase the flux it carries it has a 100mm internal ticketing piece.
- *Magnetic Block* : The magnetic block is critical to the bending power, drawing in the magnetic flux and channeling it along the top plate away from the HPD region. Its proximity to the magnet is the key property in changing its performance.
- *Internal Shelf* : The internal shelf is a 100mm thick plate that reduces the opening below the HPDs, dramatically reducing the field in the HPD region.
- *Top Plate* : The top plate is a 100mm thick plate that channels field from the magnetic block to the front plate. If it is reduced in thickness saturation occurs.
- *Back Plate* : The back plate is a 50mm plate which directs field from the magnet away from the HPDs into the shelf. Its position is far enough from the HPDs that there is no chance of field 'jumping' into the mumetal shields.
- *Side Plates* : The side plates are removable 50mm pieces that were shaped to tune the balance of trigger vs shielding. They have 400mm by 400mm slots to allow services to the HPDs.

The final model predicts a value of $\mathbf{B}_{trig}$ of 138kGcm and a value of $\mathbf{B}_{max}$ of 26G.

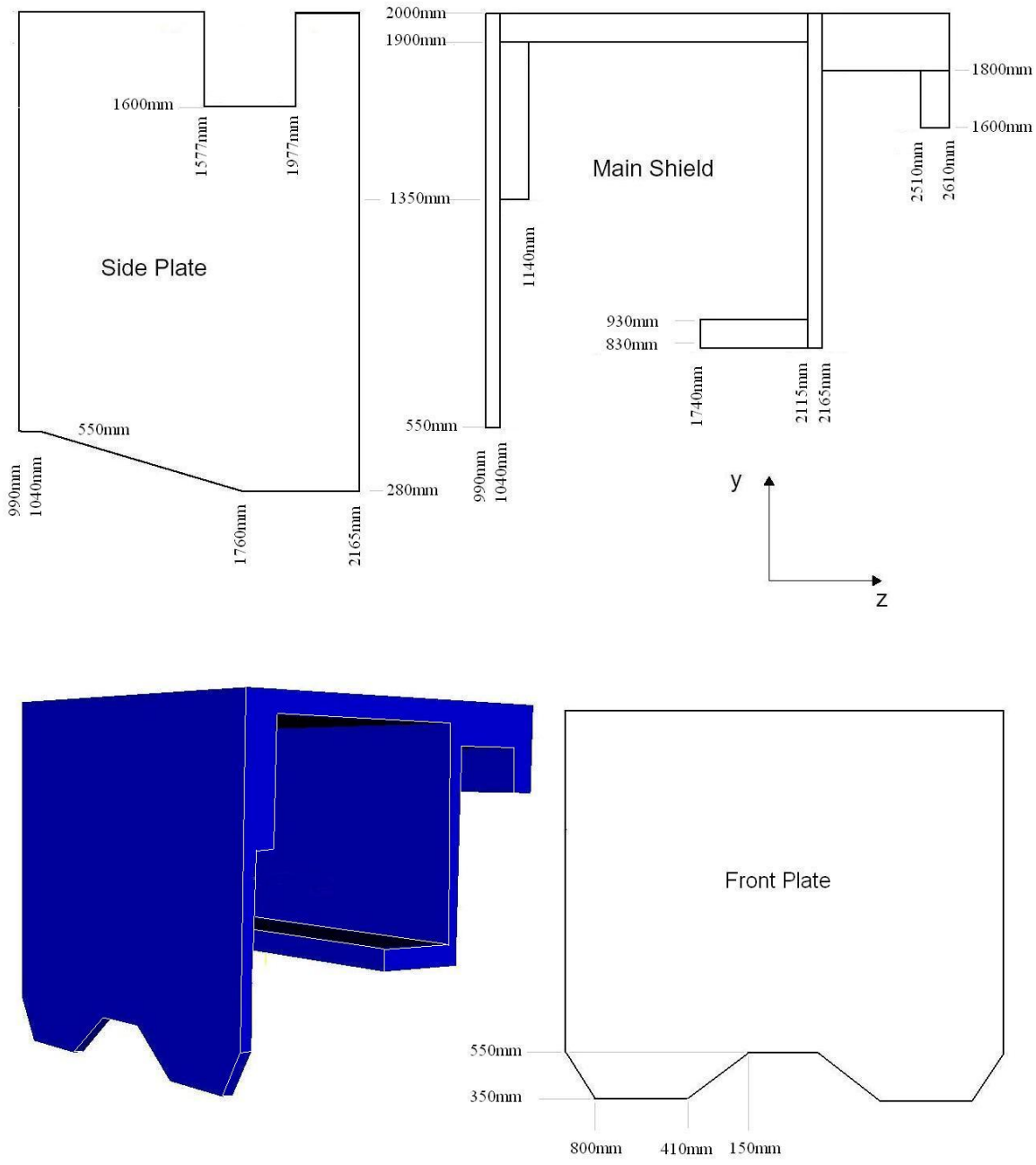

Figure 4.20: (Top Left) the design of the side plates, manufactured from ARMCO iron with a thickness of 50mm. (Top Right) A cross section showing the positions of the main components of the shield. (Bottom Left)A 3D model of the main shield excluding the side plates. (Bottom Right) Detail of the front plate, showing the design of the 'teeth'.

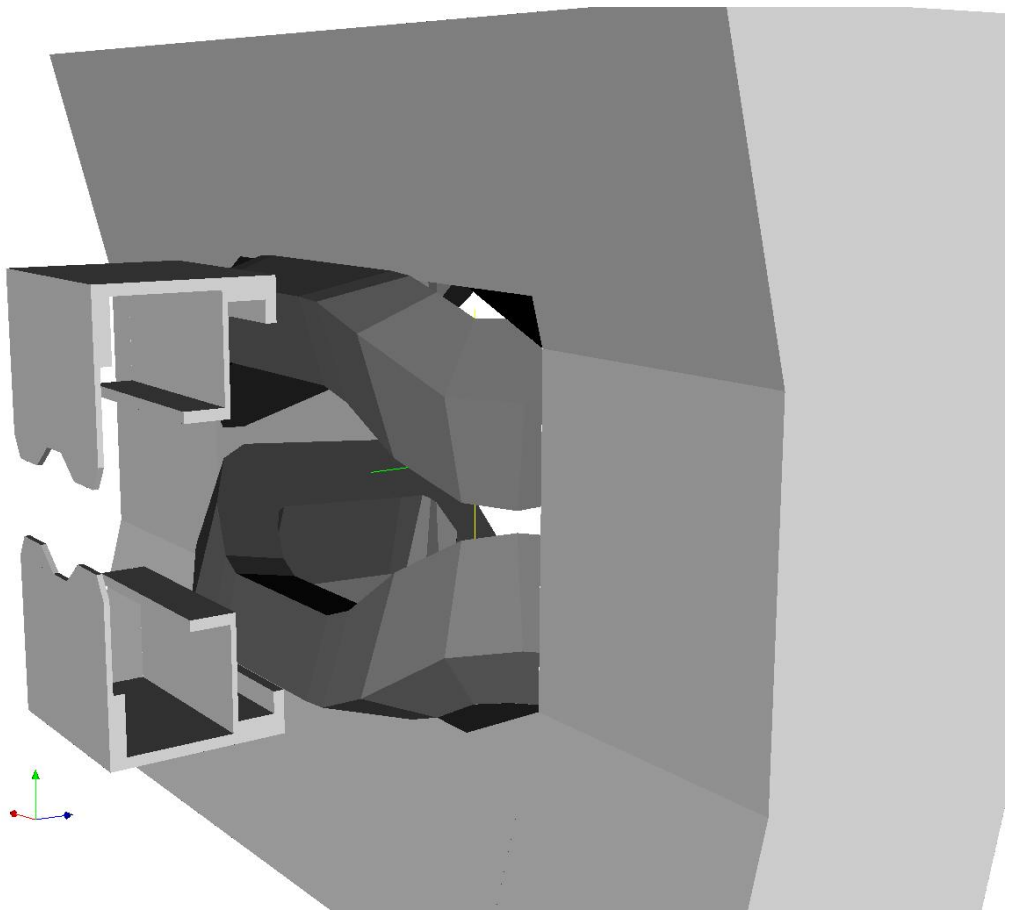

Figure 4.21: A 3D representation of the RICH1 magnetic shield without its side plates, and the LHCb dipole magnet. This image was generated from the final quarter-symmetry model used to simulate the system.

4.6 Measurements of the Field

The RICH1 Magnetic Shield was manufactured to the design shown in Figure 4.20 from ARMCO iron and delivered to CERN in April 2005. Installation at its final location in the LHCb cavern was completed in the first week of June 2005. This was immediately followed by an intensive program of magnetic measurements. The LHCb dipole magnet was powered to full field and measurements were taken throughout the LHCb acceptance and within the RICH1 HPD region.

The main series of measurements were made using a semi-automatic mechanical system[85] to map the main acceptance region within, and upstream of, the magnet. This used a motorized probe station containing two planes of 30 3D Hall probes which were read out automatically. This system was capable of measuring a high density of data points over a large volume, but was unable to access all regions inside the RICH1 shield. For this purpose an additional series of measurements was taken by the author in the RICH1 region using simple Hall probes mounted in an adjustable structure. This series of measurements recorded the field vectors in the region of the HPD plane, checked the symmetry of the field in the HPD region and obtained an initial estimate of the field integral $\mathbf{B}_{trig}$.

4.6.1 The Trigger Field

The automated measurements were taken using two parallel planar arrays of 3D Hall probes, mounted on a mechanical structure that allowed automatic movement in the z direction, taking measurements every 10cm. Each of the 60 3D probes contains three Hall probes oriented at right angles to each other. The translations in x are accomplished by a manual movement of the track along which the probes travel, the translations in y by manually raising or lowering the probe plane above this track. At each step in the z direction the automatic system records the voltage read out from each of the probes and sends it to a PC. The coordinates of the points at which the field is measured, rotation corrections for each probe and the conversion for voltage to field are calculated offline.

The results obtained for the RICH1 region are shown in Figures 4.22 and 4.23. A simple numerical integration indicates that the integral field is approximately

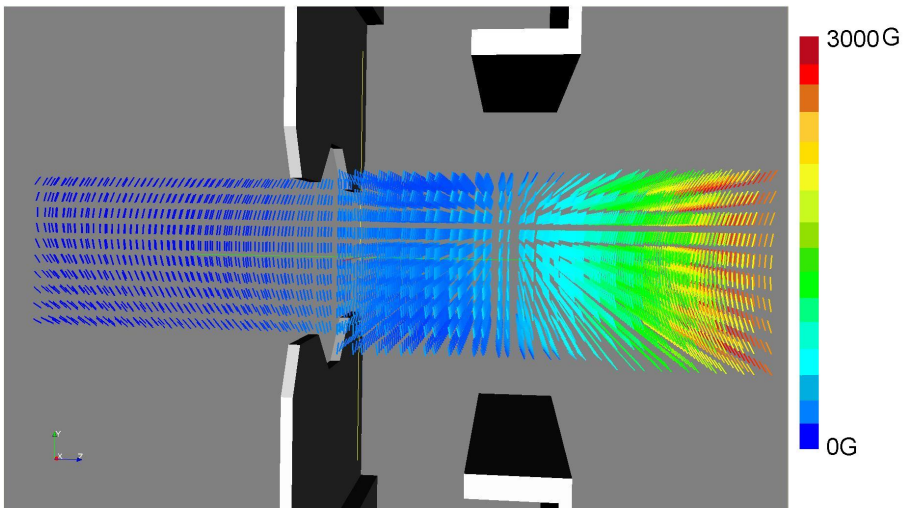

Figure 4.22: Results of the automatic mapping in the RICH1 region. Showing 3D field vectors between the halves of the RICH1 shield.

112kGcm: 20% less than the 138kGcm predicted by the model. It does however show that the field shape is as predicted.

Owing to the inability of the automatic machine to access the HPD region, manual measurements had to be made using a different set of Hall probes, designed for low field measurements. These same probes were used to take cross check measurements along the beamline, for comparison with the integral that was used to calculate the effectiveness of the shield models. The integral field measured by the manual probe is 10% higher than the integral measured by the automatic probes. This is readily seen in Figure 4.23 and is probably due either to the poor precision of positioning the manual probes with respect to the shielding, or to the effect of the large fields on the probes' readout electronics, which were not designed to operate in such conditions. As the manual probes were not designed to operate in these conditions it is assumed that the uncertainty on the measurements made along the beamline is large and the automatic probes provide a much more accurate measurement of the field in this region.

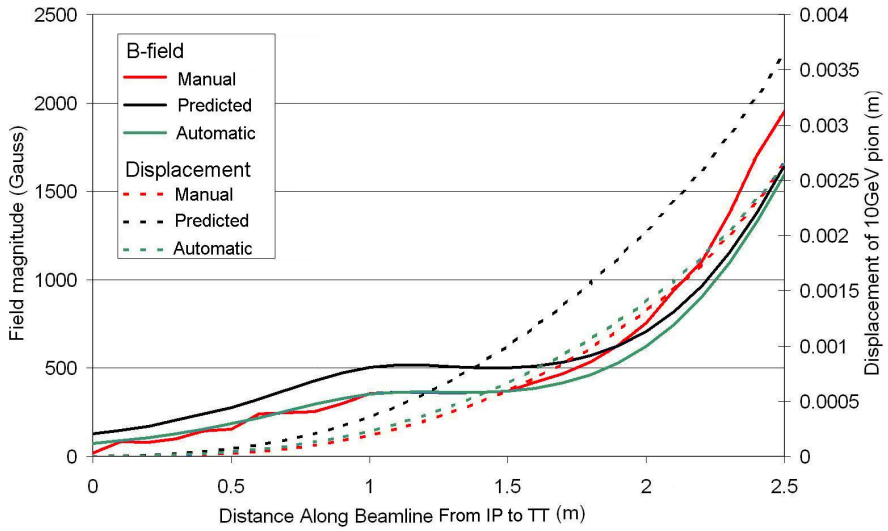

Figure 4.23: The field magnitude measured along the beamline from the interaction point to the TT. The three full-line curves are for manual, automatic and predicted fields. Also shown are the corresponding deflections for a 10GeV pion in the horizontal plane, indicative of the bending power that is required for the tracking trigger.

4.6.2 The HPD Region

The primary reason that manual Hall probes were used in addition to the automated system was the concern that the probes in the automated system were not calibrated for the low fields in the HPD region (of the order 30G). The system was calibrated for a field of 15,000G (1.5Tesla) as found at the centre of the magnet. The limited time the automatic probe system was available precluded the disassembly of the measurement plane and the re-calibration of the 60 probes, so as a precaution the manual measurements were taken. In addition, the volume in which the HPDs are to be mounted is confined by the shield walls meaning the useful movement of the automatic probes would be small, and adjusting their position would be difficult. The manual probes were the same as those used to characterise the field applied to the HPDs in the distortion experiments described in Section 4.1.

An adjustable frame was used to hold the probes in position and provide the stability required for a measurement to be taken. It could be set to the desired plane and the probes inserted in a series of 10cm-separated holes that held them in a specific

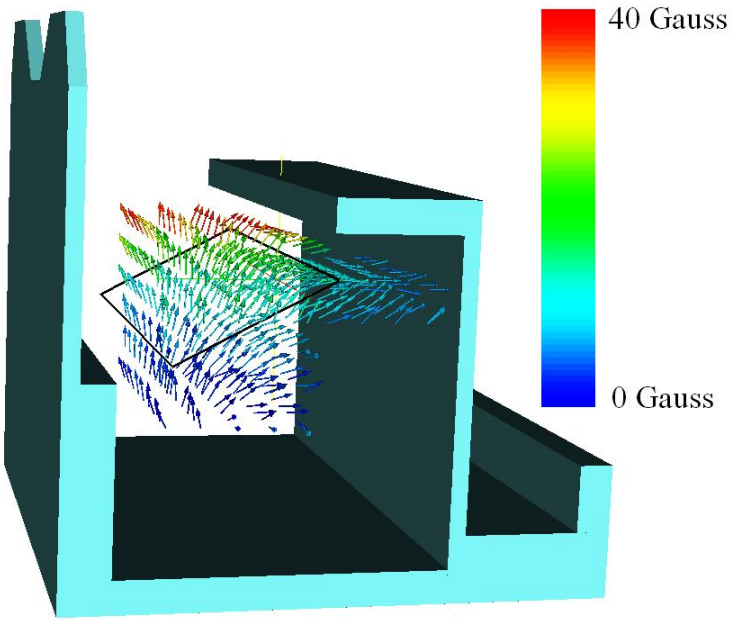

Figure 4.24: The field vectors around the HPD plane and under the internal shelf.

position. A series of measurements were taken in the bottom half of the shield, and the majority were taken only in the positive x quadrant. Several measurements at negative x were taken to verify the symmetry of the field. A single Hall probe was used to take separate $\mathbf{B}_x$ $\mathbf{B}_y$ and $\mathbf{B}_z$ measurements that were then combined into a vector. The accuracy of the manual probes in fields below 50G was $\pm$2G and the accuracy of the positioning in the frame was $\pm$5mm at the least stable point. However in the higher field regions the accuracy of the manual probe could not be guaranteed as it was possible for the field to have an effect on the probe readout unit.

These measurements of the field strength in the x, y and z coordinates were taken in a three dimensional grid of points throughout the volume around the HPD plane. This comprised six planes of nine by five points. These measurements around the HPD region, shown in Figure 4.24, were taken to ensure that there were no unexpected regions of high field close to the HPD plane. The results preclude the presence of regions of very high fields just beyond the HPD plane that could have been drawn in by the mumetal shields. They also inform a decision on whether it would be possible to move the HPD plane, in the event that the layout of the readout electronics or mounting mechanics needed to be significantly modified.

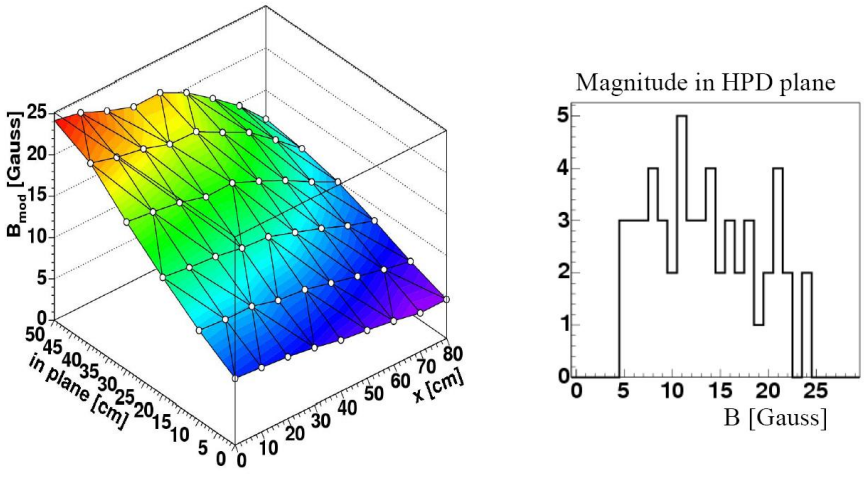

Figure 4.25: (Left) A map of the field magnitude on one half of the HPD plane, symmetry about $x = 0$ was verified. (Right) A histogram of the field values. There is no field magnitude over 25G.

$\mathbf{B}_x$, $\mathbf{B}_y$ and $\mathbf{B}_z$ measurements were taken in the region close to the internal shelf to investigate concerns about saturation. These were made on two planes of nine by six points. Results from these, also shown in Figure 4.24, indicate that the likelihood of saturation in the iron allowing field to be drawn out by the mumetal shields is smaller than predicted by the FEA. If saturation was occurring in the side plates in this region (caused by field from the shelf moving to the sides) hotspots would be seen close to the sides. As these do not occur it is unlikely that the presence of a small amount of mumetal will pull sufficient field into this area to cause the mumetal to saturate.

Measurements in the HPD photocathode plane were taken; along the axis of, and transverse to, the HPD orientation. A 3D magnitude probe was also used as an additional cross check. The measurements again used the adjustable frame to locate a six by nine array. These results are consistent with the previous measurements in the coordinate system of the experiment and are shown in Figure 4.25. They show that the field at the HPD plane is lower than predicted, especially in the y direction, and is significantly lower than the 30G in which mumetal-shielded HPDs have been successfully operated.

The three sets of measurements taken were all in one quadrant of the HPD volume. Due to the symmetry of the shield it was assumed that these measurements would

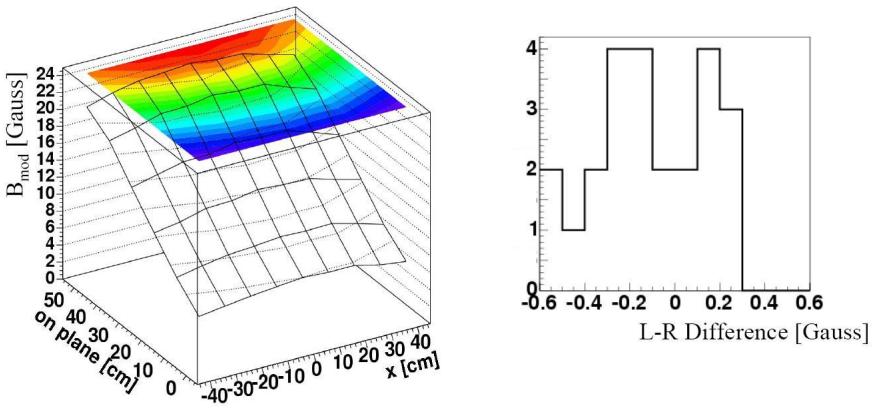

Figure 4.26: Results of the two symmetry measurements. (Left) A map of the field on the HPD plane, showing the symmetric pattern of the field. (Right) A histogram of the field difference at the symmetric points, showing no asymmetry greater than 0.6G.

be valid for all four quadrants. Checks of this symmetry were undertaken in the x direction. The adjustable frame was set in the middle of the box, within the HPD plane, and a series of measurements taken. As Figure 4.26 shows, they are consistent with symmetry.

4.6.3 Comparison with FEA

As described previously the FEA was used primarily to inform design decisions rather than to predict precise values. The success of the FEA should be judged on its ability to inform the optimisation of the shielding. Critical to this was the ability to give information on the field directions and the way the field strength changed as the shield's configuration was altered. However the final version of the model does provide predictions. In general terms the field direction has been predicted very accurately in the RICH1 region (as can be seen in Figure 4.27 & 4.28).

Overall the field values are about 10-20% lower than the predictions. The discrepancy is assumed to reside mainly in the inherent inaccuracies of the FEA model which could be exacerbated due to the (unknown) distribution of iron in the reinforced concrete of the cavern that is very close to the shields, or due to the iron of

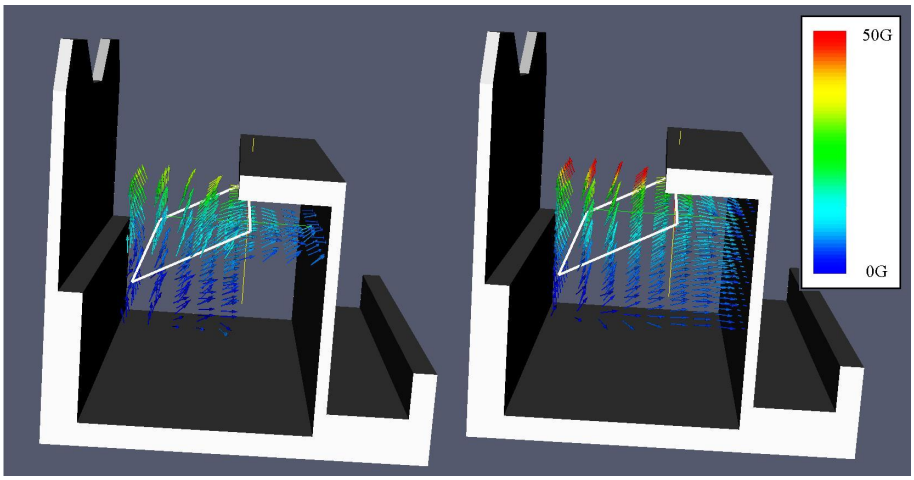

Figure 4.27: Comparison of **B**-field vectors between measurement (Left) and FEA (Right) in the HPD region.

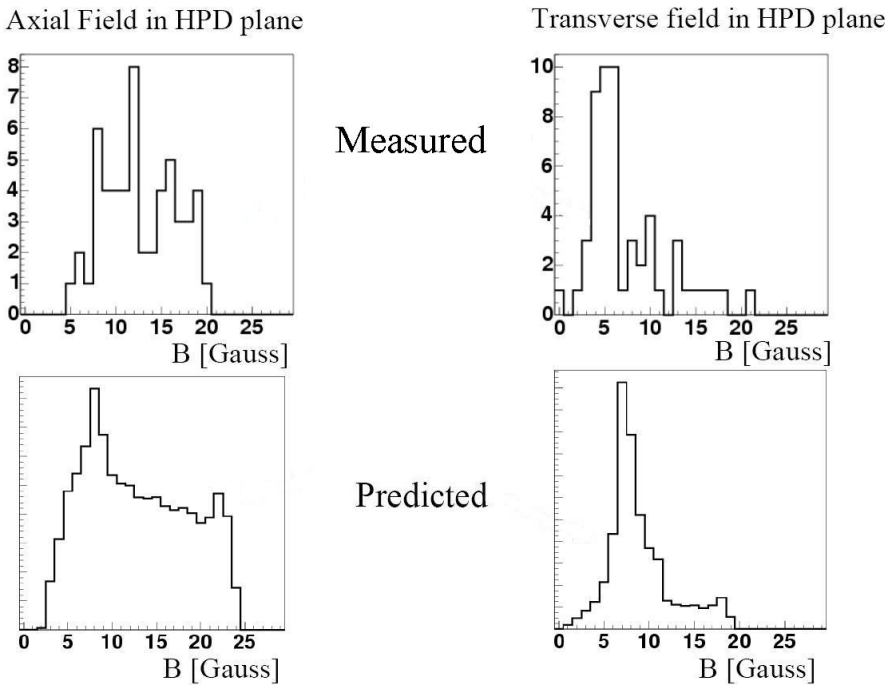

Figure 4.28: Histograms showing the field strength in the axial and transverse directions in the HPD plane for both measurements and FEA. These plots show that both transverse and axial predictions were 10-20% high.

the muon filters that was not included in the model. It is highly unlikely that there is a significant contribution to this discrepancy from the measurements in the HPD region with the manual probes, or the automatic measurements of of the field along the beamline.

4.6.4 Measurements with Cylindrical Shields in the RICH1 Shield

The initial measurements described in the previous sections demonstrated that the field was at a level compatible with shielded HPD operation. A series of measurements was then carried out to demonstrate that mounting an array of such tubes inside the shield did not have an unexpected effect on the field levels the HPDs would experience.

An array of 22 mumetal cylinders was mounted at the appropriate position in the shield and the field magnitude was measured at points along the central axis of each cylinder. Two arrangements of cylinders were used. In the first the array was set to mimic the HPDs closest to the side plates, as there was still concern about field being drawn out of these plates. In the second, the array was arranged symmetrically about the $x = 0$ line.

Figure 4.29 shows the field measured at the photocathode plane within the mumetal cylinders and the mean reduction of the field within the cylinders. This leads to the conclusion that at no point will the HPDs suffer a field of greater than 10G, and the bodies of the HPDs will reside in a field far lower than that, due to the shielding effects of the cylinders.

4.6.5 Consequences for LHCb Performance

Trigger Field

The field in the trigger region is smaller than predicted, as shown in Figure 4.23, and the predictions were lower than the design goal of 150kGcm. The automatic field measurements are 19% lower than the predicted integral field, and 25% lower

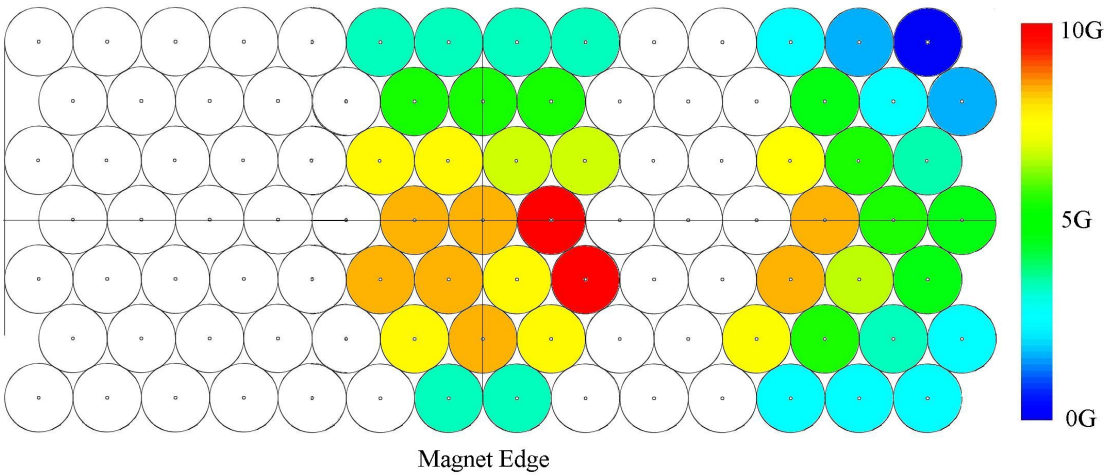

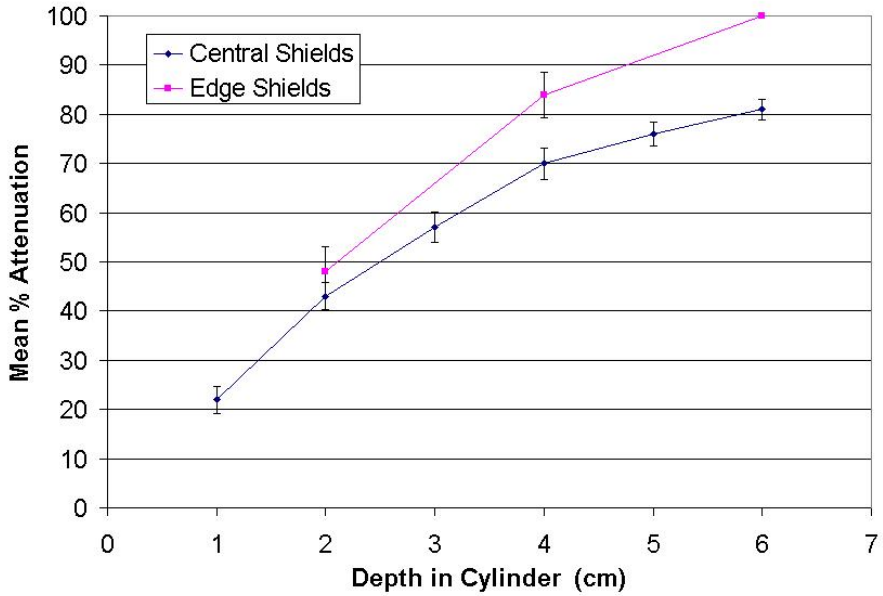

Figure 4.29: The field measured in the mumetal cylinders in the RICH1 shield. The photocathode plane is 4cm inside the cylinder.

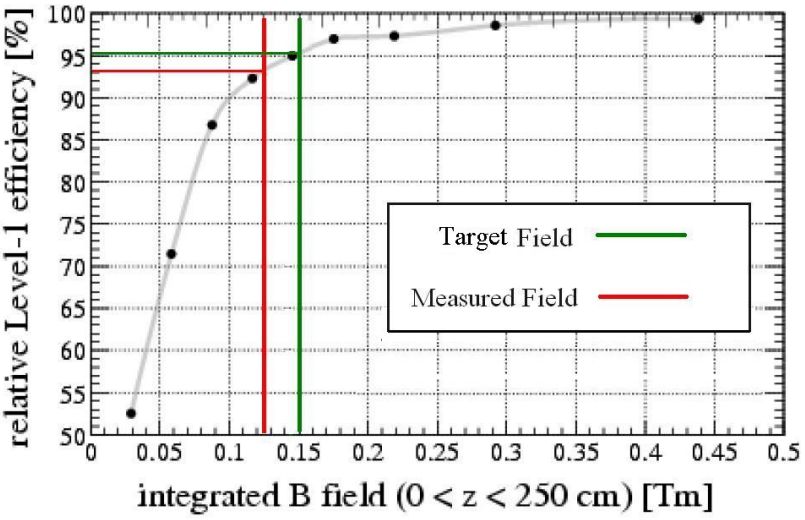

Figure 4.30: The effect of the integrated field on the efficiency of the Level-1 trigger. The difference between the target and the measured integral field results in a 2% loss in efficiency[71].

than the requested integral field. This smaller than expected bending power leads to a lower momentum resolution, resulting in a higher contribution of low momentum (and hence prone to multiple Coulomb scattering) tracks that provide false impact parameter estimates to the Level-1 trigger.

The trigger performance depends not only on the field integral (that gives the magnetic deflection) but also on the shape of the field. To examine this, numerical calculations of the flight of a 10GeV pion based on the predicted and measured fields were undertaken. As the particle is detected by the two-plane TT 250cm after the interaction point, two properties were calculated: the particle's displacement in the x direction, and its angular deflection.

The original goal for the RICH1 shield design was to provide a displacement of 3.4mm and this was converted to a (model dependent) field integral of 150kGcm. The field predicted by the FEA provided a 3.6mm displacement whilst the manual and automatic probe measurements both indicate a displacement of 2.6mm, despite their different integral fields. The predicted field provided an angular deflection of 4.1 mrad higher than the 4.0 mrad goal, whilst manual and automatic probe measurements indicate 3.8 and 3.4 mrad respectively. The Level-1 trigger algorithms are

continuously being improved and it is hoped to use information from the downstream tracking stations to recover from this potential loss in efficiency.

HPD Operation

Individual HPDs in mumetal shields have already been demonstrated to operate successfully in fields higher than those measured in the HPD region. Tests using a Helmholtz coil have shown that an HPD in a mumetal shield can operate within a field of 30G. The highest measured field on the proposed photo-cathode plane is 24G. The measurements with mumetal cylinders give a high level of confidence that the HPDs will operate and there is little danger of additional field being drawn into the region by the presence of the mumetal.

Software corrections to the HPD images will be required. The tubes tested individually in the Helmholtz coil displayed significant, but not performance-degrading, distortions at the expected field magnitude. As the field is non uniform across the HPD plane and the direction of the field will change with the magnet polarity, the distortions in the tubes will have to be regularly mapped. In RICH1 the magnetic distortions to the HPD electron optics will be monitored by a system mounted between the quartz window of the gas enclosure and the HPD box. This will be a flat frame containing a movable, low intensity laser (or mounted fibre delivering a laser) that will accurately position a spot of light on the photoplane. This will provide a reference to transform the distorted images recorded by the HPDs back to a map of hits on the HPDs. The expected precision of this system is sufficient to prevent any degradation of the Cherenkov angular resolution.

4.7 Magnetic Shield Summary

Using FEA, the RICH1 shield was optimised to protect the HPDs and to provide magnetic bending power for the Level-1 trigger. This optimisation was carried out within the strict mechanical limits of established neighbouring sub-detectors and their installation schedules. It required consideration of not only the magnetic, but also, operational and structural properties.

The shield was installed in the cavern and measured in the field of the LHCb dipole magnet, demonstrating that whilst the HPDs were well shielded, the field for the trigger was lower than the target. This could have a small detrimental effect on the trigger's efficiency, however it is not possible to quantify this until the trigger algorithm is optimised.

Additional measurements with the mumetal shields in place allow us to be confident of optimal HPD operation.

Chapter 5

HPD Readout Electronics

One of the most significant innovations in the LHCb HPD project is the pixel readout chip, LHCbPIX1[63], that is bump bonded directly to the silicon sensor and encapsulated within the HPD vacuum tube. This chip converts the response of the silicon sensor into a compressed binary signal that can be easily read out. Its low noise operation and the absence of cross-talk makes it one of the strengths of the HPD.

This chapter describes the operation of the LHCbPIX1 and details a series of measurements, carried out by the author, covering several of its characteristics. Section 5.1 describes the functionality of the chip and the methods used to study it. Section 5.2 details a study of the analogue response of the pixels to different sources of charge deposition in the silicon sensor. Section 5.3 discusses tests undertaken to examine the variation in the performance of the pixel chip over its surface, looking for dead areas and charge sharing effects. Section 5.4 describes the evolution of the response of a single pixel over the course of an LHC clock cycle and the changes caused by variations in the HPD operational parameters. Section 5.5 examines the chip's response to consecutive photoelectron hits in the same pixel and the consequences of any dead time for the operation of LHCb.

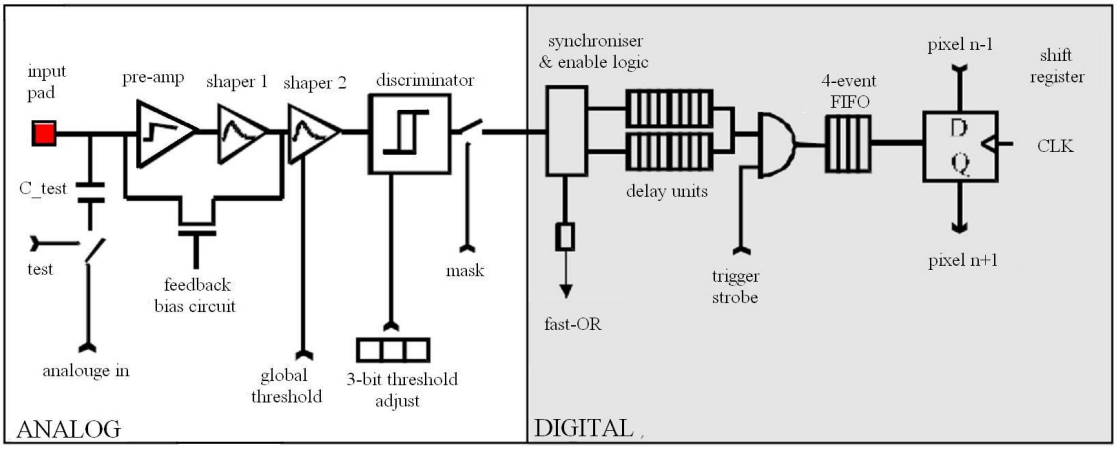

Figure 5.1: The layout of the components of a single pixel in the LHCbPIX1 readout chip, showing the analogue and digital halves of the system.

5.1 The LHCbPIX1 Chip and Test Equipment

The LHCbPIX1 and sensor 'assembly' is comprised of 256 by 32 pixels, each measuring 62.5μm by 500μm. It has two modes of operation, and so can be used for both the LHCb and ALICE[86] LHC experiments. The LHCb mode combines vertical blocks of eight pixels to form 500μm square super-pixels, and allows the HPD to be read out at the required rate of 40MHz, whereas in the ALICE mode each pixel is read out independently at a limited clock frequency. Each pixel has its own readout and control electronics, which are split into two sections (shown in Figure 5.1): an analogue front-end that amplifies, shapes and discriminates the signal from the sensor and a digital section that synchronises the read out to the global LHCb clock and processes the trigger signals. The pixel electronics have the following properties:

- Each pixel can be individually sent a pulse to simulate a hit on the sensor, regardless of whether the sensor is attached to the readout chip. This allows measurements to determine the appropriative threshold setting (VTH) for the chip, and a characterisation of the chip's performance.
- The signal from the sensor (or the test pulse) is processed by a pre-amplifier and two shaper units, giving it a standardised shape with a short (25ns duration) rise and fall time.
- The discriminator then compares the output of the shaper with the chip's

global threshold (VTH) and provides a digital signal to the synchroniser.

- At this point the chip provides the opportunity to mask the pixel. This is used as a diagnostic tool in Section 5.3, however its primary function is to block noisy pixels in the completed HPDs.

- The synchroniser takes the information from the discriminator and generates a binary signal, synchronised to the global clock, that can be read into the on-chip delay pipeline. This is used to buffer events pending a Level-0 trigger readout.

- The STROBE signal triggers the data in the final delay buffer to be read into the FIFO pipeline. The STROBE signal and its implications are discussed in more detail in Chapter 6. For measurements described in this chapter the STROBE is always in time with the clock signal and can be treated as a simple gate signal.

- The binary signal is then passed through a FIFO pipeline and into the chip's global register, from which a binary signal can be read out.

- Four of the sub-pixels on the chip are 'test pixels'. These provide probe points for the analogue response of the shaper, discriminator and synchroniser. These sub-pixels are situated across the bottom row of the chip, and are outside the photo-cathode image in nominal HPD operation.

In addition to initial measurements with the existing on-chip test pulse system, two novel methods were used to test the LHCbPIX1. In the first a laser was directed onto the surface of the silicon sensor, while in the second a low intensity LED was used to illuminate the photocathode of the HPD which was operated in a magnetic field. The purpose of the magnetic field was to deflect the photoelectrons so they fell on the test pixels.

A description of the apparatus used, and measurements taken by the author to study various attributes of the LHCbPIX1 chip follows.

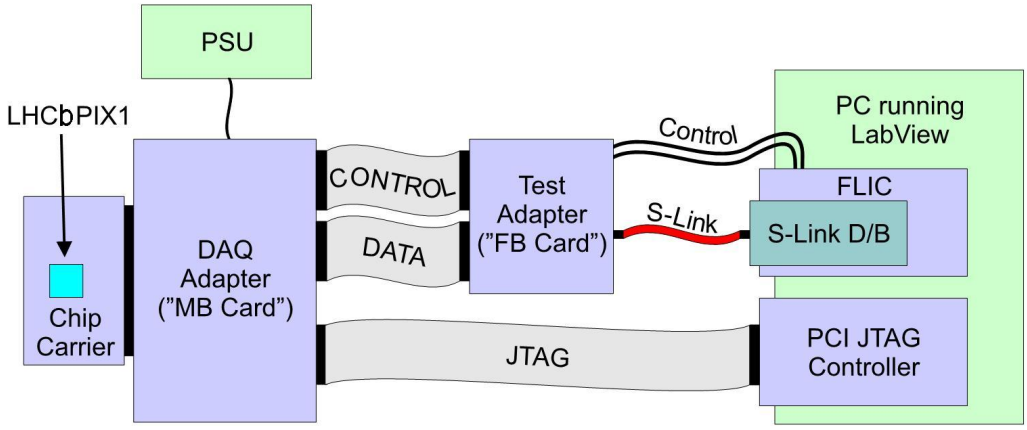

Figure 5.2: A schematic diagram of the HPD test readout system[77] showing the three main boards and the links between them.

5.1.1 Test Readout System

In the tests described in this chapter, the HPD is read out using the test system developed by the CERN electronics team and used by the HPD production test facilities[87] in Scotland. This comprises a replacement Level-0 board (the MB board) connected to a replacement Level-1 board, read through an S-Link[88] connection to a PCI-FLIC card. The MB is connected to a chip carrier board that can have either a zero insertion force socket to mount an HPD or a packaged assembly, or have an assembly or bare LHCbPIX1 chip wire bonded to it. The full system is shown in Figure 5.2. This system is controlled by a suite of LabVIEW[90] programs that are used to perform standard tests on the HPDs, including threshold finding and a continuous readout. The LabVIEW programs are also used to set (via JTAG[89]) the LHCbPIX1 parameters such as the length of the delay line, which pixels are masked and the amplitude of a test pulse.

In the measurements described in this chapter the test readout system is used primarily to measure the detection efficiency and to allow the HPD to operate normally whilst the analogue response of the pixel chip was studied.

5.1.2 Test Pulse Experiments

Initially the on-chip test pulse was used to examine the response of the LHCbPIX1 chip's analogue front-end to a charge equivalent to the detection of a photoelectron. The amplitude of the shaper response was used to define an appropriate level for the laser pulse that is described in the following section.

The electronic test circuitry was also used as part of a series of preliminary timing experiments. The chip's test pulse input was linked to a programmable pulse generator. This delivered a stepped voltage pulse into the capacitively coupled circuitry of the test board, providing two concurrent pulses to simulate the reception of photoelectrons in consecutive LHC bunch crossings. However, the results from these measurements were inconclusive and have been superceded by results from a complete HPD illuminated by an LED(presented in Section 5.5).

5.1.3 Laser Measurements

A near infra-red (1060nm) laser was used to inject charge directly into a silicon sensor without an HPD, with the laser pulse taking the place of a photoelectron. The sensor and its accompanying LHCbPIX1 chip were packaged in a ZIF socket and mounted on a test board. The laser pulse was triggered by a programmable pulse generator, and was sent down an optical fiber to a focussing unit. This was clamped in a $x-y-z$ micrometer adjustable mount, which enabled the laser to scan across individual pixels and charge to be deposited at precise locations, as shown in Figure 5.3.

The laser operated at a very low power and its output was too small to be measured by a standard electro-optical coupler. Consequently, the pixel chip itself had to be used to characterise the laser pulse, as it was the only sensor available with the necessary sensitivity. This characterisation was achieved by centring the focussing unit over a test pixel, sending controlled trigger pulses to the laser and measuring the output of the analogue shaper with an oscilloscope. The laser trigger signal was incrementally increased until the shaper response was similar to that produced by the standard 50mV test pulse. As a result of this it was not possible to deconvolve the timing response of the laser to its trigger signal and that of the assembly to the

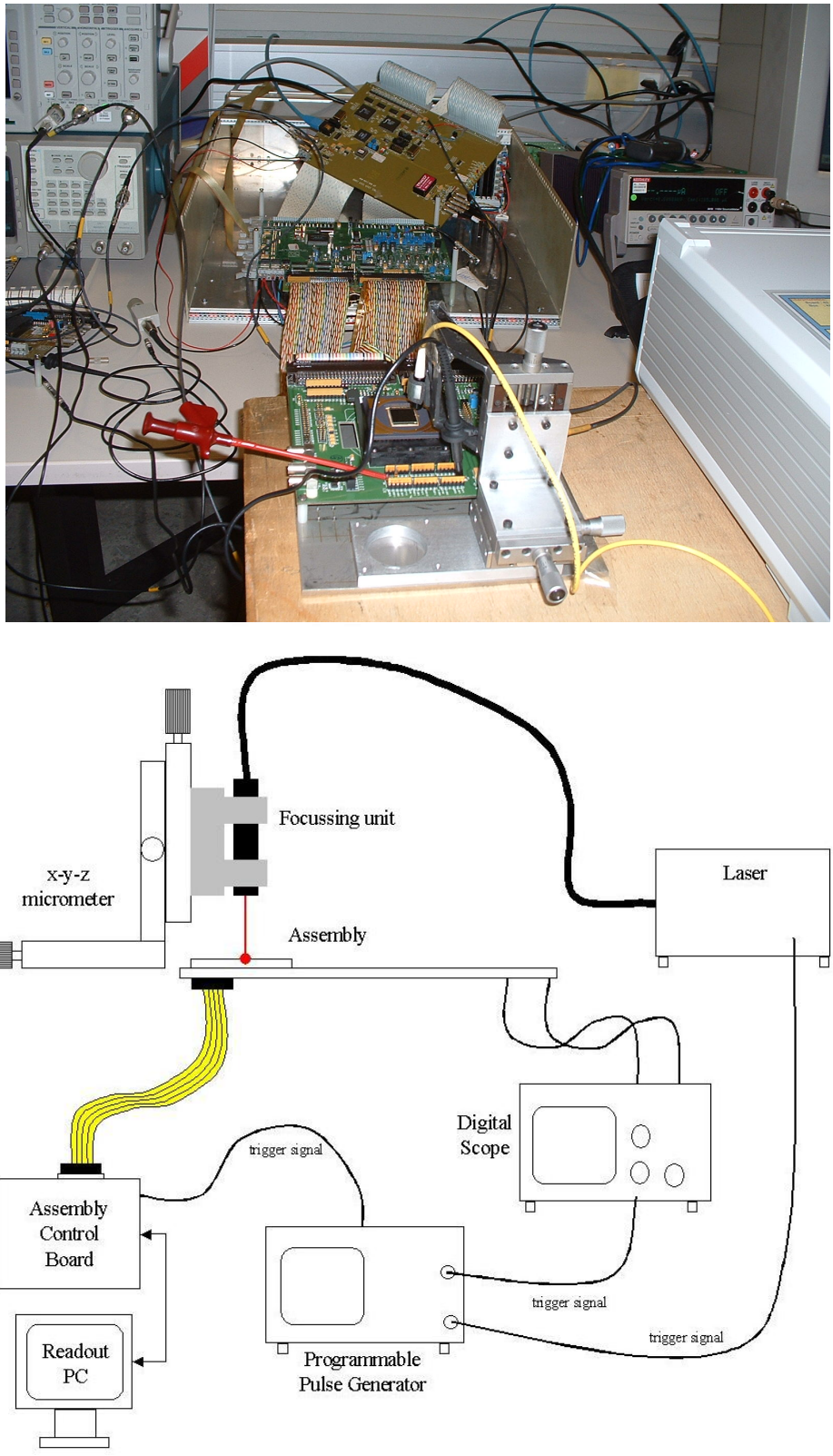

Figure 5.3: The laser/assembly test system, showing the pixel chip, laser unit and the xyz translation table.

laser pulse.

The laser measurements allow a precise determination of the charge sharing probability. The results are presented in Section 5.3.

5.1.4 HPD Front-End Measurements

In a standard HPD test rig it is not possible to access the analogue signals within the pixels readout circuitry. This is because there is no wire bond in the majority of cases and the chip is physically inaccessible, as it has been packaged inside a sealed vacuum tube of an HPD. The exceptions are the four test pixels, located on the bottom row of the sensor. Unfortunately these lie outside the image of the photocathode during normal HPD operation. To produce a photoelectron signal in these pixels, an HPD was placed in a distorting magnetic field (shown in Figure 5.4), deflecting the photoelectrons to the edge of the sensor, as described in Chapter 4.

To measure the analogue responses of the test pixels an HPD was mounted on a test board in a light-tight box. A Helmholtz coil was placed around it at 45° to achieve the maximum possible distortion of the electron optics. An LED source, tuned to ensure single photon pulses, was mounted on a remotely controlled x-y movement station enabling its light to be targeted onto the test pixels. The shaper and discriminator analogue signals were recorded and digitised using a digital oscilloscope and then sent to the readout PC over a TCP/IP link, under the control of LabVIEW. The HPD was read out continuously to check the position of the detected photons, but as the shaper and discriminator are not affected by any of the HPD's digital timing electronics, the scope data acquisition had to be triggered from the discriminator pulse and not from, or synchronised with, the HPD readout system.

These front-end measurements were used to:

- verify that the laser measurements modelled a photoelectron accurately;
- investigate the effect of changing the silicon bias and HPD high voltage on the analogue shaper response;

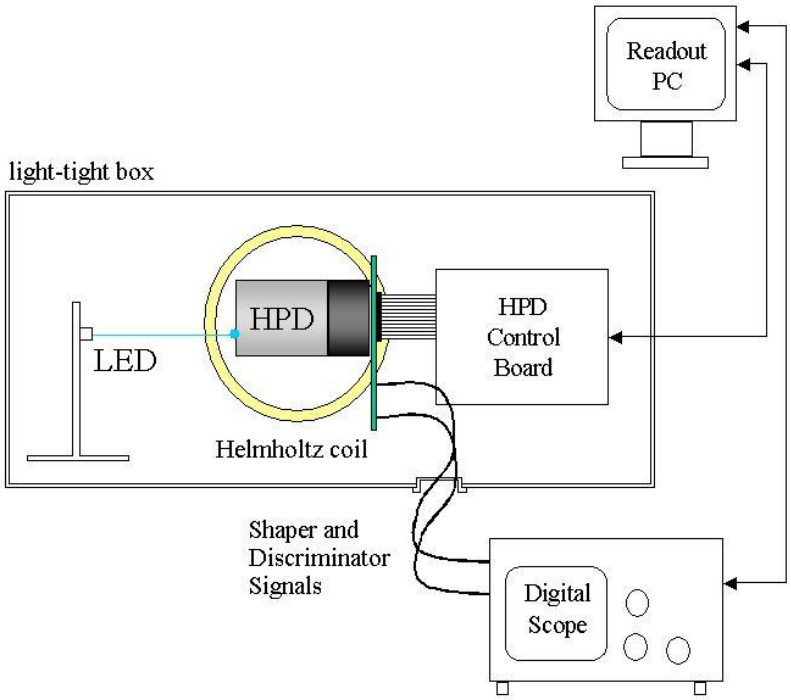

Figure 5.4: The equipment used to measure the analogue response of the pixel chip to a photoelectron in a realistic HPD environment. It shows the light source, HPD in a Helmholtz coil and the readout system.

- observe directly the effects of charge sharing, timewalk and consecutive hits on an operational HPD.

5.2 Analogue Pulse Shape Characterization

To confirm that the laser and test pulse studies were valid tests of the pixel chip, the response of the analogue shaper driven by the laser pulse was compared with that induced by the test pulse and by a real photoelectron generated within an HPD.

The HPD was set to the LHCb nominal settings for the characterisation measurements, with the silicon bias set to 80V and the high voltage to -20kV, as described in Chapter 3.

A running average smoothing algorithm was applied to the signals from the shaper to remove high frequency noise and improve the fitting performance. Each was fitted with a Gaussian curve allowing the amplitude and standard deviation of the signal to be easily measured (examples of the signal, smoothed signal and fitted results are overlayed in Figure 5.5). As not all the photoelectrons produced on the photocathode fell on the centre of the test pixel, the effect of charge sharing (described in Section 5.3) meant a wide variety of amplitudes and widths were recorded. This distribution made it necessary to take a mean value for comparison to the other test methods, rather than a single typical trace.

The analogue shaper response to the laser and test pulse were recorded directly by a digital oscilloscope. Both the laser and the test pulse have a far smaller spread of pulse widths and amplitudes than observed with the HPD measurement. Figure 5.6 shows the response for the laser and test pulse, and the mean response to a photoelectron in an HPD. This indicates the timing response of the laser pulse is a better simulation of a photoelectron in an HPD than the on-chip test pulse. This can be explained by the laser pulse producing charge in the sensor, as opposed to the test pulse injecting charge directly into the pre-amplifier and so not suffering delay and dispersion due to the time taken for the charge signal in the silicon sensor to develop.

From this we can conclude that a pulse from the laser will cause the assembly to

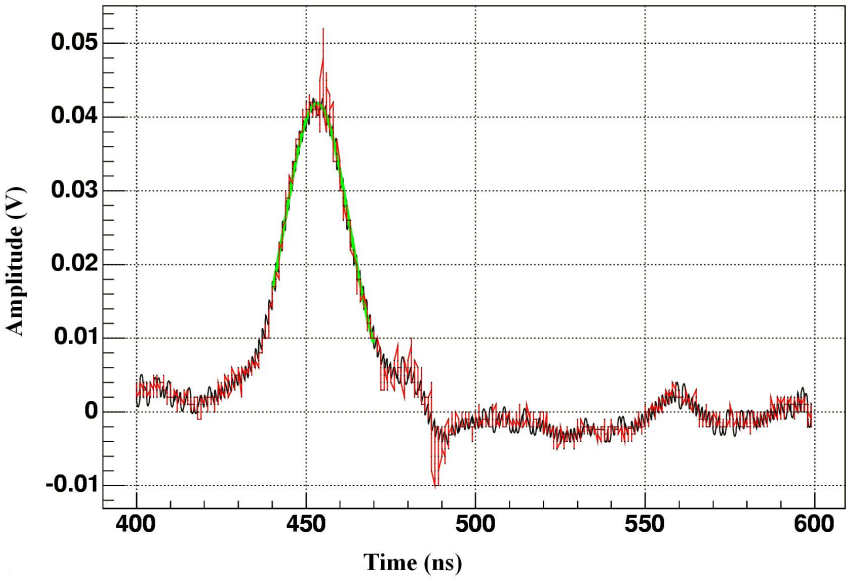

Figure 5.5: A shaper pulse recorded from the HPD test pixel, showing (red) the digitisation of the trace, (black) the smoothed curve produced by the running average and (green) the Gaussian fit to the smoothed curve.

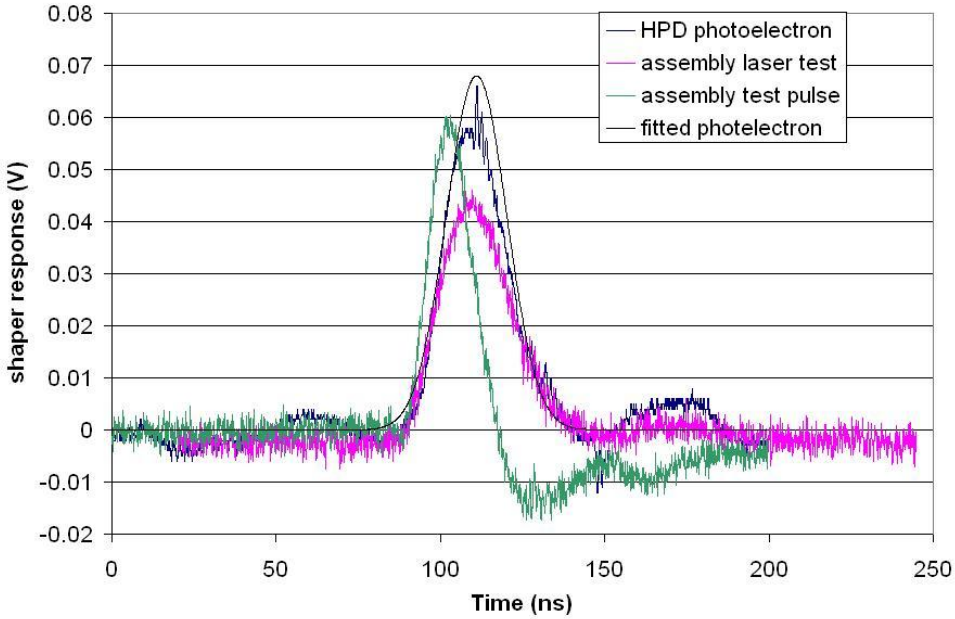

Figure 5.6: The response of the analogue shaper for the three systems used to test the pixel chip. From this it is possible to see that the laser tests provided a realistic injection of charge, and a good test of the response of the electronics. The test pulse has a steeper rising edge than that generated by the photoelectron and so is probably not totally realistic when used in timing studies.

respond in a very similar way to a photoelectron in an HPD. This measurement verifies that valid conclusions about the performance of the HPD can be drawn from the laser studies discussed in Section 5.3.

5.3 Charge Sharing Measurements

Charge sharing is a process by which the charge deposited by the same photoelectron is seen in two adjacent pixels. The sensor is made from a single silicon substrate and is only divided into pixels on its p-type side, where it is bump-bonded to the pixel chip. It is possible for a photoelectron, falling close to the boundary between two pixels, to deposit enough charge in each pixel (seen in Figure 5.7) to produce a signal that passes threshold in both pixels.

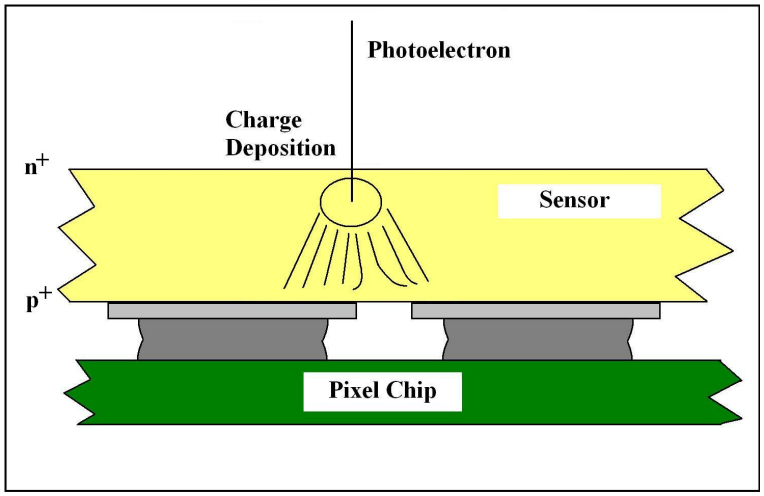

Figure 5.7: A schematic diagram showing the path of charge produced within the silicon sensor when an ionising track falls between two pixels, and the way in which this leads to charge sharing.

5.3.1 Laser Scans

To characterise the effect of charge sharing, the laser system was used to deposit charge repeatedly in specific locations on the sensor. The hit efficiency was measured and from this the charge sharing probability, as a function of impact position on the sensor, was calculated. These measurements were taken whilst scanning across the boundary between two pixels, clearly showing the shift in hit efficiency from one pixel to the other. Scans were repeated for three different threshold settings, to evaluate the change in the efficiencies between high and low thresholds. Three separate efficiency measurements were made for each point in the scans, one for the first pixel with all the others masked, one for the second and one for both pixels' efficiencies summed. When both pixels were measured, an efficiency of greater than 100% indicates the presence of charge sharing, with 1000 triggers returning greater than 1000 recorded hits. The chip was set to values of VTH (threshold) setting of 209, 214 and 219, a series of decreasing threshold settings, corresponding approximately to 3000, 2000 and 1000 electrons respectively[1]. These values were set with 219 being found to be the minimum level below which random noise is detected in some pixels on the chip and 209 the level beyond which some pixels lose efficiency.

Figure 5.8 shows the results of these measurements. As shown in Figure 5.8(a) a

[1]At 20kV a photoelectron produces approximately 5000 electrons.

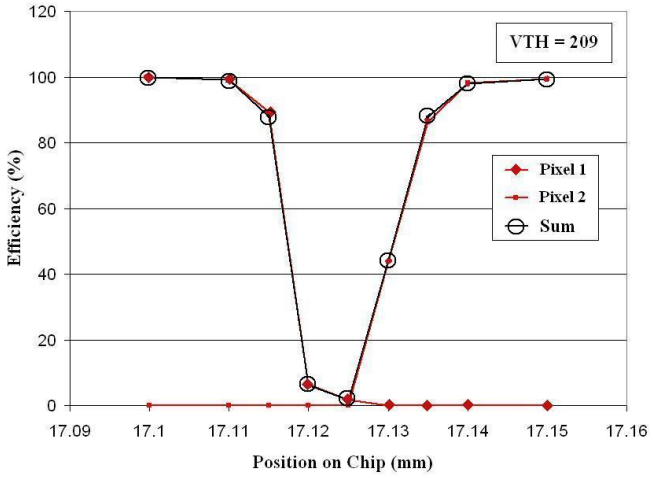

(a)

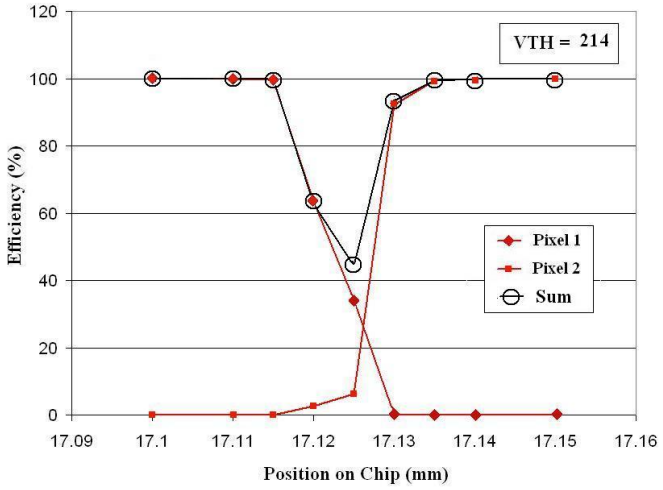

(b)

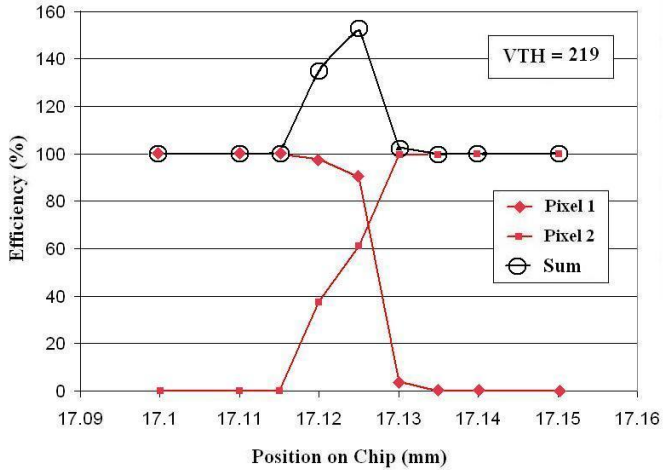

(c)

Figure 5.8: The efficiency of hit detection across a pixel boundary, showing the efficiency in the individual pixels and in both summed. (a) For a high threshold of VTH = 209, (b) for a nominal threshold of VTH = 214 (c) for a low threshold of VTH = 219.

high threshold setting leads to dead areas on the sensor, where the pixel chip will not be able to detect any hits at all. Figure 5.8(c) shows that a lower threshold setting leads to single photoelectron hits at the boundaries between pixels causing two hits to be registered. Having extra adjacent pixel hits is a lesser problem than missing hits altogether. The extra hit will either be subsumed (through the logical OR) into an LHCb super-pixel, or cause a neighbouring super-pixel to register. This has a minimal effect on the pattern recognition and ring finding as described in Section 3.4, provided that the hits are seen in the same timing window as the event that caused it. Not detecting photoelectrons that fall into a 10μm band (seen in Figure 5.8(a)) around each pixel would have a detrimental effect on the HPD's photoelectron detection efficiency and is the significantly worse option.

5.3.2 HPD results

Charge sharing is also seen in the data taken from the HPD analogue measurements. As photons from the LED result in photoelectrons that fall in a region larger than a single pixel, many of the photoelectrons produced fall in adjacent pixels and on the pixel boundaries. Figure 5.9 shows the distribution of shaper pulse amplitudes. The lower amplitude pulses are due to a band in and around the pixel where charge sharing occurs. The further from the edge of the pixel the photoelectron strikes, the larger the amplitude, until it reaches the maximum. However it is difficult to make a quantitative analysis based on these data as the distribution of the LED photons within the spot is unknown. It is unclear whether the photons fall in a Gaussian distribution about a midpoint, or as seems more probable from Figure 5.9, there is a central bright point surrounded by a flat halo. The main conclusion from Figure 5.9 is that it confirms the presence of low amplitude photoelectron hits, and so indicates the presence of charge sharing.

5.4 Timewalk Measurement

The effect of a smaller amplitude shaper pulse taking longer to reach and pass a threshold level is referred to as timewalk. It is of concern as it can cause delayed hits. These can be lost from the LHC bunch crossing to which they belong and

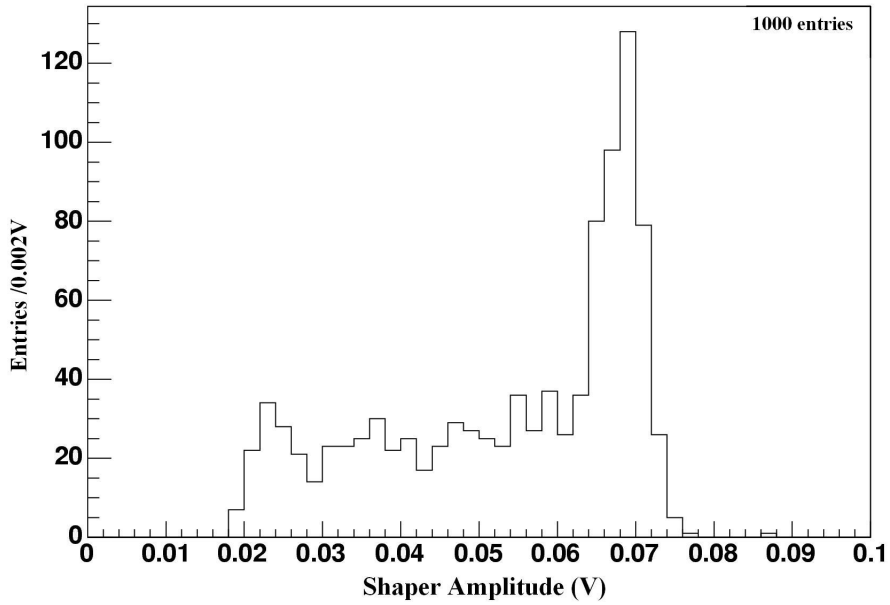

Figure 5.9: A histogram showing the spread of the amplitude of the shaper output in the HPD measurements.

be triggered by the STROBE in the subsequent bunch crossing. Reduced height pulses are caused by charge sharing, which could lead to pixel boundaries in an HPD regularly registering hits in later bunch crossings. This would cause more problems for the pattern recognition software than additional adjacent hits in the correct timing window.

To observe the effect of timewalk, the correlation between the height of a shaper pulse and the delay in the discriminator with respect to the start of the shaper pulse was recorded. Data were taken with a range of HPD high voltage settings (Figure 5.10) and with different silicon sensor bias (Figure 5.11). In these measurements, the delay offset has an arbitrary value set by the timing of the electronics on the test read-out boards and the lengths of the cables used to route the signal out of the light-tight enclosure.

Figure 5.10 shows the reduction in the peak height of the shaper as the high voltage controlling the acceleration of photoelectrons is reduced, and the energy of the photoelectrons falls. There is no effect of this reduced acceleration voltage on the timing of the discriminator, beyond that expected by the effect of timewalk itself.

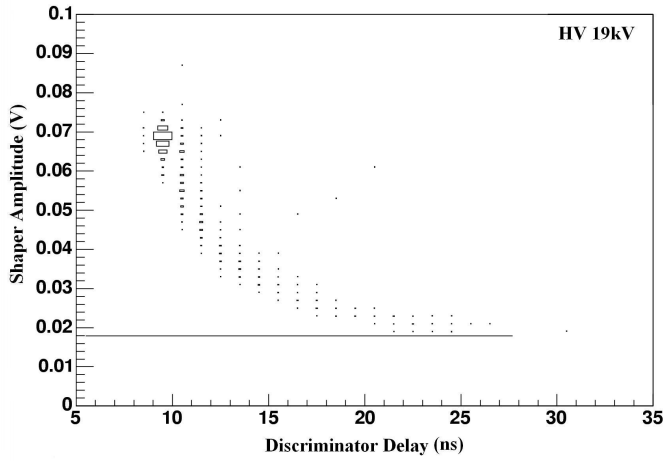

(a)

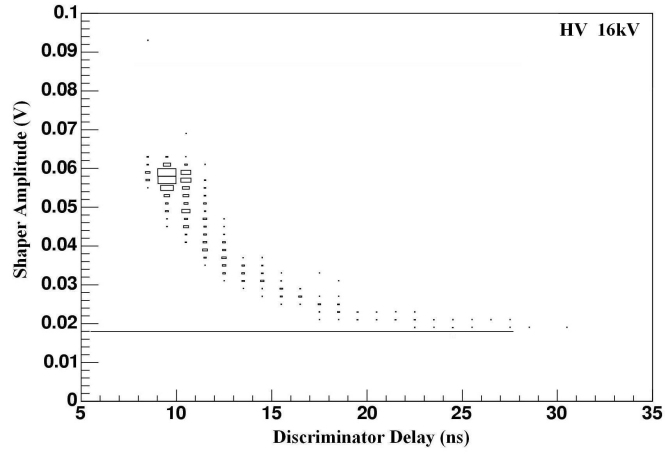

(b)

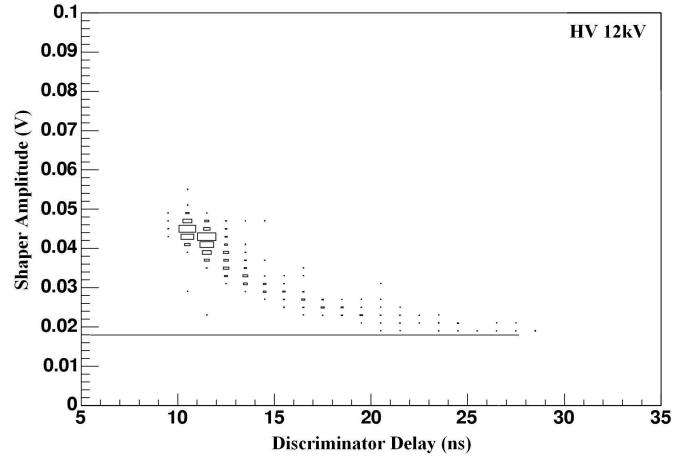

(c)

Figure 5.10: The correlation between the amplitude of the shaper pulse and the delay before the discriminator triggers, shown for (a) HPD operation at -19.6kV, (b) HPD high voltage reduced to -16kV and (c) HPD high voltage reduced to -12kV. The threshold is equivalent to 0.018V and is marked with a horizontal line.

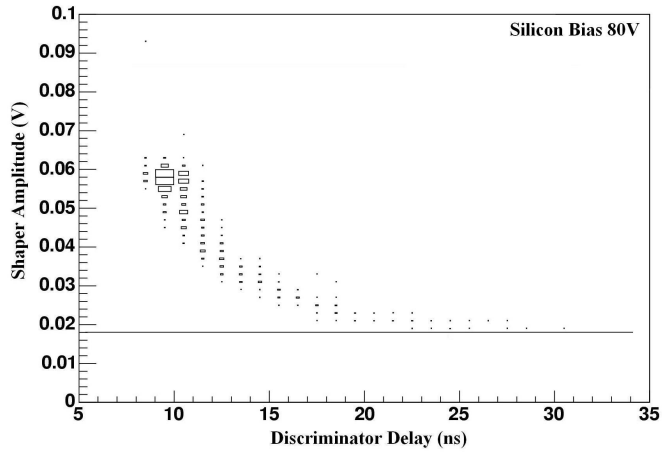

(a)

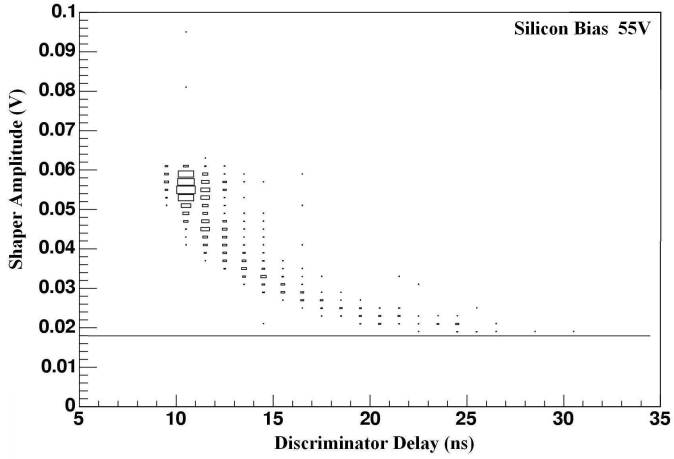

(b)

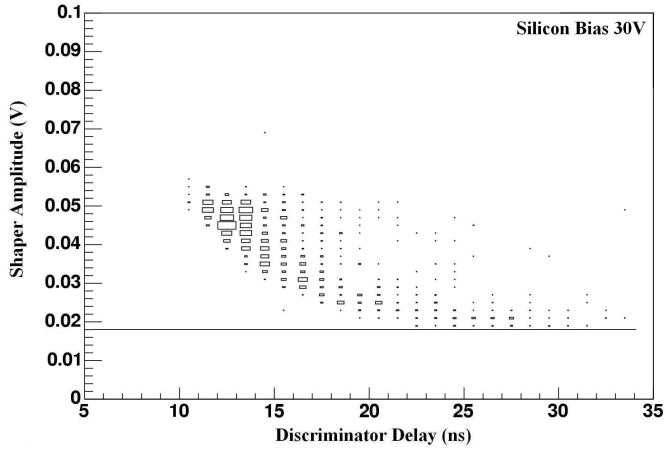

(c)

Figure 5.11: The correlation between the amplitude of the shaper pulse and the delay before the discriminator triggers, shown for (a) nominal silicon bias of 80V, (b) the silicon bias reduced to 70% and (c) the silicon bias reduced to 40%. The threshold is equivalent to 0.018V and is marked with a horizontal line.

A reduction in acceleration voltage does reduce the range of thresholds that can be used as higher threshold setting will cause a significant numbers of hits to be missed.

Figure 5.11 demonstrates that reducing the silicon bias increases the spread in delay of the discriminator response and decreases the amplitude of the shaper. This is due to a smaller bias driving the charge more slowly across the silicon substrate of the sensor. This effect delays the discrimination, even affecting some large amplitude pulses. It is expected that at the 40% (Figure 5.11(c)) point the silicon ceases to be fully depleted and the delays depend on where in the silicon the charge is deposited. This means that a photoelectron falling in the middle of a pixel, but depositing its charge close to the surface, would produce a peak after a long drift time through the undepleted silicon.

Both of these measurements with reduced acceleration voltage and silicon bias confirm that the HPD is operating in a manner that is consistent with the expected behaviour of the photoelectrons, the sensor and the readout system.

Despite the measurements of timewalk at less then nominal bias levels, Figure 5.12 shows that the lowest triggered pulses under nominal operating conditions have a delay from the largest shaper pulses of only 15ns, which is not enough to displace it into the next timing window. This means that in standard operation the HPD should be free of hits seen from previous clock cycles due to the combined charge sharing/timewalk effect. In these tests the threshold was set to a level of 0.018V, slightly below the signal released by 2000 electron-hole pairs produced in the silicon sensor.

5.5 Consecutive Hit Analysis

When a pixel is hit, the analogue signal produced by the shaper electronics takes approximately 50ns to decay to its baseline value. Thus it is possible that the discriminator for that pixel will not be ready to receive a hit in the next clock cycle. To examine this effect, measurements of two closely spaced hits were made with the HPD magnetic distortion setup.

The intensity of the LED supplying photons to the HPD was increased to en-

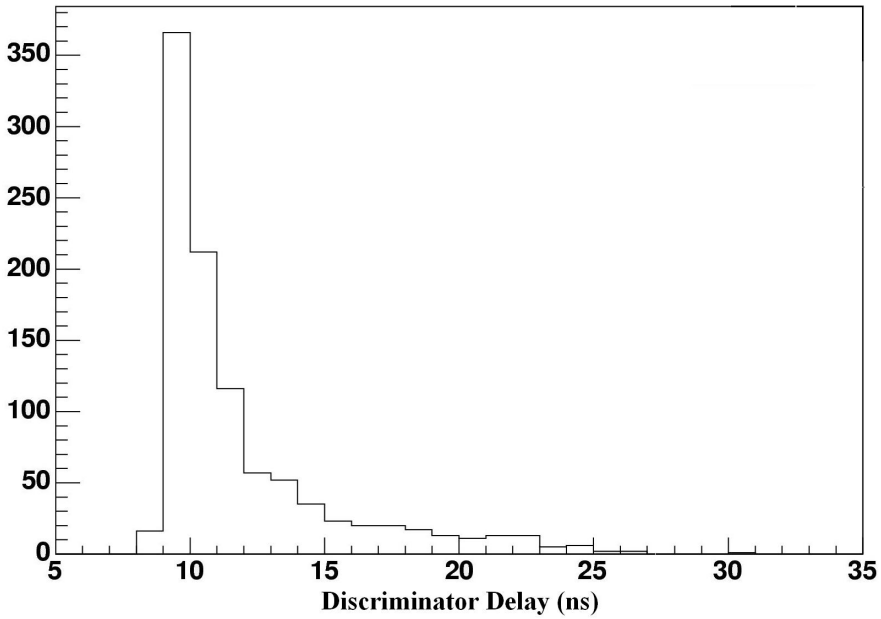

Figure 5.12: Histogram of the delay caused by timewalk in the operation of an HPD at nominal settings.

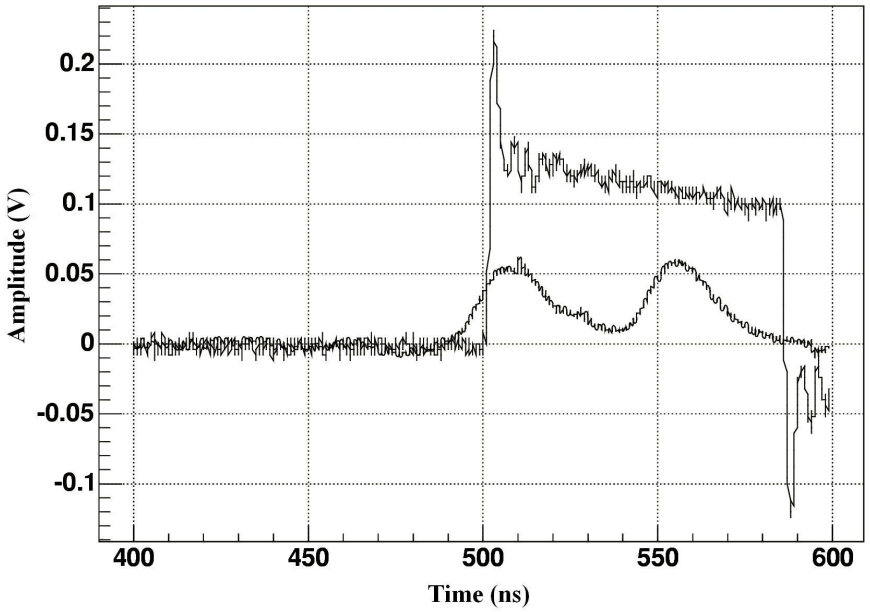

Figure 5.13: An oscilloscope trace showing two shaper pulses close together in time, resulting in a single discriminator pulse.

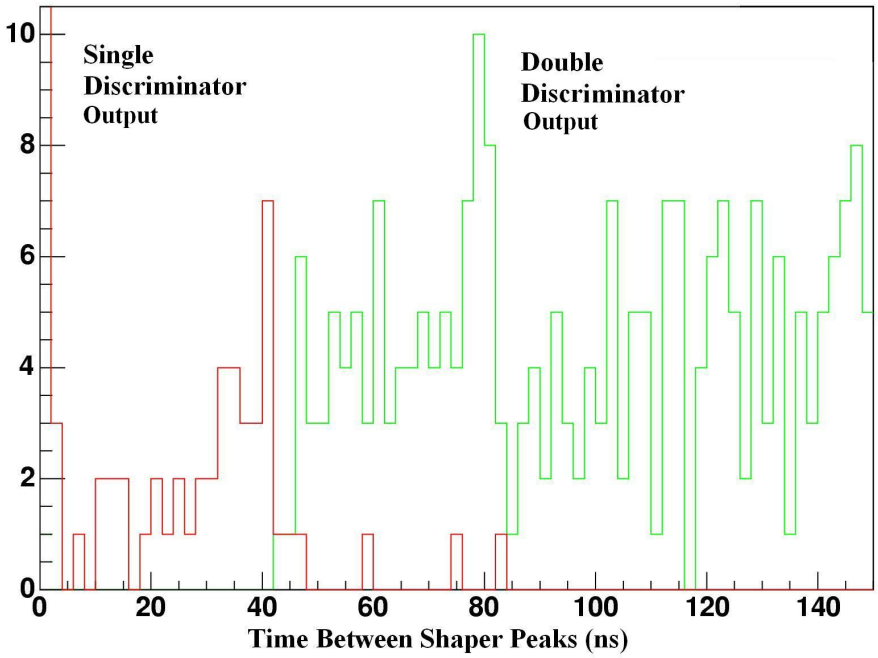

Figure 5.14: The number of discriminator outputs seen for a given separation of two shaper peaks at the input.

hance the probability of seeing photoelectron hits close together. 100,000 hits were recorded with the HPD nominal settings and the data were fit to select events with more than one shaper pulse within 300ns, as shown in Figure 5.13. The shaper pulses were then fit with Gaussians and the distance between the fit peaks recorded and separated into classes depending on the number of discriminator triggers present, as shown in Figure 5.14. The red histogram shows the separation of peaks producing a single discriminator pulse and the green histogram shows the separation of pulses that produce two discriminator signals. The single discriminator response stops when the shaper peaks are separated by ∼40ns. This means that the HPD pixel will be unable to identify a second photoelectron arriving within 40ns of the previous hit. Consequently, the pixel will be inactive for the LHC clock cycle following a hit. However, the LHCb super pixel will fire normally if there is a hit on any one of the other seven sub-pixels within that super pixel. As the maximum occupancy of the sub-pixels is less than 1% it is unlikely that this dead time will prove a problem for the detector; however, it is an issue that would need careful attention if LHCb is upgraded to operate at a higher luminosity—and so higher occupancy—in the future. It may also have an impact in events that we were unable to reproduce in

this system (to avoid stressing the HPD) such as the large shaper pulses caused by ion feedback, in which an ionised residual gas ion strikes the photocathode, releasing a shower of photoelectrons that are accelerated onto the pixel chip.

Due to the limited time the HPD test setup was available it was not possible to repeat this high statistics measurement for different threshold settings. This would be a useful study to perform, given that the optimum threshold for individual pixels exhibits a small variation, as demonstrated in HPD tests performed by my colleague S. Jolly[77].

5.6 Summary of Measurements on the Pixel Chip

By using an HPD in a magnetic field and illuminating the photocathode with a precisely positioned light source, it was possible to steer the photoelectrons onto sensor pixels equipped with analogue readout. This allowed studies to be performed that were not possible using the on-chip test pulse, including a detailed measurement of the charge sharing, timewalk and consecutive hits in an operational HPD.

The laser measurements of charge sharing demonstrate the effect of the threshold on the dead areas around the pixels, and that it is possible to avoid these dead areas at the expense of recording secondary hits in adjacent pixels.

The HPD timewalk study characterised the effect of the HPD high voltage and silicon bias and suggests that the lower amplitude hits associated with charge sharing have a low probability of being seen in the following bunch crossing, and should not pose any problem to ring reconstruction in the RICH system.

The study of consecutive hits using the HPD identified the presence of dead time in the sub-pixels, but found that it is limited to a single 25ns clock cycle after the initial hit. It would be useful, now more HPDs are available, to repeat this study for a range of threshold settings, to ensure there is no risk of the dead time being longer for other pixels or at different thresholds.

Chapter 6

HPD Tests in a Charged Particle Beam

In 2004 a series of experiments was carried out with charged particle beams from the CERN Proton Synchrotron (PS) in the T9 test area. The purpose of the tests was to operate the HPDs in an environment similar to the final RICH detectors and to evaluate the performance of the prototype readout electronics systems. The T9 area was available for two, two week periods, one in October and one in November. The first was used to test the principal elements of the system, a single HPD, a Level-0 board and prototype Level-1 board. The second was used to test close-packed HPDs, read out using three separate Level-0 boards read by Level-1 boards running with an LHC compatible clock frequency of 40MHz.

The tests were carried out using a basic RICH system that provided Cherenkov light to be detected by the HPDs. The results were then analysed to determine whether the photon yield, the Cherenkov angle and its measured uncertainty were compatible with the expected values.

This chapter reports on the detail of the equipment used to take the data and the analysis of the photon yield seen in the HPDs. The overall analysis effort was coordinated by Mitesh Patel, the work at Imperial College on the photon yield was led by Ulrik Egede who provided the fitting model. The HPD timing corrections were performed jointly by Richard Hallam and the author, with the latter focussing more on the individual pixel timing. The calculations of the expected photoelectron

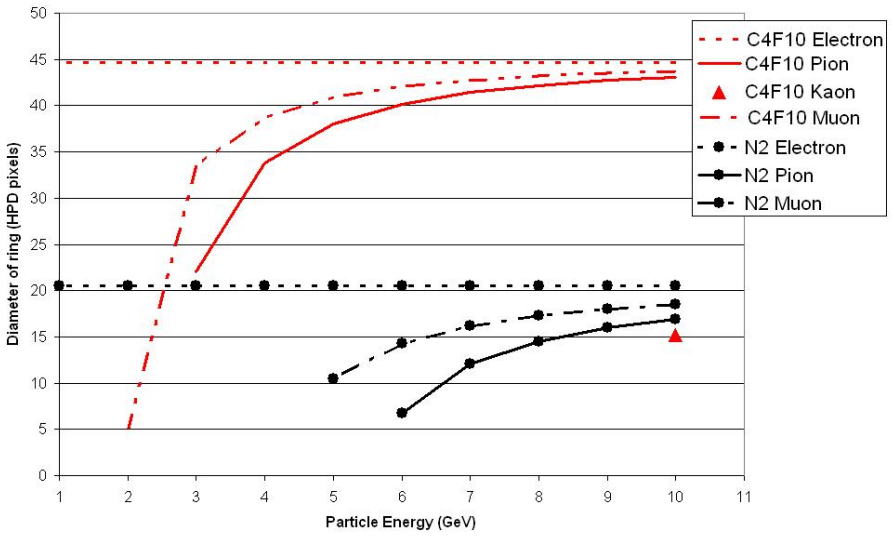

Figure 6.1: Predicted Cherenkov ring diameters using N_2 and C_4F_{10} radiators in the test RICH detector.

yield and the systematic error on the fitted yield presented here are the work of the author. The 'fake hit' analysis and the fits to the results to determine the parameters of the timing model used to inform the yield fit were the work of Tom Blake and Richard Hallam respectively.

6.1 Experimental Details

This section describes the equipment and experimental procedures used to carry out the tests.

6.1.1 The PS Beam

The T9 test area is provided with a 10GeV negative secondary beam, produced from the interactions of 24 GeV protons from the CERN PS in a target. The beam contains primarily pions and electrons although kaons, antiprotons and muons are present at the percent level. The diameters of the Cherenkov rings (measured in units of HPD pixels) are shown in Figure 6.1. At 10GeV the ring diameters of pions,

electrons and muons are similar, but kaons are just over threshold in C_4F_{10} and have a significantly smaller diameter. Antiprotons are below Cherenkov threshold.

A threshold Cherenkov counter is placed in the beam line and the pressure of its radiator gas can be set to allow the selection of heavy or light beam particles at the trigger level.

6.1.2 The Small Simple Box

The Small Simple Box (SSB) was designed to provide a realistic operating environment for the HPDs and their readout electronics. To this end it has the following features, as shown in Figure 6.2:

- A parabolic mirror of focal length 1016mm, similar to that of the spherical mirrors used in RICH1, was fixed to micrometer-screw mounts allowing precise angular adjustments to the mirror axis.
- A radiator path length consistent with RICH1. Combined with the tilt angle, this set the uncertainty in the reconstructed Cherenkov angle, due to the photon emission point of the SSB, to be approximately that of RICH1.
- A quartz window separating an N_2 environment to protect the HPDs. This is required to prevent moisture and dust particles in the atmosphere causing micro discharges on the HPDs' photocathodes which could result in damage. This window is also present in RICH1 and RICH2 so any unexpected transmission effects in these detectors should also be seen in the SSB.
- Mountings for three close-packed RICH2 HPD columns, although only part of each column could be illuminated by Cherenkov light. This means the SSB can be used for HPD column tests when there is no particle beam available.
- The ability to use N_2 or C_4F_{10} as radiator gasses. These produce different expected photon yields and ring diameters. The N_2 radiator produces photons that when projected through the SSB form a small ring that fits within the photocathode of one HPD. The C_4F_{10} radiator produces a much larger

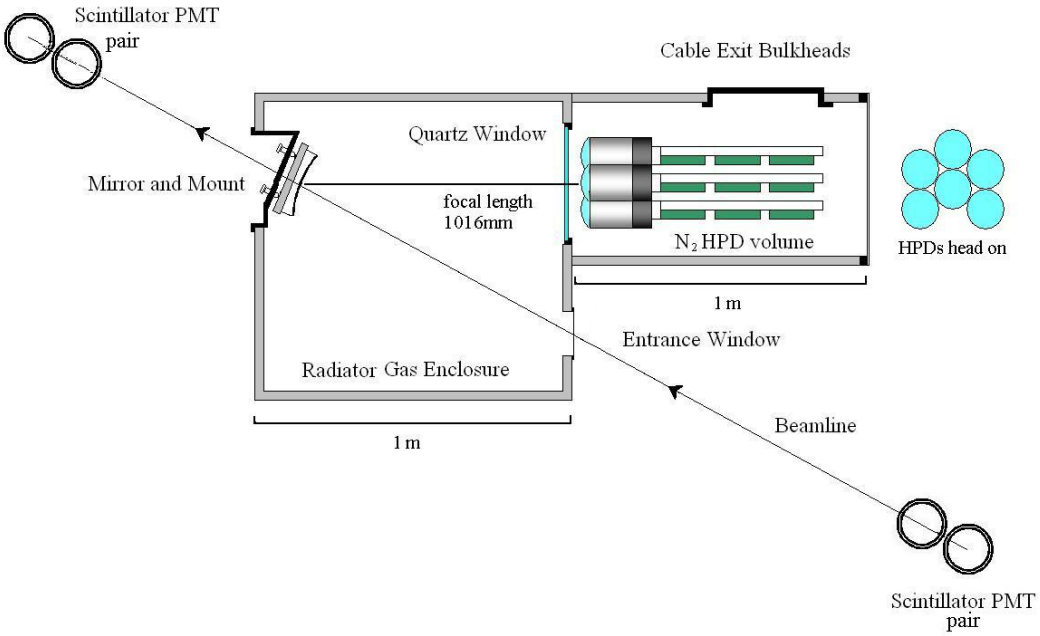

Figure 6.2: *Top*: A photograph showing the SSB aligned in the T9 test area. *Bottom*: A plan view of the SSB showing its design and experimental layout.

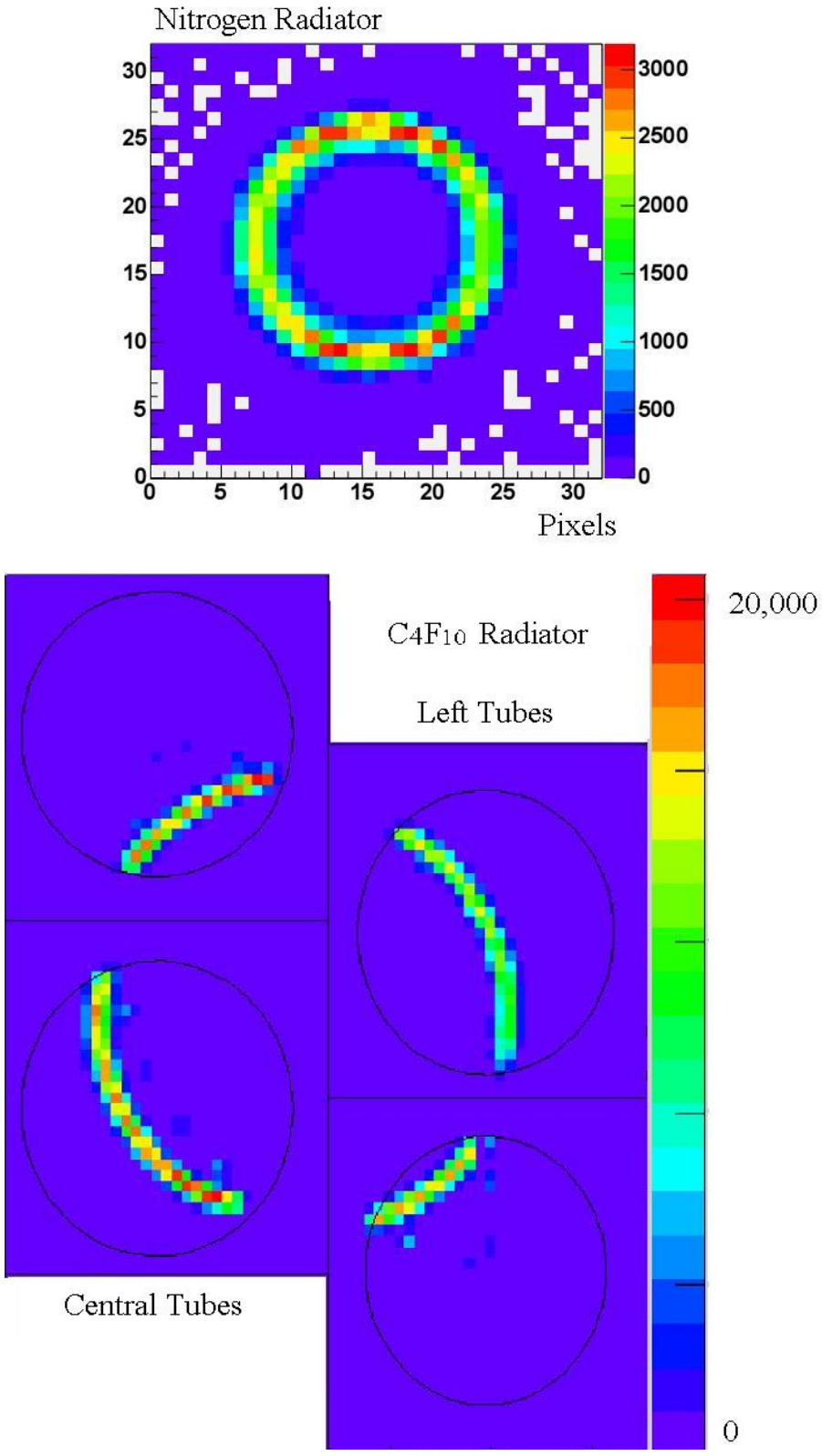

Figure 6.3: *Top*: The Cherenkov ring from the accumulated hits from many beam triggers in the N_2 radiator is contained in a single HPD. *Bottom*: The ring from the C_4F_{10} radiator spans four HPDs.

ring that can be positioned to cover three or four HPDs simultaneously. Typical rings accumulated from a large number of beam triggers and from both radiators are shown in Figure 6.3.

- A series of gas temperature and pressure monitors to record the characteristics of the radiator medium, from which the refractive index was determined. The system included a measurement of the speed of sound in the gas, from which the density could be precisely determined. This was a prototype of the monitoring system to be used in the LHCb RICH detectors.

- A thin, removable, aluminium entrance window for the particles, that maintains light tightness without producing excessive multiple scattering at the entrance to the radiator volume. It was removable so cross hairs could be installed in its place to allow the SSB to be aligned using a laser beam, directed along the line of the particle beam.

- Extensive efforts were made to ensure the light tightness of the SSB. This was important, not only to avoid background noise, but to avoid any risk of damaging the HPDs, which (at the time) comprised the entire stock of prototypes. The inside of the SSB was blackened,and the joints were filled with black epoxy. The door to the HPD enclosure had light-tight seals. The gas inlets and outlets were pigtailed to prevent scattered photons entering and the the entire apparatus was covered in a blackout cloth.

6.1.3 Trigger System and Alignment

The HPD trigger signal (the STROBE signal described in Chapter 5) was generated by a coincidence of 4 scintillators, indicating that a charged particle had traversed the system. These were arranged in two pairs, up and downstream of the SSB, as shown in Figure 6.2. Pairs of scintillators were used to reduce the chance of a cosmic ray, or other noise source, being in coincidence with an off-axis particle and causing a fake trigger.

The trigger system (shown in Figure 6.4) could be set to include a coincidence with the beam threshold Cherenkov counter. This is used to select or veto various particles in the beam. It consists of a CO_2 gas radiator, and a thin mirror to deflect the Cherenkov light perpendicular to the beamline, where it is detected with

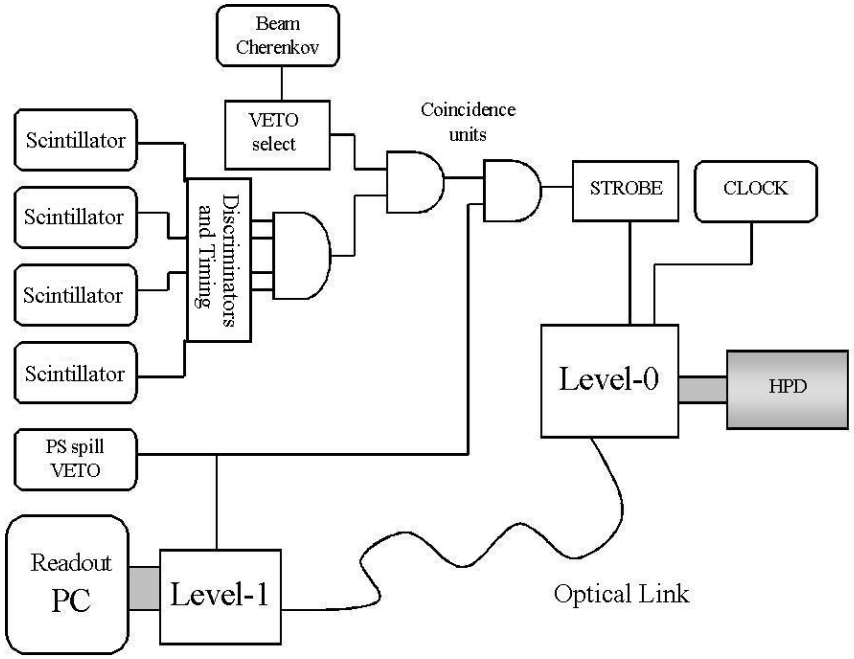

Figure 6.4: The trigger system, comprising beam scintillators and beam Cherenkov counter, and the schematic of the signal processing logic.

a photomultiplier. It is controlled by setting the pressure of the gas, such that only particles of the desired species were above threshold (or below if it is used as a VETO).

Signal pulses from the PMTs on the trigger scintillators were passed through NIM logic discriminators to give a standardized NIM signal (-14mA into 50Ω). These signals were then passed through delay units to allow the timing to be adjusted so that the pulses from a particular beam particle passing through all the scintillators were in coincidence.

Once the scintillator signals were in time, they were spatially aligned. Initially they were roughly positioned by directing a laser down the beamline. After this the scintillators' positions were fine tuned by moving them individually in steps to maximise the count rate in each scintillator, and then finally to maximise the full coincidence rate.

The SSB itself was then aligned to the beam and the scintillators. This was achieved by removing the mirror mount and marking the line between the centres of the two scintillator pairs with a laser. The mirror mount was then replaced, with a mark at

its centre and a cross hairs placed on the front window of the SSB. The SSB was moved until this and the centre of the mirror mount were aligned with the laser.

The mirror itself, fit to its mounting, could be tilted using the three micrometers. To position the projected Cherenkov ring in a particular position on the HPD plane, the SSB entrance window was removed again and the laser beam directed along the beamline. The mirror angle was adjusted incrementally until the reflected laser spot was centred on the required position in the HPD plane.

In a departure from previous HPD beam tests, particle tracking information was not recorded. Previously, silicon telescopes had been used to provide tracking and angular measurements for individual trigger beam particles, and were synchronised to the trigger system. It was decided that the read out delay introduced by the available silicon telescopes would reduce the rate of data taking to the point where it would no longer be a reasonable test of the 40MHz system. Further, the slow read out of the telescopes significantly reduced the quantity of data that could be accumulated. Whilst this has no bearing on the measurements reported here, it limits the precision with which the Cherenkov angle can be determined due to the finite beam divergence.

6.1.4 Single HPD Runs

The primary goals of the October 2004 run were to debug the system and demonstrate that the electronic and mechanical components were compatible and operational. These were achieved with the HPD and its flexible coupling connected to a Level-0 board, powered by a low voltage board and read out by a prototype Level-1 system. The high voltage (20kV) was supplied to the HPDs by an external commercial power supply rather than a prototype high voltage board as it was unavailable at the time of the first session.

With the system operational, data were recorded from the HPDs. N_2 was used as a radiator without the quartz window separating the HPDs from the radiator volume. This arrangement produced an easily identifiable Cherenkov ring on the HPD (an example of which is shown in Figure 6.3). A series of measurements were taken, including:

- A series of data sets varying the value of the HPD pixel chip threshold.
- A series of measurements examining the delay between the STROBE and the clock. The delay between the clock and the STROBE was altered partly by changing settings on the Level-0 board and partly by using a passive delay box in the trigger system.
- Data triggered by a random pulser, taken with and without the beam present, to quantify the background noise associated with the HPD operating in a realistic environment.

A major problem faced in this series of tests was ensuring the light tightness of the SSB. Despite the precautions described earlier in this chapter, a background level of photon counting was observed higher than any previously measured by the HPDs. The light tightness precautions were redoubled leading to a very small improvement. The problem was worse for the HPDs with photocathodes that are more sensitive to infra-red wavelengths. It was concluded that photons were escaping the optical fibers and the VICSEL[91] communication driver linking the Level-0 board to the Level-1 readout system. To solve this, covers were put over the VICSELs and the fibres to stop light from the electronics reaching the HPD photocathodes. Although this did not totally solve the problem it was reduced to an acceptable level.

6.1.5 Tests with a Close-Packed HPD Array

The progress made in the October run allowed for more extensive tests in the second session in November 2004. It utilised six close-packed HPDs mounted in pairs on three separate columns. The low voltage board provided power for the Level-0 board and the HPD silicon bias. A prototype of the final high voltage chain was used for the HPD, as shown in Figure 6.5. The quartz window was installed to separate the radiator gas from the dry nitrogen environment of the HPDs.

Several measurements were taken in this session, with more emphasis on systematic scans of parameters. Data were taken using C_4F_{10} and N_2 radiators.

- Initially the radiator gas used was N_2.

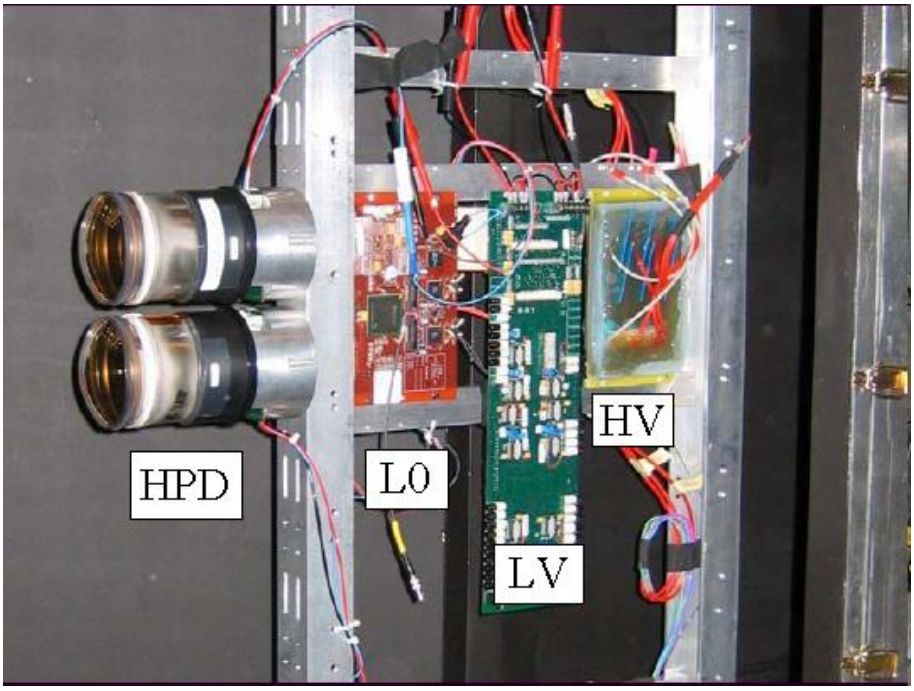

Figure 6.5: A photograph of the electronics chain mounted on a RICH2 column, showing the HPDs, a L0 board, a LV board and an HV board.

  - Individual data runs were taken with the Cherenkov ring centred in turn on each of the six HPDs. The data taken in these runs are described in Section 6.2, comparing the measured and predicted photon yields.
  - For each HPD separate data were recorded for pions and electrons using the threshold Cherenkov counter to select the appropriate particle species.
  - A threshold (VTH) scan was undertaken for selected HPDs to ensure that they were operating correctly in the test beam environment, and to compare with the laboratory measurements.

- The radiator gas was then changed to C_4F_{10}.
  - The mirror was positioned so the larger C_4F_{10} rings span three or four of the HPDs simultaneously. Five mirror positions were used.
  - Delay scans were repeated for each ring position using only the passive delay box. These data were used to study the different timing effects on each HPD and are described more fully in Section 6.2.
  - Data were then taken with random triggers with the beam on and off to characterise the background noise.

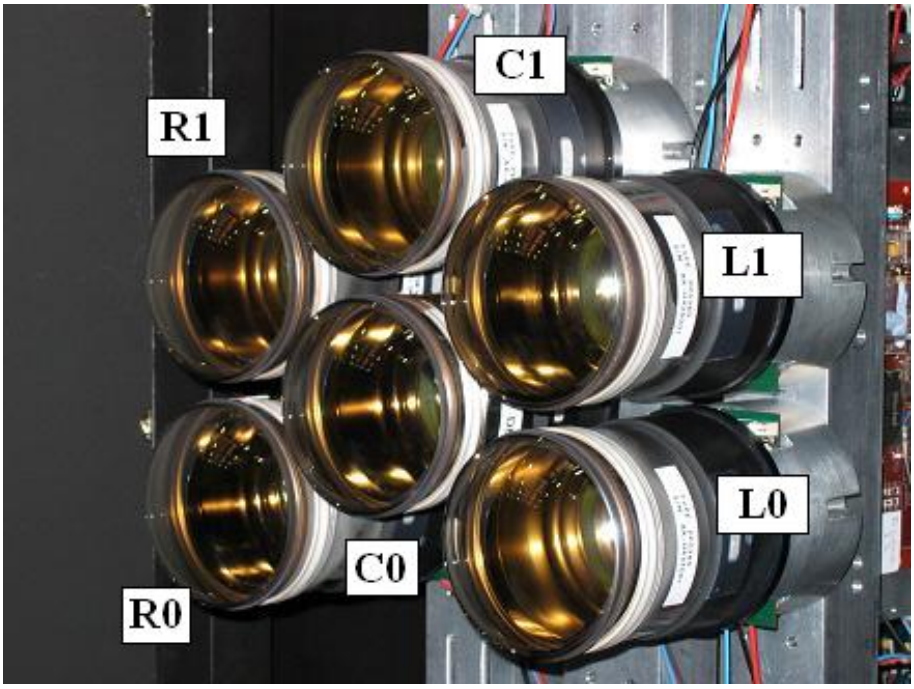

Figure 6.6: Close-packed HPDs mounted in the SSB, showing the arrangement of the HPDs and the columns.

- An LED was used in continuous (not pulsed) mode to illuminate the HPDs.
  - A standard LED data series is used later to gain an insight into the timing characteristics of the individual hits on an HPD.
  - A high voltage scan was undertaken with the LED to evaluate the effect of the threshold with improved sensitivity.

The six HPDs are designated L1, L0, C1, C0, R1 & R0 depending on whether they are situated on the left, central or right column as seen from behind, as shown in Figure 6.6.

6.2 Photon Yield Analysis

The main goal of this analysis is to compare the average number of photoelectron hits observed by the HPDs on a Cherenkov ring, with the expected number. This analysis is focussed primarily on the rings produced by the N_2 radiator where corrections due

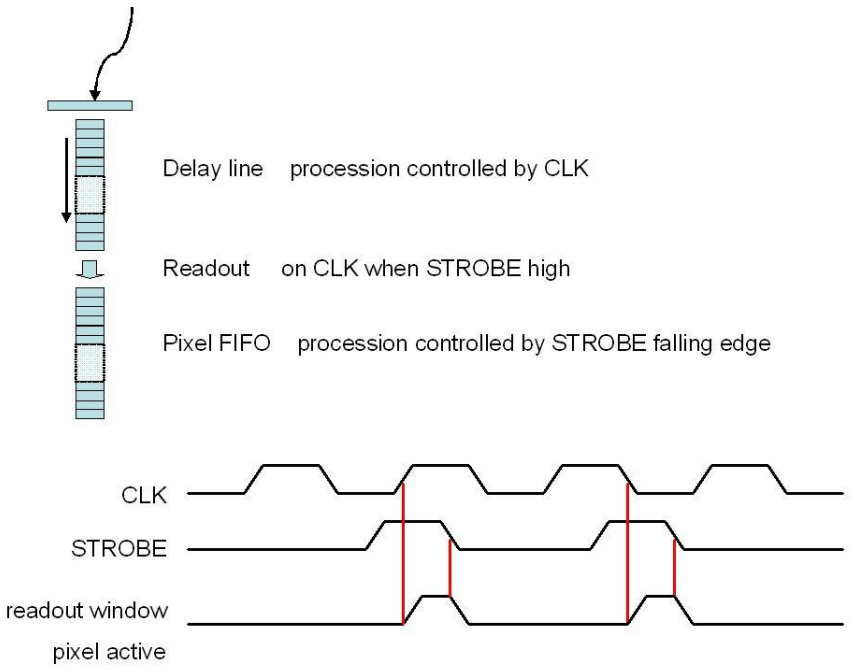

Figure 6.7: *top*: The sequence of operation of the delay line within the pixel chip in the testbeam. *bottom*: The timing diagram showing the method by which the efficiency curve is produced by varying the delay between the STROBE and leading edge of the CLK signal.

to the geometrical coverage are not relevant. Corrections that are required owing to the timing issues are extracted using the wider range of operating conditions available for the C_4F_{10} data.

As this series of measurements demonstrates, the relative timing of the arrival of a photoelectron on the anode and the HPD trigger influences the detection efficiency. In these tests the readout chip is set to operate with a delay (the latency) allowing time for the trigger signal processing. To activate the HPD readout a STROBE trigger signal is sent to the pixel chip. The chip reads out the pipeline on the clock signal when the STROBE is present, and moves to the next set of data when the STROBE falls. This is shown in Figure 6.7. However, as a STROBE signal is generated by the trigger unit (although it is synchronised to the global clock) the differing performance of each HPD's electronics means the optimum synchronisation between the STROBE and the CLK signal can not be achieved for all the HPDs simultaneously. This leaves some of the HPDs operating at less than their maximum efficiency, and this had to be quantified to correct the expected photon yield calculation.

To determine this efficiency several measurements were taken incrementally increasing the delay. This shows the HPD occupancy rising to a maximum and then falling away as the optimum point is passed for each HPD, as seen in Figure 6.8. This distinctive triangular shape is caused by varying the relative delay of the two 25ns windows of the CLK and the STROBE, as shown in Figure 6.7. From these data it is possible to calculate the relative efficiencies of each tube at any delay setting.

The consistency of the data between individual pixels is demonstrated by repeating the efficiency scan for each pixel and examining the spread. This produces the results shown in Figure 6.9. The banded region is the spread of the normalised pixel occupancy of illuminated pixels, demonstrating that there is a very small timing uncertainty between pixels. This means that the timing efficiency correction, calculated from the C_4F_{10} data can be applied to all the pixels in an HPD.

The response of the HPD and its dependence on the timing are highlighted in this test beam due to the asynchronous timing inherent to the beam's operation. At the LHC the events are expected to be synchronised to the LHC bunch crossings and will occur at a similar time within each readout window. In this series of tests the events occur randomly within the readout window, leading to a reduced efficiency if not enough time is left to collect all the charge deposited on the HPD pixel chip. This effect can be seen in Figure 6.10. To compensate for this effect, the effect of charge sharing and that of two photons arriving in the same pixel within 25ns, a fit to the recorded data was performed to achieve an accurate correction. This is described below in Section 6.2.3.

6.2.1 Expected Photon Yield

The N_2 photon yield measurements were taken using the delay settings shown in Table 6.1. The N_2 data were used to avoid the complications of having a Cherenkov ring fall over multiple HPDs and to factor in the efficiencies for all the HPDs involved.

The expected photon yield is calculated by determining the number of Cherenkov photons that were seen in each of the N_2 ring configurations, and then taking account of the reflectivity of the mirror, the transmissivity of the quartz window, the Quantum Efficiency(QE) of the photocathode, the detection efficiency of the pixel

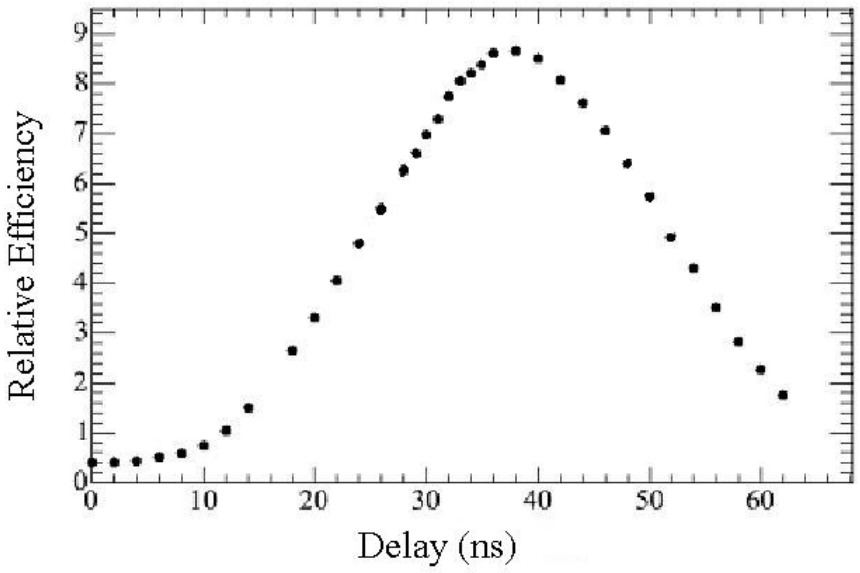

Figure 6.8: Plot of the efficiency, averaged over all pixels for a single HPD, as a function of the relative delay between the STROBE and the leading edge of the CLK signal. The data are from the C1 HPD and clearly show the distinctive triangular shape.

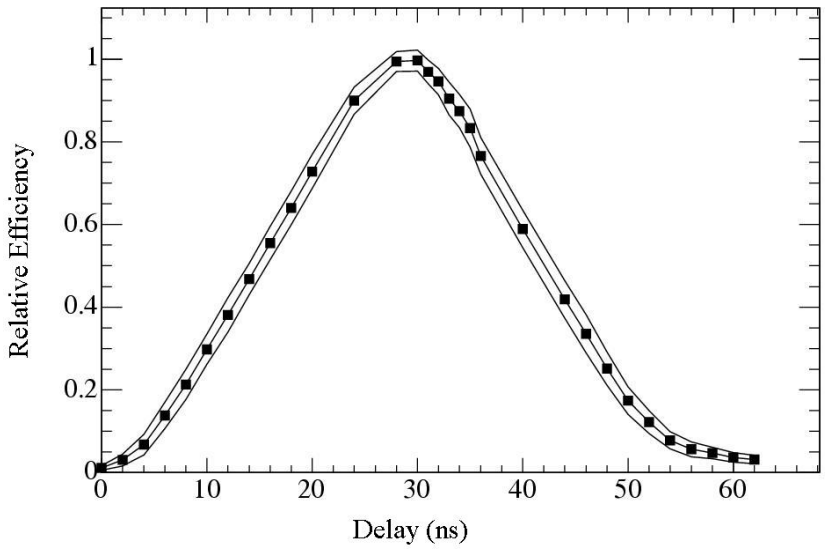

Figure 6.9: The delay curve, averaged over the 40 most illuminated pixels, in the C1 HPD. The banded region is one standard deviation.

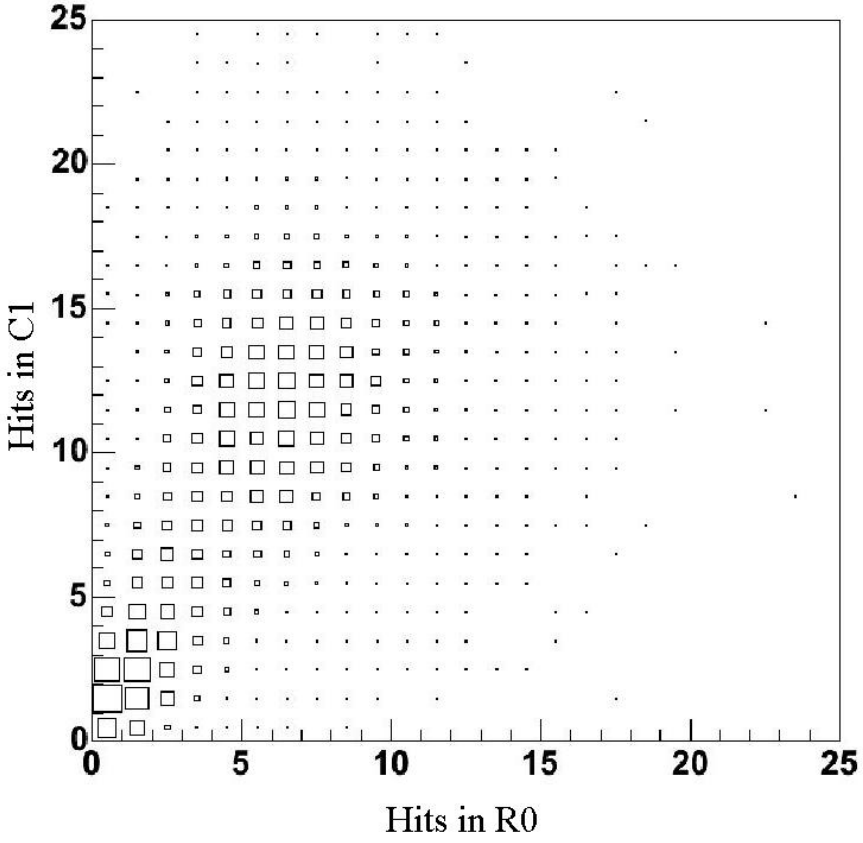

Figure 6.10: The correlation between two HPDs showing the number of photons per event across two HPDs illuminated in the same C_4F_{10} event. This shows a lower multiplicity in one tube is correlated to a lower multiplicity in the other. This indicates there is a universal effect that can be attributed to relative timing between the beam particle and the HPD readout window.

HPD	L0	L1	C1	R0	R1
Track Length (mm)	1099	1101.5	1102	1100	1098
Strobe Delay	38ns	38ns	32ns	30ns	30ns
Timing Eff.	100%	100%	98%	96%	92%
p.e. Detection Eff.	85%	85%	85%	85%	85%
μ_{exp}	11.1	10.1	11.1	8.7	9.9
Uncertainty	$\pm$ 0.8	$\pm$ 0.7	$\pm$ 0.8	$\pm$ 0.7	$\pm$ 0.9

Table 6.1: A summary of the values of the wavelength independent parameters that were used to calculate the expected photon yield. Also tabulated are the expected yield μ_{exp} and its rms uncertainty.

chip and the misaligned timing efficiency discussed in Section 6.2. The particle track length, timing efficiency and detection efficiency are independent of the wavelength of the photons and are summarised in Table 6.1. The other effects, including photon production, QE, reflectivity and transmissivity are wavelength dependent and the measured values and calculations are shown below with more detailed results tabulated in Appendix C.

To account for the wavelength dependance of several of the factors a numerical calculation was performed over appropriate wavelength bands and the measured correction applied to each interval. The photons produced after these steps are summed and the universal corrections are then applied. This is complicated by the measured values (reflectivity, transmissivity and the QE) being taken at different wavelengths and with differing intervals, resulting in the wavelength steps being necessarily larger than ideal. To calculate the number of Cherenkov photons produced in each wavelength band the formula

$$N = 2\pi\alpha l \left(\frac{1}{\lambda_2} - \frac{1}{\lambda_1}\right)\left(1 - \frac{1}{\beta^2 n^2}\right) \tag{6.1}$$

is used. Where α is the fine structure constant, l is the length of the particle path through the radiator, n is the refractive index of the radiator, β is the velocity expressed as a fraction of the speed of light and λ_1 and λ_2 are the limits of the wavelength band. This formula results from the integration of equation 3.2 between λ_1 and λ_2.

6.2.2 Correcting for HPD effects

In addition to the timing correction, photocathode quantum efficiency and the photoelectron detection efficiency there are three effects inherent to HPDs operating in these conditions. These are charge sharing, two photons falling on the same pixel in the same bunch crossing (double hits) and the effect of the beam's asynchronous timing.

To extract the average number of photons detected in a pion Cherenkov ring, the measured distribution in the number of hits was fit to a model in which the mean and overall normalisation were free parameters. The distribution is not a simple

Poisson owing to the corrections that need to be applied, resulting in a summation of Poisson distributions of different means.

The effect of charge sharing in the silicon increases the number of hits recorded. This is modelled as a Poisson distribution with its mean dependant on the number of hits in a given event. The scaling factor for this effect for each HPD is calculated using a 'fake hit' analysis method. This involves combining a single hit, selected at random from one event with hits selected at random from similar events. The total number of merged hits follows a Poisson distribution and the resultant "fake" ring events cannot contain physical charge sharing. Any adjacent hit pixels result from random association and the events are compared with real events. The difference in the number of adjacent hits is used to determine the level of charge sharing. The results of the fake hit analysis are shown in Table 6.2.

The effect of two photons falling into the same pixel within a clock cycle is also characterised using the fake hit analysis. It is a smaller effect than charge sharing and is related to the square of the mean number of photons.

To compensate for the effect of particles arriving asynchronously to the HPD clock, the distribution of particles produced by this effect had to be modelled to allow a fit to be performed. In an ideal situation a hit can be considered to be a delta function in the time domain, the incorporation of a jitter in the system smears this to a Gaussian shape, and the addition of timewalk adds a tail to the distribution (parameterised as an exponential). These two effects are characterised by the width (σ) of the Gaussian distribution and the time constant (τ) of the decaying tail.

An example of the data and the fitted curve is shown in Figure 6.11. The model gives a good fit to the data.

6.2.3 Measured Photoelectron Yield

This fitting process was applied to a data set for complete pion runs. Electron and Kaon events were filtered out using the ring diameter. Only hits that fell within the expected ring region are counted to remove other sources of noise.

The results of the fit to determine the photon yield and a comparison with the

HPD	L1	L0	C1	R1	R0
Charge Sharing	0.027	0.035	0.037	0.001	0.039
Uncertainty	± 0.007	± 0.005	± 0.018	± 0.004	± 0.01
Double Hits	0.039	0.031	0.048	0.041	0.045
Uncertainty	± 0.002	± 0.001	± 0.001	± 0.002	± 0.002
Jitter (σ)	3.9	3.3	0.1	0.04	0.06
Uncertainty	± 0.1	± 0.1	± 0.2	± 0.05	± 0.31
Time Constant	4.3	5.9	5.6	5.8	6.42
Uncertainty	± 0.1	± 0.1	± 0.2	± 0.1	± 0.04
Active Fraction	0.95	1.00	0.85	0.96	1.00

Table 6.2: Summary of the fraction of events with adjacent hits in normal and fake events. The probability for charge sharing is given by the difference in these fractions. The low levels of charge sharing observed in HPD R1 are explained by the high threshold used for this tube. These results were produced by Tom Blake and Richard Hallam (Imperial College)[92][93].

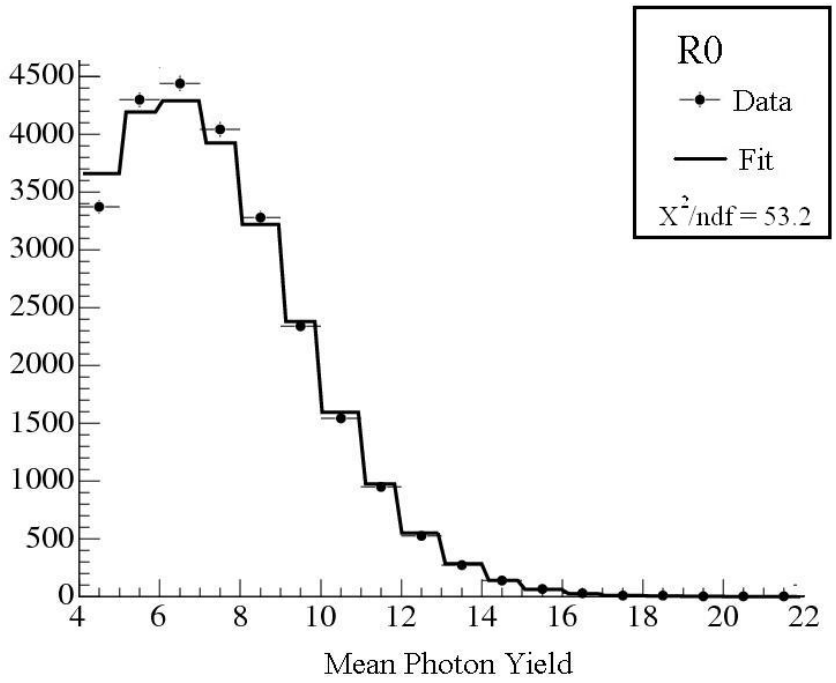

Figure 6.11: A fit to the measured photon yield in a N_2 radiator incorporating the corrections for the R0 HPD.

HPD	L0	L1	C1	R0	R1
μ_{fit}	8.2	10.2	11.7	8.7	9.9
Uncertainty	± 0.1	± 0.1	± 0.3	± 0.2	± 0.1
μ_{exp}	11.1	10.1	11.1	8.7	9.9
Uncertainty	± 0.8	± 0.7	± 0.8	± 0.7	± 0.9
Ratio	0.74	1.01	1.05	1.0	1.0
Uncertainty	±0.07	±0.07	±0.07	±0.1	±0.1

Table 6.3: Comparison of the measured and expected photon yields for the individual HPDs. The last row is the ratio μ_{fit} : μ_{exp}, where μ_{fit} is the mean extracted from the fit to the data and μ_{exp} gives the expected number of photons , including timing and quantum efficiency corrections.

expected photon yield are shown in Table 6.3. The predictions and measurements for L1, C1, R1 and R0 match within the expected uncertainties. C0 was found to have a faulty Level-0 channel and so has been excluded and the abnormal L0 yield is unexplained at present.

6.2.4 Uncertainty in the Determination of the Photoelectron Yield

The sources of uncertainty in the photoelectron yield contribute to uncertainties in both μ_{fit} and μ_{exp}. This is due to the inclusion of the pixel chip corrections into the fit. The contributions for both μ_{fit} and μ_{exp} are given in Table 6.4.

The four sources of uncertainty contained within the fitting process are evaluated. These are the uncertainties in the values of the frequency of charge sharing and double hits, the level of timing jitter, and the value of the time constant in the timing model. To evaluate these uncertainties the fits were repeated for each of the sources, varying the input values over a range corresponding to the given uncertainty. The results of these calculations are shown in Table 6.4 and demonstrate that the systematic error within the fitting process is dominated by the uncertainty in the level of charge sharing.

The values for the uncertainty on the double hit and charge sharing parameters are taken from the fake hit analysis results shown in Table 6.2. The values for the timing parameters are obtained by fitting the timing functions described in Section 6.2.2

to LED data, where the whole tube is illuminated.

The external sources of uncertainty are dominated by that of the quantum efficiency of the photocathode for each HPD, but also include contributions from the timing efficiency and the photoelectron detection efficiency. The uncertainties of the reflectivity of the mirror and the transparency of the quartz windows were small enough to be ignored in this analysis.

The following contributions to the error on μ_{exp} are shown in Table 6.4.

- The detection efficiency uncertainty is determined from previous work by the HPD group[94]. This was achieved by comparing the number of hit pixels to a fit performed on the analogue pulse height distribution obtained by collecting the charge from the back-surface of the pixel sensor.
- The timing efficiency uncertainty is calculated by taking the nanosecond level jitter seen in the timing boards and applying it to the timing curve. The tubes operating near the peak efficiency are less affected as their region of efficiency is reasonably flat. Those further from the peak are affected more strongly due to the steep rate of change of the efficiency.
- The quantum efficiency uncertainty is estimated from a comparison of measurements performed at DEP following the HPD manufacture and independent measurements performed at the test stations in Edinburgh.
- It is assumed that the uncertainty on the measurement of the transmission curve of the quartz and the reflectivity of the mirror are small compared to the others as very high accuracy can be achieved with the precision equipment available in the CERN lab where they were characterized.

The results show that the uncertainty from the fitting process is relatively small compared to that contributed by the HPD characteristics (particularly the uncertainty in the photocathode quantum efficiency).

HPD	L0	L1	C1	R0	R1	max
μ_{fit}						
Double Hit	0.002	0.019	0.012	0.017	0.021	0.024
Charge Sharing	0.06	0.09	0.26	0.21	0.05	0.28
σ	0.01	0.03	0.02	0.01	0.00	0.03
τ	0.02	0.02	0.04	0.01	0.00	0.04
$\sigma\mu_{\text{fit}}$	0.06	0.10	0.26	0.21	0.06	0.28
μ_{exp}						
QE	0.57	0.50	0.56	0.45	0.54	0.57
Timing Eff.	0.34	0.30	0.45	0.53	0.64	0.64
p.e. Det. Eff.	0.34	0.30	0.34	0.27	0.32	0.34
$\sigma\mu_{\text{exp}}$	0.75	0.66	0.79	0.74	0.90	0.95

Table 6.4: The contribution to the percentage uncertainty of the mean number of photons for each effect and added in quadrature, and the maximum uncertainty for each effect over all the tubes. σ and τ represent the uncertainties on the parameters for the asynchronous timing model and QE denotes the photocathode quantum efficiency.

6.3 Conclusions

Of the HPDs used in the second test beam run, Table 6.3 shows that four of the six performed with the expected photon detection efficiency. The tube designated C0 was subsequently found to have a faulty Level-0 channel, resulting in a timing problem and its results were discarded. The L0 HPD's yield is significantly lower than was expected and cannot be explained at the present time. The uncertainty of this analysis is dominated by the uncertainties of the quantum efficiency measurement and the timing efficiency correction.

Performing this analysis has improved our understanding of a range of HPD issues, especially the importance of timing effects and high voltage systems across an array of HPDs. The detection of infrared light (820nm) escaping from the optical links in the electronics read out chain was unexpected and measures have been taken to eliminate this background source.

Chapter 7

Summary and Conclusions

This thesis has reported on development work undertaken as part of the collaborative effort to construct the LHCb detector, to be able to start making measurements in 2007 when colliding beams will be available from the LHC. It is expected that the big step in B production yield will add to our knowledge of the physics of the quark flavour, complementing the work of the previous generation of experiments. To this end we expect that as well as observing and measuring to higher precision expected CP violating effects, indications of physics beyond the Standard Model will be seen. These include non-Standard Model CP violating effects resulting from flavour changing neutral currents.

LHCb is uniquely adapted to make these measurements. The LHC collision energy of 14TeV surpasses all previous colliders, and allows the production of B_s mesons creating opportunities for measurements of the parameters of the CKM unitarity triangle that have been out of reach of the detectors operating at e^+e^- colliders at the Υ(4s) resonance. The VELO system will make measurements of the proper decay time evolution and mixing parameters of the B mesons, allowing their mass splitting in oscillation to be measured with high precision. The RICH system will provide particle separation across a wide range of momenta, and will perform a crucial role in identifying the underlying quark content of the majority of events that are of potential physics interest.

The two RICH detectors, which at the time of writing are nearing completion in IP8, are each instrumented with two arrays of photo tubes. These Hybrid Photon

Detectors (HPDs) have been designed and developed by a team working at CERN over the development period of LHCb. Their development has presented one of the hardest technical challenges in the LHCb project. They consist of a large area photocathode, covering a high fraction of the geometrical footprint of the tube, that converts visible and UV incident photons into photoelectrons that are focussed by an electrostatic field onto a pixilated silicon sensor anode. The sensor is bump-bonded directly to the back of a read-out chip. This chip, the LHCbPIX1, provides amplification and shaping, discrimination, a decision pipeline and a read out route to the Level-0 electronics for all 256 by 32 channels on the silicon sensor.

The photoelectron trajectories in the electrostatic field of the HPD are distorted by the magnetic field used to deflect particles in the tracking system. This leads to a loss of detected photoelectrons if the field exceeds 10G. The development and testing of an adequate system of magnetic shielding for the RICH1 sub-detector is described in Chapter 4. This involved the iterative simulation of the performance of the magnetic dipole and the proposed shield system in a finite element analysis package. The shield design had to provide protection for the HPDs, whilst increasing the field at the beamline to improve the performance of the Level-1 trigger. By simulating the components of the proposed shield design in turn, it was possible to determine their effect on the overall system and achieve a comprise that also complied with the mechanical constraints implied by the location of neighbouring sub-detectors.

Once the RICH1 magnetic shield was completed and installed in the LHCb cavern a series of measurements was carried out to verify its performance. These are reported in Chapter 4. These measurements indicate that with individual cylindrical mumetal shields the HPDs will operate in the field present in their proposed location. The field in the acceptance of the spectrometer is also about 20% less than that predicted by the model, however the loss in efficiency to the charged particle trigger is small and probably recoverable using improved algorithms that use data from the tracking stations downstream of the LHCb magnet.

Chapter 5 reports on two novel investigations into the performance of the critical LHCbPIX1 chip. A pulsed laser was used to deposit charge at a precise location on the sensor and chip not mounted in an HPD. A magnetic field was used to distort the electron optics of a fully operational HPD to allow photoelectrons to fall on otherwise unavailable test pixels for which analogue circuitry was accessible. These

two methods allowed investigation of three effects:

- The chip's charge sharing characteristics, the process by which a single photoelectron falling between pixels can result in a signal that exceeds threshold in both. Increasing the threshold level removed this problem but produced a dead area around each pixel that would be undesirable.
- The effect of timewalk, a process by which a low amplitude signal in the read out system passes threshold later. This can cause random noise in later clock cycles, but seems to be of a negligible level at the nominal HPD voltage settings.
- The length of the dead time after a hit, measured in an operational HPD for the first time, and seen to leave a sub-pixel blind for the clock cycle after a hit has been registered. The low occupancy of the RICH photon detector planes means this is not a serious problem, however it should be taken into account when evaluating the effect of other noise sources and in the planning for the proposed higher luminosity super-LHCb upgrade.

Finally Chapter 6 reports on a series of tests carried out on the HPD and its readout electronics in a charged particle beam, in the T9 area of the PS facility at CERN. This test was the first demonstration of the operation of a prototype read out chain and the operation of an array of HPDs. A small scale RICH system was constructed for the test so that the HPDs could be used to detect Cherenkov light. These tests confirmed that the HPDs are detecting the number of photon hits consistent with the model of operation used for the RICH system. In addition they provided a valuable insight into the importance of the timing of the electronics system, the response of the read out electronics and the HPDs' sensitivity to infrared light produced by the fibre optic devices on the Level-0 boards.

This thesis has reported primarily on work developing LHCb systems relating to the HPDs and the RICH1 magnetic shielding required for their operation. With the RICH1 magnetic shielding in its final location work is underway to install the other RICH1 subsystems, initially the gas enclosure, followed by the beampipe and the exit window. The design for the electronics column, complete for RICH2, is being altered and optimised for the conditions in RICH1, involving rerouting the services and developing a reliable extraction mechanism. Following the successful

operation of the HPDs and their electronics in the 2004 testbeam, further studies have been carried out with full RICH2 columns of 18 HPDs and their associated electronics. In parallel the final production and testing effort has begun to produce, assemble and test all the HPD columns in time to take data at the first LHC beam in 2007. Once the LHCb installation and commissioning is complete and data taking has begun it is the intention of the Imperial College group to continue to focus on the analysis of rare decays, and in particular to measure the rate and angula distributions of the decay $B \rightarrow K^{*}\mu^{+}\mu^{-}$. In the longer term there are prospects to upgrade LHCb to operate at a higher luminosity of $2 \times 10^{33}\mathrm{cm}^{-2}\mathrm{s}^{-1}$ independent of any possible Super-LHC upgrade. This will require replacing the VELO tracking planes with higher granularity, more radiation hard designs, and possibly upgrading the granularity of the HPD photon detectors in the RICH systems. An upgrade of this type would increase the data sample available to LHCb by at least an order of magnitude, bringing even rarer channels into reach.

Appendix A

Particle Identification Performance

This appendix describes the calculations that led to Figure 3.5. The precision in measurement of the Cherenkov angle is obtained from simulations performed for the LHCb RICH Technical Design Report[35] and the Reoptimised Detector Technical Design Report[45].

The angle of Cherenkov light produced in each radiator was calculated for hadrons of mass m, with a range of particle momenta, p, from 1GeV/c to 150GeV/c, using the following formula and input parameters given in Table A.1.

$$\cos\theta = \frac{1}{n\beta} \tag{A.1}$$

$$\beta = \frac{1}{\sqrt{1 + m^2/p^2}} \tag{A.2}$$

Angles were calculated for all three radiators. Those for C_4F_{10} are shown in Figure A.1.

The difference between the Cherenkov angles for pions and kaons was calculated and divided by the corresponding precision in the measurement of the angle σ_θ. The parameter σ_θ includes terms due to the emission point error, the pixel granularity and the chromatic dispersion of the radiator summed in quadrature. This is scaled by

Radiator		Aerogel	C_4F_{10}	CF_4
Refractive Index		1.03	1.0014	1.0005
$m(\pi)$	(GeV)	0.138	0.138	0.138
$m(K)$	(GeV)	0.497	0.497	0.497
m(proton)	(GeV)	0.939	0.939	0.939
θ_c	(mrad)	242	53	32
$\sigma_{emission}$	(mrad)	0.60	0.74	0.31
σ_{pixel}	(mrad)	0.78	0.83	0.18
$\sigma_{chromatic}$	(mrad)	1.61	0.81	0.42
σ_{track}	(mrad)	0.26	0.42	0.20
σ_θ	(mrad)	2.00	1.45	0.58
$N_{photoelectrons}$		6.6	32.7	18.4

Table A.1: The parameters for the three radiators and the values of the 4 major sources of uncertainty for each.[35]

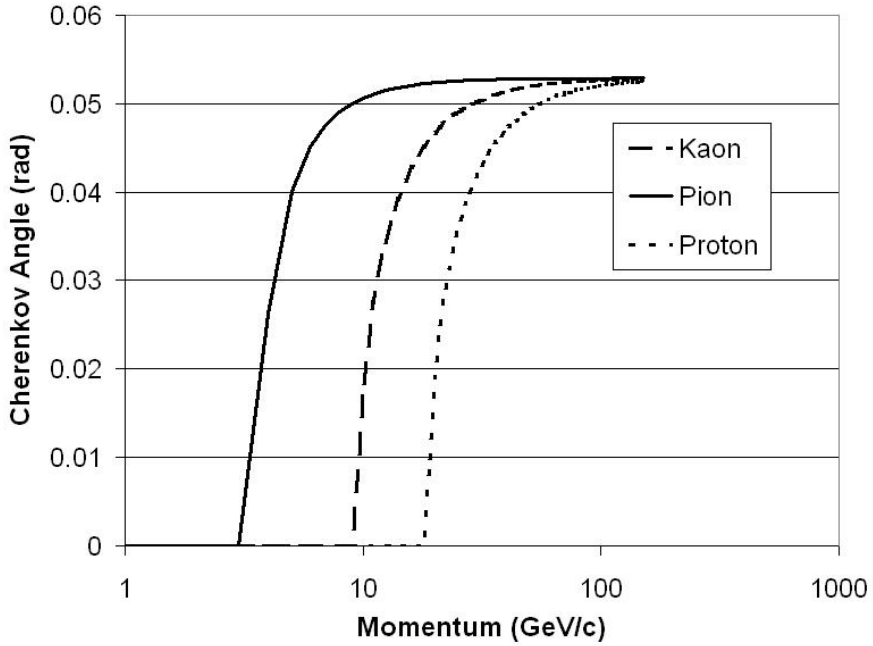

Figure A.1: Cherenkov angles of pion, kaon and proton in C_4F_{10}.

$n^{-1/2}$, where n is the average number of photoelectrons detected and then combined with the uncertainty in the measurement of the particle's trajectory.

Specifically

$$\sigma_\theta = \sqrt{\frac{\sqrt{\sigma_e^2 + \sigma_p^2 + \sigma_c^2}^2}{n^{1/2}} + \sigma_t^2} \tag{A.3}$$

Appendix B

Magnetic Models

In total over 150 models were calculated for the magnetic shield design presented in Chapter 4. Over 60 days of CPU time were used. In the interest of clarity, specific results were not included in Chapter 4, and some are tabulated in this appendix.

B.1 Upstream Plate

This section gives the full results for three studies designed to optimise the height and thickness of the upstream plate. The first two were studies of the vertical distance between the beampipe and the lower (or upper) edge of the front plate, one with a magnetic block present and one without. The third describes the plate thickness study. These results are shown in Tables B.1, B.2 & B.3.

B.2 Magnetic Block

This section contains the full results for the magnetic block study. The 'top' and 'bottom' are the upper and lower y-coordinates of the magnetic block and the value of 'depth' given is the z extent of the block away from the back plate. The results are presented in Tables B.4 & B.5 following, split only for convenience.

y-coordinate (cm)	$\mathbf{B}_{trig}$ (Gcm)	$\mathbf{B}_{max}$ (G)
30	115277	6.4
35	112438	6.9
37	111432	7.1
39	110488	7.4
41	109601	7.6
43	108766	7.8
45	107979	8.1
47	107236	8.44
49	106533	8.7
51	105868	9.1
53	105239	9.4
55	104643	9.7
57	103594	11.4
59	103080	11.8
65	101720	13.3

Table B.1: An early shield design without a magnetic block. The y-coordinate giving the distance of the bottom of the upstream plate from the beamline.

y-coordinate (cm)	$\mathbf{B}_{trig}$ (Gcm)	$\mathbf{B}_{max}$ (G)
25	165597	20.3
30	159844	20.9
35	155449	22.1
40	151742	23.4
45	148526	24.9
50	145738	26.6
55	143300	28.6

Table B.2: A later shield design with a magnetic block to check consistency. As before the y-coordinate defines the distance of the bottom of the upstream plate from the beamline.

Thickness (cm)	$\mathbf{B}_{trig}$ (Gcm)	$\mathbf{B}_{max}$ (G)
5	143300	28.6
7	143784	26.9
9	144273	25.4
11	144752	23.9
13	145217	22.4
15	145673	20.9

Table B.3: A later design with a magnetic block, the thickness is the z direction and defines the thickness of the upstream plate.

depth (cm)	top (cm)	bottom (cm)	$\mathbf{B}_{trig}$ (Gcm)	$\mathbf{B}_{max}$ (G)
0	0	0	106000	8.75
30	90	70	105532	13.5
30	110	90	108745	13.3
30	130	110	110651	16.2
30	150	130	110704	11.5
30	170	150	109774	11.4
50	70	50	110049	13.5
50	90	70	111105	16.9
50	110	90	115640	17.2
50	130	110	118471	25.4
50	150	130	117970	14.3
50	170	150	115175	13.3
50	190	170	109603	11.5
30	110	70	107885	14
30	130	90	110935	18.2
30	150	110	112475	36.37
30	170	130	111445	11.9
70	90	70	123411	22
70	110	90	128290	23.5
70	130	110	130996	41
70	150	130	128907	18.4
70	170	150	122907	15.9
30	130	70	110083	18.6
30	150	90	112724	45.4
30	170	110	113078	37.8

Table B.4: Magnetic block investigation.

depth (cm)	top (cm)	bottom (cm)	$\mathbf{B}_{trig}$ (Gcm)	$\mathbf{B}_{max}$ (G)
50	90	50	115425	15.9
50	110	70	116031	18.1
50	130	90	119725	28.69
50	150	110	121182	41
50	170	130	118630	14.5
50	190	150	113279	12.9
70	110	70	131604	25.1
70	130	90	134586	49.9
70	150	110	134594	46.8
70	170	130	129182	18.3
50	110	50	120726	15.9
50	130	70	120004	30.7
50	150	90	122180	47
50	170	110	121536	43.7
50	190	130	116422	14.1
50	130	50	125033	27
50	150	70	122368	48.4
50	170	90	122370	49.66
50	190	110	120796	43
70	130	70	137454	52.5
70	150	90	137597	52.6
50	150	50	127647	45.3
50	170	70	122452	50.2
50	190	90	119757	49.3
50	170	50	127747	47.1
50	190	70	119694	49.6
50	190	50	124821	46.7

Table B.5: Magnetic Block Investigation continued.

Thickness (cm)	Plate from Beamline (cm)	$\mathbf{B}_{trig}$ (Gcm)	$\mathbf{B}_{max}$ (G)
10	55	148568	27.5
10	40	144866	25.2
10	25	137801	22
5	80	151735	31.8
5	55	149940	28.3
5	25	139899	23.1

Table B.6: Side plate study results.

B.3 Side Plates

Table B.6 shows the results of a study into the effect of the y extent, measured from the lower edge of the plate to the beamline at $y = 0$, and thickness of the side plates.

Appendix C

Calculation of the Expected Photon Yield

This appendix describes the calculation that was made to estimate the average number of photons expected to be detected in the SSB testbeam RICH detector with an N_2 radiator. This calculation needs to include the wavelength dependence of the mirror reflectivity, the transmission efficiency of the quartz window and the quantum efficiency of the HPD photocathodes. In addition to these three factors the photoelectron detection efficiencies for each HPD are taken into consideration.

The results of this calculation are given in Table 6.1

C.1 Cherenkov Photon Production

The equation:

$$N = 2\pi\alpha l \left(\frac{1}{\lambda_2} - \frac{1}{\lambda_1}\right)\left(1 - \frac{1}{\beta^2 n^2}\right) \tag{C.1}$$

was used to calculate the number of photons produced in each wavelength band from λ_1 to λ_2. N is the number of photons, α the fine structure constant, l the length of the radiator, β the velocity and $n(\lambda)$ the refractive index of the radiator.

Wavelength (nm)	L0 (photons)	L1 (photons)	C1 (photons)	R0 (photons)	R1 (photons)
200	5.38	5.39	5.39	5.38	5.37
240	17.02	17.06	17.07	17.04	17.01
270	9.46	9.48	9.48	9.47	9.45
300	7.57	7.58	7.59	7.57	7.56
320	4.26	4.27	4.27	4.26	4.25
360	7.09	7.11	7.11	7.10	7.09
400	5.67	5.69	5.69	5.68	5.67
440	4.64	4.65	4.66	4.65	4.64
480	3.87	3.88	3.88	3.87	3.87
520	3.27	3.28	3.28	3.28	3.27
560	2.81	2.81	2.81	2.81	2.80
600	2.43	2.44	2.44	2.43	2.43
640	2.13	2.13	2.13	2.11	2.13
700	2.74	2.74	2.74	2.74	2.73
750	1.95	1.95	1.95	1.95	1.94
800	1.70	1.71	1.71	1.70	1.70

Table C.1: The average number of photons produced for each HPD taking into account the different path lengths produced by the different mirror positions.

The wavelength bands used were irregular and were set by the available data for the transmission, reflection and quantum efficiency, as no accuracy is gained by interpolation. The number of photons produced in each band for each HPD mirror position is shown in Table C.1.

C.2 Reflection and Transmission

To determine the wavelength dependent properties of the mirror and quartz window, their reflectivity and transmission efficiencies were measured, with the results shown in Table C.2. These efficiencies were applied to the wavelength bands generated in Table C.1. As the wavelength bands from the measurements did not overlap, the calculation was made by selecting points where data was available and using them as the boundaries for wider calculation bands. For reflection etc the value of the lower edge of the band was used to perform the calculation.

Wavelength (nm)	mirror reflectivity (%)	Quartz transmission (%)
190		84.23
200	14.49	84.60
210	58.32	87.39
220	84.63	89.92
230	92.28	90.48
240	94.95	89.24
250	96.23	90.54
260	96.75	91.69
270	97.12	92.49
280	97.25	92.63
290	97.28	92.67
300	97.20	92.55
310	97.04	92.49
320	96.55	93.19
340	96.55	93.62
360	95.99	93.91
380	95.07	93.65
400	93.99	93.65
420	92.68	93.37
440	91.06	93.69
460	89.40	93.76
480	87.52	93.76
500	85.59	93.70
520	83.58	94.18
540	81.86	94.09
560	80.35	94.26
580	79.11	94.32
600	78.14	94.35
620		94.35
640		94.44
660		94.42
680		94.42
700		94.67

Table C.2: The measured reflectivity and transmission for the mirror and quartz windows in the testbeam system.

Wavelength (nm)	L1 (%)	R0 (%)	R1 (%)	C0 (%)	L0 (%)	C1 (%)
200	9.07	4.12	9.39	6.94	7.46	11.61
240	22.28	18.21	23.78	16.12	25.03	25.21
270	25.41	22.30	26.17	18.35	27.17	27.90
300	21.84	18.36	22.61	15.17	23.40	24.28
320	19.50	15.75	20.35	12.91	21.20	22.14
360	19.34	15.78	20.15	12.89	20.93	21.92
400	20.19	19.79	20.89	19.83	21.03	21.99
440	20.25	23.82	20.80	18.97	21.55	21.98
480	16.20	18.61	17.87	15.99	18.53	17.03
520	13.13	13.72	14.73	12.84	15.27	14.63
560	10.47	10.12	12.04	10.64	12.64	12.01
600	7.95	6.99	9.21	8.32	9.68	8.45
640	6.37	5.33	7.86	7.20	8.30	7.62
700	3.80	2.44	5.40	5.42	5.80	5.24
750	1.89	0.81	3.64	4.17	4.01	3.44
800	0.57	0.14	2.15	3.04	2.43	1.85
830	0.24	0.05	1.33	2.33	1.54	1.05
850	0.12	0.02	0.80	1.89	0.98	0.60
880	0.02	0.01	0.10	0.62	0.13	0.08
900	0.00	0.00	0.02	0.16	0.02	0.01

Table C.3: Measured photocathode quantum efficiency

C.3 Quantum Efficiency

There is a small but significant variation in the quantum efficiency for each HPD. The curve QE(λ) for each HPD used in the testbeam was measured in the HPD lab at CERN, producing the results shown in Table C.3.

C.4 Wavelength Independent Efficiencies

The number of photons produced in each wavelength band was then summed to produce a number for each HPD and was then combined with the photoelectron detection efficiency within the detector and timing efficiency given in Table C.4.

HPD	L0	L1	C1	R0	R1
Timing Eff.	100%	100%	98%	96%	92%
Detection Eff.	85%	85%	85%	85%	85%

Table C.4: Detection and Timing Efficiency.

Bibliography

[1] M. Kobayashi and K. Maskawa, *"CP-Violation in the Renormalizable Theory of Weak Interaction"*, Prog. Theor. Phys. **49** 652 (1973).

[2] J. Christensen, J. Cronin, V. Fitch, R. Turlay, *"Evidence for the 2π Decay of the K_2^0 Meson"*, Phys. Rev. Lett **13**, 138 (1964).

[3] L. Lederman et al., *"Observation of a dimuon resonance at 9.5 GeV in 400-GeV proton-nucleus collisions"*, Phys. Rev. Lett. **39**, 252 (1977).

[4] S. Ting et al., *"Experimental Observation of a Heavy Particle J"*, Phys. Rev. Lett. **33**, 1404 (1974).

[5] B. Richter et al., *"Discovery of a Narrow Resonance in e^+e^- Annihilation"*, Phys. Rev. Lett. **33**, 1406 (1974).

[6] D. Andrews et al., *"Observation of Three Upsilon States"*, Phys. Rev. Lett. **44**, 1108 (1980).

[7] D. Andrews et al., *"Observation of a Fourth Upsilon State in e^+e^- Annihilations"*, Phys. Rev. Lett. **45**, 219 (1980).

[8] M. Gell-Mann and A. Pais, *"Behavior of Neutral Particles under Charge Conjugation"*, Phys. Rev. **97**, 1387 (1955).

[9] O. Schneider, *"Heavy flavour physics results from LEP1"*, IPHE 2000-009, May 2000.

[10] The D0 collaboration, *"The Upgraded D0 Detector"*, Fermilab-Pub-05/341-E.

[11] The CDF Collaboration, *"The CDF Detector: An Overview"*, FERMILAB-PUB-88-25-E, Feb 1988.

[12] The BABAR collaboration, *"Observation of CP Violation in the B^0 Meson System"*, Phys. Rev. Lett. **87**, 091801 (2001).

[13] The Belle Collaboration, *"The Belle Detector"*, NIM **A479**, 117 (2002).

[14] F. Halzen and A. Martin, *"Quarks and Leptons"*, Wiley, (1984).

[15] A. Sakharov, *"Violation of CP invariance, C asymmetry, and baryon asymmetry of the universe"*, JETP 5, 24-27 (1967). Republished in Soviet Physics Uspekhi 34 (1991) 392393.

[16] N. Cabbibo, *"Unitary Symmetry and Leptonic Decays"*, Phys. Rev. Lett. **10**, 531 (1963).

[17] S. L. Glashow, J. Iliopoulos and L. Maiani, *"Weak Interactions with Lepton-Hadron Symmetry"*, Phys. Rev. **D2**, 1583 (1970).

[18] F. Gilman, K. Kleinknecht, B. Renk, *"The CKM Quark Mixing Matrix"* Particle Data Group, (2005).

[19] L. Wolfenstein, *"Parametrization of the Kobayashi-Maskawa Matrix"*, Phys. Rev. Lett. **51**, 1945 (1983).

[20] P. F. Harrison and H. R. Quinn, *"The BABAR Physics Book"*, SLAC-R-504, (1998).

[21] NA48 Collaboration, *"A new measurement of direct CP violation in two pion decays of the neutral kaon"*, Phys. Lett. **B 465**, 335 (1999).

[22] KTeV Collaboration, *"Observation of Direct CP Violation in $K_{S,L}\rightarrow \pi\pi$ Decays"*, Phys. Rev. Lett. **83**, 22 (1999).

[23] The BABAR Collaboration, *"Measurement of CP-Violating Asymmetries in B^0 Decays to CP Eigenstates"*, Phys. Rev. Lett. **86**, 2515 (2001).

[24] The Belle Collaboration, *"Observation of Large CP Violation in the Neutral B Meson System"*, Phys. Rev. Lett. **87**, 091802 (2001).

[25] B. Aubert, et al, BABAR Collaboration, *"Improved Measurements of CP-Violating Asymmetries in $B^0 \rightarrow \pi^+\pi^-$ Decays"*, hep-ex/0407057 (2004).

[26] S. Banerjee, *"Prospects of B-Physics with CMS"*, CMS CR 2001-004, April 2001.

[27] The D0 Collaboration, *"Measurement of the Lifetime Difference in the B_s^0 System"*, D0 conference note 5052, May 2005.

[28] The CDF Collaboration, *"Observation of Bs-Bsbar Oscillations"*, hep-ex/0609040 (2006).

[29] R. Fleischer, *"New strategies to extract β and γ from $B_d \to \pi^+\pi^-$ and $B_s \to K^+ K^-$"*, Phys. Lett. **B 459**, 306 (1999).

[30] R. Aleksan, I. Dunietz and R. Kayser, *"Determining the CP-Violating phase γ"*, Z. Phys. **C 54**, 653 (1992).

[31] G. Raven, *"Selection of $B_s \to J/\psi\phi$ and $B^+ \to J/\psi K^+$"*, CERN-LHCb-2003-119, Dec 2003.

[32] T. Sjstrand, P. Eden, C. Friberg, L. Lonnblad, G. Miu, S. Mrenna and E. Norrbin, Computer Phys. Commun. 135, 238 (2001)

[33] The LHCb Collaboration, *"LHCb Technical Proposal"*, CERN LHCC 98-4, February 1998.

[34] The LHCb Collaboration, *"LHCb VELO Technical Design Report"*, CERN LHCC 2001-011, May 2001.

[35] The LHCb Collaboration, *"LHCb RICH Technical Design Report"*, CERN LHCC 2000-037, September 2000.

[36] The LHCb Collaboration, *"LHCb Inner Tracker Technical Design Report"*, CERN LHCC 2002-029, November 2002.

[37] The LHCb Collaboration, *"LHCb Outer Tracker Technical Design Report"*, CERN LHCC 2001-024, September 2001.

[38] The LHCb Collaboration, *"LHCb Calorimeters Technical Design Report"*, CERN LHCC 2000-036, September 2000.

[39] The LHCb Collaboration, *"LHCb Muon System Technical Design Report"*, CERN LHCC2001-010, May 2001.

[40] The LHCb Collaboration, *"LHCb Muon Technical Design Report Addendum 1"*, CERN LHCC 2003-002, January 2003.

[41] The LHCb Collaboration, *"LHCb Muon Technical Design Report Addendum 2"*, CERN LHCC 2005-012, April 2005.

[42] The LHCb Collaboration, *"LHCb Magnet Technical Design Report"*, CERN LHCC 200-007, January 2000.

[43] The LHCb Collaboration, *"LHCb Trigger System Technical Design Report"*, CERN LHCC 2003-031, September 2003.

[44] The LHCb Collaboration, *"LHCb Online System Technical Design Report"*, CERN LHCC 2001-040, December 2001.

[45] The LHCb Collaboration, *"LHCb Reoptimised Detector Design and Performance Technical Design Report"*, CERN LHCC 2003-030, September 2003.

[46] The LHCb Collaboration, *"LHCb 1MHz System Addemdum to Online Technical Design Report"* CERN LHCC 2005-039, November 2005.

[47] M. Needham, *"Updated Occupancies for the LHCb Inner Tracker"* CERN-LHCb-2005-006, February 2005.

[48] M. Needham, *"Silicon Tracker Simulation Performance"* CERN-LHCb-2003-015, February 2003.

[49] R. Fleischer, *"New Strategies to Obtain Insights into CP-Violation Through* $B_s \to D_s\ K$, $D_s^{*\pm} K^m p$, *... and* $B_d \to D^{\pm}\pi^m p$ *... Decays"*, Nucl. Phys. **B 671**, 459 (2003).

[50] M. Gronau and D. London, *"How to determine all the angles of the unitarity triangle from* $B_d^0 \to D\ K_s$ *and* $B_s^0 \to D_\phi$*"*, Greek Phys. Lett. B 253, 483 (1991).

[51] M. Calvi, O. Dormond and M. Musy, *"LHCb flavour tagging performance"* CERN-LHCb-2003-115, October 2003.

[52] T. Ypsilantis and J. Seguinot, *"A historical survey of ring imaging Cherenkov counters"*, NIM **A343**, 1 (1994).

[53] I. M. Frank and I. Y. Tamm, Doklady Akademii Nauk SSSR **A14**109-14 (1937).

[54] A. F. Danilyuk et al., *"Recent results on aerogel development for use in Cherenkov counters"* NIM **A494**, 491 (2002).

[55] T. Bellunato, M. Calvi, C. Coluzza, G. Longo, C. Matteuzzi, M Musy, P Negri and D Perego, *"Study of ageing effects in aerogel"* LHCb-2004-005, Mar 2004.

[56] R. Forty, O. Schneider, *"RICH pattern recognition"*, LHCb-98-040, April 1998.

[57] F. Muheim, *"Proposal for Multi-Anode Photo Multiplier Tubes as Photo Detectors for the LHCb RICH"*, LHCb 2000-065 RICH, September 2000

[58] M. Campbell, F. Formenti, T. Gys, W. Snoeys and K. Wyllie, *"Development of pixel hybrid photon detectors for the RICH counters of LHCb"*, LHCb-98-035, January 1998.

[59] G. Wilkinson, presentation, *Photodetector Performance Simulation Studies"*, $http://lhcb-rich.web.cern.ch/lhcb-rich/html/agenda_9 91103.html$, November 1999.

[60] N. van Bakel et al, *"The Beetle Reference Manual"*, LHCb 2001-046, April 2001.

[61] R. Chamonal, S. Eisenhardt, F. Muheim, *"Multianode photo multiplier tube signal response to magnetic fields up to 35 mT"*, LHCb-2003-042, June 2003.

[62] V. Gibson, et al., *"Performance of a cluster of Multi-anode Photomultipliers equipped with lenses for use in a prototype RICH detector"*, LHCb-2001-091, July 2001.

[63] K. Wyllie *"The LHCBPIX1 Preliminary Users Manual"*, October 2002. http://kwyllie.home.cern.ch/kwyllie/LHCBPIX1.htm

[64] A. van Lysebetten, presentation *"HPD/Mumetal insulation and B-field tests"*, http://indico.cern.ch/getFile.py/access?contribId =s1t4&resId=1&materialId=0&confId=a041981, May 2004.

[65] R. Hallam, Presentation, *"HPD Dark Tests"*, http://indico.cern.ch/getFile.py/access?contribId =7&resId=0&materialId=slides&confId=1121.

[66] S. Cuneo, M. Ameri, V. Gracco, P. Musico, A. Petrolini and M. Sannino, *"A proposal for a supporting structure for the Hybrid Pixel Detectors of RICH2"*, LHCb-2000-082, April 2001.

[67] K. Wyllie, *"Level-0 electronics for the LHCb rich"*, LHCb-2000-075, September 2000.

[68] S. Wotton, Presentation *"Level-1 Functions"*, http://indico.cern.ch/materialDisplay.py?contribId =s1t4&materialId=0&confId=a041001 2006.

[69] The LHCb Collaboration, *"LHCb RICH1 Engineering Design Report"*,LHCb-2004-121, October 2005.

[70] The LHCb Collaboration, *"LHCb RICH2 Engineering Design Report"*,LHCb-2002-009, March 2002.

[71] H. Dijkstra, J. Hernando-Morata, T. Schietinger and M. Witek, *"The relevance of the magnetic field in the Level-1 trigger"* LHCb-2003-110, August 2003.

[72] G. Aglieri-Rinella, Presentation, *"Magnetic Field Tests Lab Measurements"*, http://indico.cern.ch/materialDisplay.py?subContId=0&contribId =s8t5&sessionId=s8&materialId=0&confId=a036270, December 2003.

[73] Magnetic Distortion moitoring systems

[74] Vector Fields Ltd, *"OPERA-3D User Guide"*, VF-04-00D2, 1999-2000, Vector Fields Ltd., Oxford UK.

[75] Vector Fields Ltd, *"Frequently Asked Questions"*, VF-03-01-AB*, 1999, 2001, Vector Fields Ltd, Oxford UK.

[76] Newton Raphson Method

[77] S. Jolly, *"Development of Ring Imaging Cherenkov Detectors for the LHCb Experiment"*, CERN-THESIS-2005-016 , 2004 London, Imperial Coll.

[78] T. Gys, presentation *"Magnetic Shield Studies"*, http://tilde-gys.home.cern.ch/ gys/LHCb/Main.htm#MAG.

[79] T. Gys, *"Magnetic field simulations for the LHCb-RICH 2 detector"*, LHCb-2002-029, May 2002.

[80] M. Losasso, Presentation, *11LHCb Magnetic Field Issues for RICH1 Design""*, http://indico.cern.ch/materialDisplay.py?contribId =s1t5&sessionId=s1&materialId=0&confId=a01810, December 2001.

[81] R. Forty, Presentation *"RICH-1 Re-Optimization"*, http://indico.cern.ch/materialDisplay.py?contribId =s1t5&sessionId=s1&materialId=0&confId=a01810, December 2001.

[82] M. Patel, M. Losasso and T. Gys, *"Magnetic Shielding Studies of the RICH Photon Detectors"*, LHCb-2005-055, January 2006.

[83] P. Kohnke ed, *"ANSYS Theory reference"*, Ninth Edition, 1999, ANSYS Inc, Houston PA.

[84] M. Ferro-Luzzi, R.Lindner, H. Schuijlenburg, *"LHCb RICH1 Magnetic Shield Production Readiness Review Referee's Report"*,CERN EDMS 497636, September 2004.

[85] M. Losasso, Presentation, *"LHCb Field Mapping Campaign on May-June"*, http://indico.cern.ch/getFile.py/access?contribId =s1t0&resId=1&materialId=0&confId=a052665, May 2005.

[86] The ALICE Collaboration, *"Alice Technical Proposal of A Large Ion Collider Experiment at the CERN LHC"*, CERN/LHCC/95-71, December 1995.

[87] F. Muhiem et al., *"Photo Detector Test Facilities Production Readiness Review"*, LHCb-2005-nnn, July 2005.

[88] H. van der Bij et al., *"S-LINK, a Data Link Interface Specification for the LHC Era"*, IEEE Trans. Nucl. Sci. 44 (1997)

[89] JTAG Technologies Homepage, http://www.jtag.com/

[90] Wavemetrics Ltd., *"The LabVIEW User Mannual"*,320090E-01, 2003, National Instruments Corp, Austin, Tx. USA.

[91] L. Zhang, *"Test System for Optical Receiver Card"*, LHCB-2005-042, June 2005.

[92] T. Blake, Presentation, *"Adjacent Hits and Fake Rings"*, indico.cern.ch/getFile.py/access?contribId =s1t2&resId=1&materialId=0&confId=a052392, April 2005.

[93] R. Hallam, R. Plackett, presentation *"Delay Scans"*, indico.cern.ch/getFile.py/access?contribId =s1t2&resId=1&materialId=0&confId=a052392, April 2005.

[94] G.Aglieri-Rinella, Presentation, *"Performance Studies of Pixel HPDs for the LHCb RICH Counters"*, http://www.imperial.ac.uk/research/hep/preprints/01-3.pdf, May 2004.